The Astrophysical Journal, 904:25 (43pp), 2020 November 20 https://doi.org/10.3847/1538-4357/abbc6c

JWST Transit Spectra. II. Constraining Aerosol Species, Particle-size Distributions, Temperature, and Metallicity for Cloudy Exoplanets

Brianna I. Lacy and Adam Burrows
Princeton University, Peyton Hall, Ivy Lane, Princeton, NJ 08544, USA; blacy@princeton.astro.edu
Received 2020 June 17; revised 2020 September 15; accepted 2020 September 27; published 2020 November 19

Abstract

The James Webb Space Telescope (JWST) will provide moderate-resolution transit spectra with continuous wavelength coverage from the optical to the mid-infrared for the first time. In this paper, we illustrate how different aerosol species, size distributions, and spatial distributions encode information in the JWST transit spectra of warm exoplanets. We use the transit spectral modeling code METIS, along with Mie theory and several flexible treatments of aerosol size and spatial distributions to perform parameter sensitivity studies, calculate transit contribution functions, compute Jacobians, and retrieve parameters from simulated data. The broader wavelength coverage of the JWST can encompass enough non-gray aerosol behavior to recover information about the species and size distribution of particles under many feasible aerosol scenarios. Within the JWST wavelength range, the optical and mid-infrared typically provide information about 0.1–1 μm sized aerosols, while the near-infrared to mid-infrared wavelengths usually provide information about gaseous absorption. Strong gaseous absorption features in the infrared can remain visible, even when clouds and hazes are flattening the optical and near-infrared portion of the spectrum that is currently observable. For some combinations of aerosol properties, temperature, and surface gravity, one can make a precise measure of metallicity despite the presence of aerosols, but more often the retrieved metallicity of a cloudy or hazy atmosphere has significantly lower precision than for a clear atmosphere with otherwise similar properties. Future efforts to securely link aerosol properties to atmospheric metallicity and temperature in a physically motivated manner will ultimately enable a robust physical understanding of the processes at play in cloudy, hazy exoplanet atmospheres.

Unified Astronomy Thesaurus concepts: Exoplanet atmospheres (487); Exoplanet atmospheric composition (2021); Exoplanets (498)

1. Introduction

Theories for utilizing the wavelength dependence of transit depths to learn about exoplanet atmospheres arose soon after the first detection of a transiting exoplanet (Seager & Sasselov 2000; Brown 2001; Hubbard et al. 2001), and it was not long before transit spectroscopy enabled the first detection of an exoplanet atmosphere (Charbonneau et al. 2002). Since then, many studies have applied Bayesian techniques to estimate atmospheric properties, successfully detecting individual molecules and estimating water abundances (see Madhusudhan 2018 and Barstow & Heng 2020 for recent reviews). Today, sparse multi-wavelength transit measurements have been done for ∼100 planets, with more thorough wavelength coverage for a subset of ∼30.[1] Eventually, it is hoped that enough measurements can be made to search for overarching patterns in the abundances, metallicities, and C/O ratios of exoplanets which can be used to test theories of planet formation, migration, and subsequent evolution (Öberg et al. 2011; Pisoet al. 2016).

Some researchers have already started to use the small sample of transit spectra to discern patterns across planet mass and levels of stellar irradiation (Iyer et al. 2016; Sing et al. 2016; Barstow et al. 2017; Fu et al. 2017; Fisher & Heng 2018; Tsiaras et al. 2018; Pinhas et al. 2019; Wakeford et al. 2019; Welbanks et al. 2019), but it is generally expected that more reliable results will come when the upcoming James Webb Space Telescope (JWST) and the Atmospheric Remote-sensing Infrared Exoplanet Large-survey (ARIEL) expand the size and quality of available transit spectroscopy (Burrows 2014). These two missions are complementary by design. The JWST will observe tens of transiting exoplanets from 0.6 to 30 μm (Stevenson et al. 2016). It will have native spectral resolutions ranging from order $R \sim 100$ s to 1000 s which can be rebinned to trade off between supernova remnant (SNR) and spectral information. This mission reaches out to much longer wavelengths than was previously possible with the Hubble Space Telescope and the Spitzer Space Telescope (Spitzer) and greatly improves the spectral resolution, especially at longer wavelengths. ARIEL will have the ability to observe from 2.0 to 7.8 μm with a spectral resolution of R∼100 (Puig et al. 2016). This satellite is dedicated solely to exoplanet science, so it will survey a much larger sample than the JWST (around 1000 transiting planets, Tinetti et al. 2018). One core goal of ARIEL is to measure the mass–metallicity relationship of exoplanets (Zellem et al. 2019).

The future for transit spectroscopy looks very fruitful, but the method has some inherent challenges and limitations which we must work to overcome in order to realize the full promise of missions like the JWST and ARIEL. Foremost among these is the reality that the slant geometry of transit spectroscopy makes this type of observation particularly sensitive to the presence of even trace amounts of aerosols in the upper atmosphere of the target exoplanet (Fortney 2005). Note that,

[1] https://exoplanetarchive.ipac.caltech.edu

throughout this paper, we will adhere to the custom of referring to condensing species as *clouds*, photochemically formed species as *hazes*, and using the term *aerosol* to encompass both. Initially, it was thought that the high temperatures of most exoplanets studied with transit spectroscopy would prevent clouds from forming. This notion turned out to be erroneous; the exoplanets observed so far exhibit a range of behavior from densely cloudy or hazy to completely clear (Charbonneau et al. 2002; Lecavelier Des Etangs et al. 2008; Kreidberg et al. 2014; Sing et al. 2016; Louden et al. 2017). In fact, Wakeford et al. (2019) used the statistics of aerosol effects in current transit spectroscopy to demonstrate that, if the currently available transit spectra are a representative sample, then observers proposing for time with the JWST should anticipate signal sizes that are 30% reduced from what one would see if atmospheres were clear.

When clouds or hazes are present, they make it more difficult to measure chemical abundances with current retrieval models. Clear atmospheres produce spectra with large variations in transit depth with wavelength, on the order several gas-pressure scale heights. Absorption and scattering by clouds and hazes can fill in the gaseous absorption windows, shrinking the size of the transit spectroscopy "signal." Furthermore, properties like metallicity are more easily inferred from chemical abundances if one only needs to account for gas-phase chemistry rather than coupling gas-phase chemistry to the microphysics and/or photochemistry of aerosols (Woitke et al. 2018; Helling 2019). For observations like those currently available (i.e., sparse coverage from optical to near-infrared (NIR)), models accounting for a gray absorber and a varying optical slope have been adequate to marginalize over aerosol effects and obtain unbiased measurements of a planet's temperature and abundances (Mai & Line 2019; Barstow 2020). These measurements of abundances and temperature may be unbiased, but they are generally much less precise when thick hazes or clouds are present than for clear atmospheres (Barstow et al. 2017; Fisher & Heng 2018; Tsiaras et al. 2018; Wakeford et al. 2018; Pinhas et al. 2019).

It is hoped that the additional long-wavelength coverage of the JWST and ARIEL will finally allow us to learn more about cloudy and hazy exoplanet atmospheres because there are stronger gaseous absorption features in the MIR–mid-infrared (midIR) that may be visible above cloud or haze layers, and there may be distinctive spectral features in the midIR arising from resonance modes within the aerosols themselves (Budaj et al. 2015; Wakeford & Sing 2015; Pinhas & Madhusudhan 2017; Kitzmann & Heng 2018). If we can use transit spectra to identify which aerosol species are present and to constrain detailed size distributions, then this empirical information may even help refine efforts to model aerosol microphysics in detail (Helling 2019 review the state of the art for exoplanet cloud modeling; Kawashima & Ikoma (2018) provide an example of modeling photochemical haze formation in exoplanets). Eventually, if fast and accurate retrieval models can be developed which couple depletion and enrichment from clouds and hazes to gas-phase chemistry, then their presence need not hinder researchers from making accurate and precise measurements of chemical abundances, eventually uncovering chemical trends left by the processes of planet formation and evolution. Retrieved information from such transit spectra could even teach us surprising and interesting things about microphysics and photochemistry in alien environments (Helling 2019). This reasoning forms the basic motivation for our study.

In this work, we explore how well properties of the aerosols themselves can be constrained with JWST-like transit spectra, and to what extent adding longer wavelength coverage enables better measurements of metallicity and temperature, even in the presence of clouds or hazes. Our goal is to build an intuitive sense of how the temperature, mass, and metallicity of an exoplanet and the physical properties of any aerosols in its atmosphere translate into the shape of the full transit spectrum. We use the following questions to direct us:

1. Which JWST wavelengths contain the most information about aerosol properties and which provide information about gaseous absorption?
2. How well can we recover atmospheric metallicities and temperatures, even when aerosols are present as we extend the wavelength coverage of transit spectra?
3. Can we uniquely identify which dominant aerosol species are present in atmospheres using JWST transit spectroscopy?
4. Can we constrain the size distribution of aerosols?
5. How do these tasks differ for condensed clouds and photochemical hazes?

Section 2 describes our methods and discusses which aerosol species we consider. We use the recently developed code Multi-dimensional Exoplanet TransIt Spectroscopy (METIS; Lacy & Burrows 2020) to carry out Markov chain Monte Carlo (MCMC) retrievals, compute transit contribution functions, and conduct studies of model parameter sensitivity. Section 3 presents the four fiducial planets we use to anchor our study, which range in temperature from 700 to 1800 K in order to explore a range of possible condensate species for warm and hot exoplanets. Section 4 demonstrates that the additional long-wavelength coverage of the JWST (and, to a lesser extent, ARIEL) will allow one to probe gas-phase molecules in the near–midIR and aerosol properties at optical and midIR wavelengths. In Sections 5 and 6 we use MCMC experiments to test how well aerosol species can be distinguished and how well particle distributions can be recovered. In Section 5 we incorporate aerosols as a uniform slab at an arbitrary pressure, a method suitable for either hazes or clouds. In Section 6, we place a cloud base where the Clausius–Clapeyron line and the temperature–pressure profile intersect, and then have the cloud taper off. This phase equilibrium approach is suitable for condensing clouds. We summarize and draw our conclusions in Section 7.

2. Methods

The code used throughout this work, METIS, is described in Lacy & Burrows (2020), but we will review the important points here for the reader's convenience and go into more detail on the aerosol parameterizations. The code takes in an arbitrary latitude–longitude–altitude grid of temperatures and pressures along with an atmospheric metallicity and returns the corresponding transit spectrum. It assumes thermochemical equilibrium to assign the correct opacity and mean molecular weight to each grid point and assumes the ideal gas law to assign the appropriate densities. In this paper our focus is on exploring a wide variety of aerosol behaviors rather than 3D effects, so we simply use isothermal atmospheres as the input grids for METIS. When computing these isothermal structures

Table 1
Summary of Aerosol Parameterizations

Name	Parameters	Meaning	Intended Aerosol Type
Slab	$P_{\rm top}$	Top-pressure cut-off	Condensing clouds
(Figure 1, right)	F	Fraction of available material that contributes to aerosol particles (by number)	or photochemical hazes
	a_m	Modal particle radius	
	σ_a	Size dispersion for log-normal	
Equilibrium Base	α	Ratio of gas scale height to aerosol particle scale height	Condensing clouds
(Figure 1, left)			
	a_m	Modal particle radius	
	σ_a	Size dispersion for log-normal	

Note. The spatial parameters could also be paired with other size distributions besides the log-normal parameters included here (a_m and σ_a). In addition to these parameters, both parameterizations need some properties of the assumed aerosol species. These are listed in Table 2 for the species considered in this work. The equilibrium base parameterization also requires a Clausius–Clapeyron line to locate the cloud base. In this work we use the curves shown in Figure 2.

we assume hydrostatic equilibrium and the ideal gas law. The atmospheres have constant temperature with altitude but varying surface gravity and varying mean molecular weight in a manner consistent with hydrostatic equilibrium and thermochemical equilibrium. We use a reference pressure, P_0, and reference radius, R_0, a planet mass at that radius, M_P, a metallicity, Z, and a temperature, T, as input to form the T–P structure of the atmosphere and assign the correct gaseous opacities.

We treat gaseous opacities by interpolating within precalculated tables of mixing ratios and matching premixed tables of total opacity to assign the correct mean molecular weight and opacity for any combination of temperature and pressure. The tables are created using the thermochemical equilibrium calculations described in Burrows & Sharp (1999) and Sharp & Burrows (2007), and opacity calculations as described in Sharp & Burrows (2007), with updated CH_4 opacities from Yurchenko & Tennyson (2014). The chemistry calculations begin with the solar abundances of all the atomic species as reported in Anders & Grevesse (1989), or the solar abundances scaled to a different value of Z. Z is defined in the typical way, as the mass fraction of material that is in any element heavier than He (metals in the astrophysical sense of the word). As Z changes, only the amount of H and He relative to all the metals changes. The relative amounts of all the different metals among themselves remain the same, and the ratio of H to He is also kept the same. It is common to vary the C/O ratio in addition to varying Z when assuming thermochemical equilibrium, but we always assume the C/O ratio remains at the solar C/O ratio. From this starting point, the chemical equilibrium calculations minimize the Gibb's free energy for a network of hundreds of species and reactions, recording mixing ratios for 30 important ions, atoms, and molecules in the chemistry tables across a grid of temperatures and pressures. The corresponding opacity tables have a grid in temperature and density, assuming an ideal gas equation of state to convert pressure to density. The opacity tables sum together opacities from 26 ionic, atomic and molecular sources, as well as from H_2–H_2 and H_2–He collision induced absorption (CIA). The opacity calculations and sources of laboratory data are described in detail in Sharp & Burrows (2007), with a convenient summary in Table 1 of that publication. We leave out the opacity from TiO and VO. Rayleigh scattering cross sections for the appropriate mixture of gases are provided in a separate table at the same temperatures and densities but only for a single reference wavelength of $\lambda_0 = 1\,\mu$m. This cross section is then scaled as $(\lambda/\lambda_0)^{-4}$. The reference cross sections are composed of an appropriately weighted average of the Rayleigh cross sections for H, He, H_2O, N_2, CH_4, NH_3, and CO, based on their mixing ratios in thermochemical equilibrium.

We employ a set of chemistry and opacity tables which span a range from sub-solar ($0.1 \times Z_\odot$) to around the metallicity of Jupiter ($3.16 \times Z_\odot$). By interpolating between these tables, we can perform MCMC retrievals of Z over this limited range of metallicities. Gaseous exoplanets and gaseous planets in the solar system have bulk metallicities which span over a larger range of metallicities than those considered here (Thorngren et al. 2016). Estimates of individual exoplanet metallicities based on analysis of their atmospheric properties remain highly uncertain for the most part and limited to a sample of only a few dozen targets. Nonetheless, Welbanks et al. (2019) use this sample to infer a mass–metallicity relation. Their mass–metallicity relation predicts that the ratio of planet metallicity to host star metallicity is under 1 for targets more massive than $\sim 0.2 \times M_{\rm J}$, with some scatter. If this relation bears out, then our range of $Z = 0.1 \times Z_\odot$–$3.16 \times Z_\odot$ is not infeasible for the hot Jupiters modeled here. However, we also model a smaller warm mini-Neptune with a mass of only 0.02 $M_{\rm J}$. It is likely that a planet of this size would have a metallicity higher than our maximum-allowed metallicity. There is also a lot of scatter in the measurements used by Welbanks et al. (2019) and in the work of Thorngren et al. (2016), so some larger planets could fall well above the mass–metallicity relation inferred by Welbanks et al. (2019). These trends indicate that our metallicity range ought to be expanded by several orders of magnitude to upwards of 100–$1000 \times Z_\odot$ to be ready for general application, especially if we wish to focus on smaller exoplanets in future work. When we discuss the results in more detail, we will come back to the limitations of the metallicity range, and what we expect to find in the MCMC results as we expand it.

When aerosols are included, we do not account for any corresponding changes to the gas-phase chemistry, so we are effectively assuming that the timescales for photochemical processes and condensation are long compared to gas-phase interactions and that replenishment of new material from deeper in the atmosphere keeps the gas phase unchanged. Alternatively, one could see this as an assumption that the amount of material tied up in aerosols is negligible compared to the gas-phase abundances of relevant atomic species.

Table 2
Summary of Aerosol Properties Used in Calculations

Aerosol Species	Bulk Density (g cm^{-3})	Molar Mass (g mol^{-1})	~Condensation Temperature (K)	Solar Mixing Ratio of Limiting Species	Source for Complex Indices of Refraction	Other Names
Al_2O_3	4.02	101.96	1500–2000	Al: 2.95×10^{-6}	(1)	Corundum
TiO_2	4.23	79.865	1500–2000	Ti: 9.77×10^{-8}	(1)	Anatase
Fe	7.874	55.845	1200–2500	Fe: 4.68e−5 $\times 10^{-5}$	(1)	Iron
Mg_2SiO_4	3.25	140.69	1200–2000	Mg: 3.8×10^{-5}	(1)	Forsterite
$MgFeSiO_4$	3.25	153.31	1200–2000	Fe: 4.68×10^{-5}	(1)	Olivine
$MgSiO_3$	3.2	100.387	1200–2000	Mg: 3.8×10^{-5}	(1)	Enstatite
NaCl	2.16	58.44	900–1600	Cl: 3.16×10^{-7}	(1)	Table Salt
Na_2S	1.86	78.0452	700–1200	S: 1.62×10^{-5}	(1)	…
KCl	1.98	74.551	700–1000	K: 1.32×10^{-7}	(1)	Sylvite
H_2O	0.997	18.02	200–300	O: 8.51×10^{-4}	(1)	Water Ice
NH_3	0.8	17.031	100–200	N: 1.12×10^{-4}	(2)	Ammonia Ice
…	~0.687	~27.0253	…	N: 1.12×10^{-4}	(3)	Titan Tholins
$(HCN)_X$	0.687	27.0253	…	N: 1.12×10^{-4}	(4)	poly-HCN
$C_{14}H_{10}$	1.25	178.23	…	C: 3.63×10^{-4}	(5)	Carbonaceous Soot
C_4H_8	0.588	56.106	…	C: 3.63×10^{-4}	(6)	Biomass Burning (vegetation)
C_3H_8	0.493	44.1	…	C: 3.63×10^{-4}	(7)	Biomass Burning (propane)

Note. (1) Kitzmann & Heng (2018), (2) Robertson et al. (1975), (3) Khare et al. (1984), (4) Khare et al. (1994), (5) Chang & Charalampopoulis (1990), (6) Sutherland & Khanna (1991), (7) Wu & Cheng (2016).

2.1. Aerosol Parameterizations

We incorporate aerosol opacity using Mie theory, log-normal size distributions, and two options for specifying the spatial positions of particles in the atmosphere. We call these two forms of aerosol the "slab" and the "phase equilibrium cloud." In both the slab and the phase equilibrium cloud, the maximum possible amount of aerosol that can be incorporated into the atmosphere is limited to an amount consistent with the solar abundances reported by Anders & Grevesse (1989) scaled by the overall metallicity of the atmosphere, Z. For a given layer of atmosphere with pressure P and temperature T we ensure that the aerosol satisfies this equality:

$$n_{\rm tot}(P,\,T)\frac{X_{\rm lim}(Z)}{n_{\rm stoich}}f_{\rm shape}(P,\,T) = \int_0^\infty \frac{\rho_{\rm part}4/3\pi a^3}{\mu_{\rm mol}}n(a)da. \quad (1)$$

On the left-hand side, $n_{\rm tot}$ is the number density of all gaseous molecules, $X_{\rm lim}$ is the molar mixing ratio of limiting atomic species that goes into the aerosol species of interest, $n_{\rm stoich}$ is the number of limiting atomic species atoms needed to make one molecule of the aerosol species, and $f_{\rm shape}$ is an additional factor that can be manipulated to impose the slab and phase equilibrium cloud parameterizations. On the right-hand side, $\rho_{\rm part}$ is the solid or liquid bulk density of the aerosol species, $\mu_{\rm mol}$ is the mass of an individual molecule of the aerosol species, and $n(a)$ is the particle-size distribution. The fraction within the integral is an expression for the number of aerosol molecules which go into making one spherical aerosol particle with radius a. Throughout this work we assume the values of species bulk density and molar mass given in Table 2. Note that $X_{\rm lim}$ is not a mixing ratio of the limiting atomic species in the pure gas phase, but rather of the limiting atomic species present in any molecule. We compute this factor based on the solar mixing ratios listed in Table 2 and the assumed metallicity of the atmosphere. $n_{\rm stoich}$ can be inferred from the first column of the table. $f_{\rm shape}$ is limited to range from 0 to 1. If $f_{\rm shape}$ is 1 throughout the whole atmosphere, then all of the available material would be used to form particles with the size distribution specified by $n(a)$. Using all of the "available material," would mean every single atom of the limiting species were bound up into the aerosol rather than incorporated into other gaseous species. The material is not available in the sense that it would be energetically favorable for it to condense, but it is available in the sense that those atoms are somewhere in the atmosphere. When we talk about fractions of available material, it is based on number fractions of this limiting species of atom.

Ensuring that Equation (1) is true amounts to identifying the correct normalization for the chosen particle-size distribution $n(a)$. Once this normalization factor is determined for each T–P point, we can use the particle-size distribution to sum up the appropriate total aerosol opacity at each T–P point. We do this summation using precomputed tables of extinction cross sections as a function of wavelength and particle size as described in Lacy & Burrows (2020). We employ log-normal particle-size distributions throughout this work, so we always adopt:

$$n(a) = \frac{N_{P,T}}{\sqrt{2\pi}}\frac{1}{\ln(\sigma_a)}\frac{1}{a}\exp\left[\frac{-(\ln(a)-\ln(a_m))^2}{2\ln(\sigma_a)^2}\right], \quad (2)$$

where σ_a dictates the width of the size distribution and a_m sets the modal particle size. $N_{P,T}$ is the normalization factor that can be chosen to make the equality in Equation (1) hold true. The slab and phase equilibrium cloud could be paired with different particle-size distributions, so long as the distribution is normalized to ensure that Equation (1) holds.

The parameters dictating the slab and phase equilibrium parameterizations are summarized in Table 1 and portrayed visually in Figure 1. The table and figure are replicated from

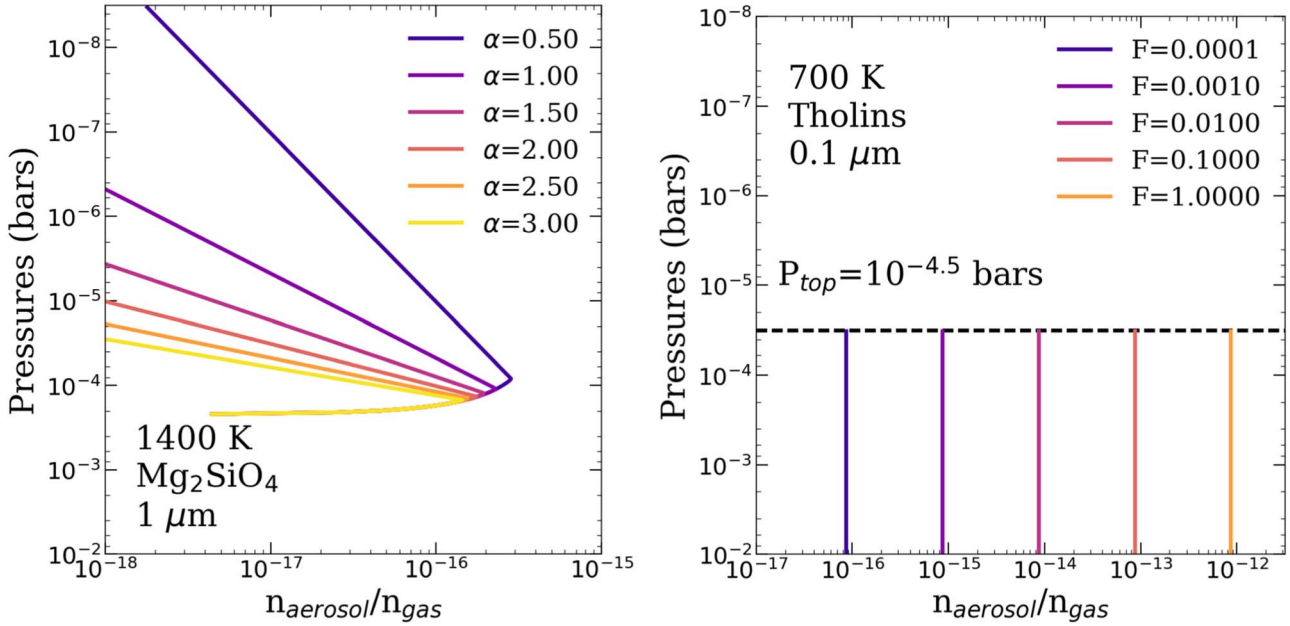

Figure 1. Demonstration of the meaning of parameters describing the spatial positions of aerosols. Each panel shows the ratio of the number density of aerosol *particles* to number density of gas particles as a function of pressure level. Each aerosol particle is made up of many molecules of a given aerosol species, calculated assuming spherical particles and the densities and masses in Table 2. The left panel shows an equilibrium cloud with varying values of α and the right panel shows a slab with varying values of F. The equilibrium cloud examples assume a forsterite cloud with 1 μm particles in a 1400 K isothermal atmosphere. The slab examples assume a tholin haze with 0.1 μm particles in a 700 K isothermal atmosphere and a top-pressure cut-off of $10^{-4.5}$ bar marked by a black dashed line. In both cases we assumed the atmosphere had a solar metallicity, that is $Z = 1 \times Z_{\odot}$.

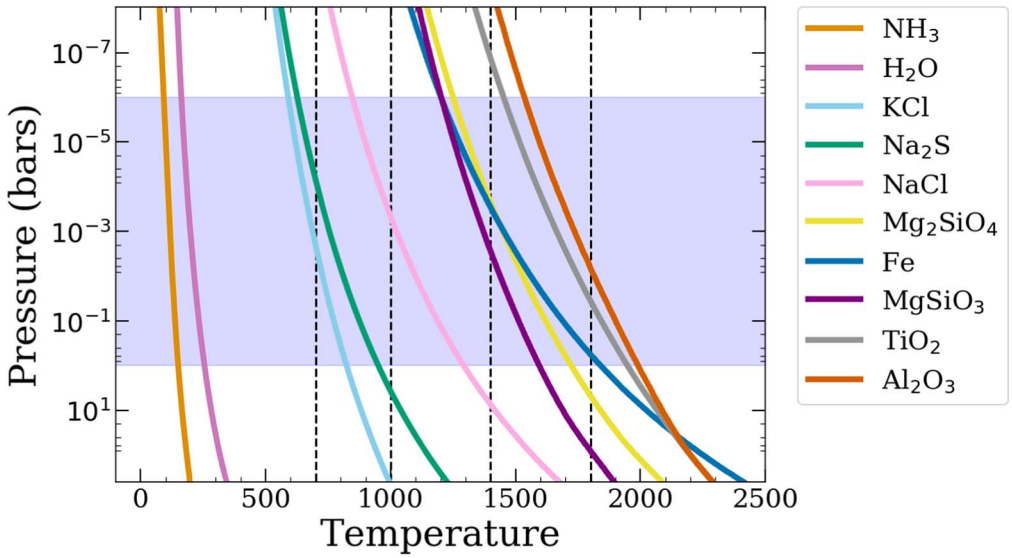

Figure 2. Clausius–Clapeyron lines for the condensed aerosol species included in this work (Sudarsky et al. 2003; Morley et al. 2012; Gao & Benneke 2018). These curves are calculated for solar-metallicity atmospheres. The shaded blue region indicates the range of pressures typically probed by transit spectroscopy. The black dashed lines denotes four fiducial temperatures which we consider throughout this work. In our equilibrium cloud aerosol parameterization, we assume aerosols condense when the T–P profile and Clausius–Clapeyron line intersect. Note that typically a T–P profile for an atmosphere would have a steeper temperature dependence on pressure than the Clausius–Clapeyron lines.

Lacy & Burrows (2020) for the reader's convenience. We will discuss how to formulate $f_{\rm shape}$ for the slab first, and then the phase equilibrium cloud.

For the slab aerosol, $f_{\rm shape}(P, T)$ is very simple (right panel of Figure 1). $P_{\rm top}$ sets a top-pressure cut-off above which no particles form or remain for long, even if there is sufficient material to form them. So, if P is less than $P_{\rm top}$, then $f_{\rm shape}(P, T) = 0$. For deeper pressures, $f_{\rm shape}(P, T) = F$. F simply sets the fraction of available material that winds up bound into cloud or haze *particles* as a fraction of the number of aerosol *molecules*. Note that this parameterization has no reliance on the Clausius–Clapeyron line whatsoever.

The phase equilibrium cloud parameterization (left panel of Figure 1) imposes a profile $f_{\rm shape}$ which trades off between including the material in excess of the saturation vapor pressure near the base of the cloud (see the curved base of the cloud profile) and a tapering off from the maximum-allowed material toward the top of the cloud (see the power-law decrease in the upper part of the cloud profile). The Clausius–Clapeyron line defines the saturation vapor pressure as a function of temperature (see Figure 2 for the

ones adopted in this work). Computing this line depends on thermodynamic properties of the material in question, like the latent heat of the phase transition from gas to liquid and the change in specific volume. We use the Clausius–Clapeyron line to locate a physically feasible base pressure of the cloud and to determine how much material is in excess of the saturation vapor pressure at each pressure level above the cloud base. Applying this parameterization consists of the following steps:

1. First, identify the pressure level of the cloud base where the Clausius–Clapeyron line and the T–P profile of the atmosphere intersect. If we denote the Clausius–Clapeyron line as $P_{cc}(T)$, this intersection will occur at a point on the T–P profile (T, P) where $P_{cc}(T) = P$. Call this level P_{base} and its corresponding temperature T_{base}. At (T_{base}, P_{base}) the amount of aerosol vapor in the atmosphere is equal to the saturation vapor pressure.
2. Second, compute the amount of material in excess of the saturation vapor pressure for levels above the cloud base. We approximate the number density of particles in excess of saturation vapor pressure as $n_{excess}(P, T) = n_{tot}(P, T)\frac{X_{lim}(Z)}{n_{stoich}} \times \left(1 - \frac{P_{cc}(T)}{P}\right)$. One can thus use $f_{shape}(P, T) = (1 - P_{cc}(T)/P)$ in Equation (1) to impose the desired limit. This is only an approximation since a true calculation would need to use the mixing ratio of the actual aerosol species vapor, not just the limiting atomic species. We are forced to make this approximation because our chemistry tables do not track most of the aerosol species considered here.
3. Third, compute the attenuation of cloud particles given the free parameter, α. For this we set $f_{shape}(P, T) = (P/P_{base})^{\alpha}$. Larger values of α make for a more compressed cloud and smaller values of α make for a more extended cloud.
4. Finally, to put the whole cloud profile together, at each T–P level we compare the material in excess of the saturation vapor pressure, $f_{shape}(P, T) = (1 - P_{cc}(T)/P)$ to the attenuation by the cloud scale height, $f_{shape}(P, T) = (P/P_{base})^{\alpha}$, and select the minimum f_{shape} for that T–P point. Then we use this value of f_{shape} to normalize the particle-size distribution such that Equation (1) holds.

Note that, if we applied only $f_{shape}(P, T) = (P/P_{base})^{\alpha}$ all the way down to P_{base} and ignored step 2, it would set $f_{shape}(P_{base}, T_{base})$ to 1. All of the available material based on the limiting atomic species would be bound up into aerosol particles at the cloud base, and then, from there, the relative number density of aerosol particles to gaseous species would immediately decrease. On the other hand, if we set α to zero, so only $f_{shape}(P, T) = (1 - P_{cc}(T)/P)$ is in effect, the fraction of available material incorporated into the cloud particles will increase until it reaches the maximum possible amount. The competition of these two effects combines to set the maximum fraction of available material that is bound up into the cloud. See how in the left panel of Figure 1 the clouds with different values of α reach slightly different maximum ratios of $n_{aerosol}/n_{gas}$. In this way we can avoid introducing an additional free parameter like F. Since the focus of this work is to explore a broad range of aerosol-related parameter space, we adopt the simplification of isothermal T–P profiles throughout. Unfortunately, this introduces some hiccups for the phase equilibrium cloud parameterization. Typically, the Clausius–Clapeyron line has a much steeper temperature dependence than the T–P profile. This means that usually $P_{cc}(T) < P$ for pressure levels lower than the cloud base pressure (higher altitudes), so there is an excess of material above saturation vapor pressure above the cloud base. This assumption is folded into step 2 above. In an isothermal T–P profile, $P_{cc}(T) > P$ for pressure levels higher up than the cloud base, so above P_{base} there is actually a dearth of material rather than an excess. One option to deal with this would be to ignore step 2 and jump right to step 3, adding in an additional free parameter F_{base} from which to have the cloud attenuate. But we wanted to still implement cloud profiles with the desired qualitative shape and order-of-magnitude optical thickness as the phase equilibrium would produce in an atmosphere with a non-isothermal, non-inverted T–P profile in the same temperature range. To attain this, we use $f_{shape}(P, T) = (1 - P/P_{cc}(T))$ rather than $f_{shape}(P, T) = (1 - P_{cc}(T)/P)$. This fudge is not entirely befitting of the moniker "phase equilibrium cloud," but it enables us to reach our desired goals without altering the isothermal T–P profiles.

Exploring both these forms of aerosol captures a wide range of likely behavior for photochemical hazes and condensing clouds, and demonstrates the advantages and disadvantages of applying retrieval models which favor incorporating physical assumptions versus maximizing flexibility. Our two forms of aerosol are complimentary in this sense. The slab aerosol is flexible, and, as such, should be able to replicate a wide range of haze or cloud behavior seen in nature, provided the correct aerosol species is used. One could even increase the flexibility by adding a free base pressure for the slab rather than having the slab always extend deep into the atmosphere. Flexibility is good for retrieval models, since one wants data to shape conclusions rather than preconceived notions. However, we do have many examples of clouds in our own solar system and ground-truth laboratory measurements of the temperatures and pressures at which substances can condense. The phase equilibrium cloud parameterization makes some strong, but physically motivated, assumptions. Condensing clouds in the solar system tend to have their base around the intersection between the Clausius–Clapeyron line and the T–P profile, and they tend to have a smaller scale height than the gas-pressure scale height (Sánchez-Lavega et al. 2004).

There are a number of retrieval tools for transit spectra which account for clouds and hazes.[2] Barstow & Heng (2020) and Barstow et al. (2020) provide a recent review of retrievals and a direct comparison of results found with different aerosol parameterizations. Cloud and haze parameterizations usually involve some subset of the following: a single cloud opacity if the cloud is gray or an initial cloud opacity that will then be scaled with wavelength according to some rule if the cloud is non-gray, a specified range of pressures where the cloud will be present, a single particle size, and a scattering index (Barstow et al. 2017; Fisher & Heng 2018; Tsiaras et al. 2018; Mai & Line 2019; Pinhas et al. 2019; Ormel & Min 2019). We take a slightly different approach in order to incorporate the actual complex indices of refraction from whichever aerosol species is used, along with a full log-normal size distribution not just a single particle size. These choices are necessary to answer one

[2] Some examples of transit retrieval codes which allow aerosols include: NEMESIS (Irwin et al. 2008), POSEIDON (MacDonald & Madhusudhan 2017), PyRat-Bay (Cubillos et al. 2017), BART (Blecic et al. 2017), SCARLET (Fraine et al. 2014), CHIMERA (Line et al. 2013), τ-REx (Waldmann et al. 2015).

of our motivating questions: will the JWST and ARIEL be able to distinguish between potential aerosol species? We also formulate our clouds and hazes such that we never put in a cloud or haze that has an impossibly large total mass of aerosol for a chosen metallicity and aerosol species. In the slab model, F sets a fraction of *available material* which will be incorporated into the haze or cloud, and the phase equilibrium assumption that only material in excess of saturation goes into cloud particles can only reach the total available material at maximum. As Barstow et al. (2020) point out, it will ultimately be most informative to conduct retrievals on transit spectra with several different aerosol parameterizations that have made different assumptions and then consider where the results agree and where they disagree and why.

One limitation of our cloud and haze models is that they assume a single dominant species of aerosol, and they use a single log-normal particle-size distribution throughout the whole cloud or haze regardless of altitude. Detailed one-dimensional microphysical models and models coupling microphysics to three-dimensional global circulation models (GCMs) indicate that condensed clouds likely have larger particles at their base and smaller particles near the upper boundary and that the chemical makeup of the clouds will vary with altitude and about the heterogeneous surface of highly irradiated exoplanets (Parmentier et al. 2016; Powell et al. 2019; Helling 2019; Helling et al. 2019). If the cloud or haze in a target's atmosphere is not well approximated by a single species and log-normal size distribution, then our cloud and haze models will likely fail to find a good fit or retrieve misleading results. Another limitation of our cloud and haze models is that we assume that the cloud or haze is uniformly present about the whole limb of the planet. This has been shown to return biased results (Line & Parmentier 2016; MacDonald & Madhusudhan 2017), so in order to apply our methods to real data we would need to adjust the model to account for patchiness. These limitations do not interfere with the purposes of this study because we are using simulated transit spectra and retrieval experiments on these synthetic observations to assess whether it is feasible that certain types of information could be embedded in JWST and ARIEL transit spectra rather than carrying out retrievals on actual data. This could be thought of as an upper limit of sorts. If information about aerosol species and particle-size distributions cannot be retrieved given our assumptions, then it will be even more difficult to do so when these assumptions are relaxed. If information can be retrieved, then this is a promising first step and further studies are warranted which include particle-size distributions and the full spectrum of the complex index of refraction in more complicated models. For example, one way to incorporate a varying size distribution with altitude is to apply the model suggested by Ackerman & Marley (2001), which balances gravitational settling with a parameterized turbulent upwards mixing strength to determine the modal particle size at each level.

2.2. Aerosol Species

The species of aerosols present in exoplanet atmospheres remains a mystery given our current observational capabilities. When fitting current data, it is generally sufficient to include an unidentified flat gray absorber and an optical slope along with gaseous opacity sources (Mai & Line 2019; Barstow 2020; Barstow et al. 2020). This gives us a hint at the presence of both smaller and larger sized particles, but provides no smoking-gun signature of which set of species is present. In theory, transit spectra should be able to provide more information about aerosols because the effect of aerosols on a planet's transit spectrum depends on the optical properties of the aerosol species, the full size distribution of particles, where in the atmosphere the particles have formed, and how the presence of the aerosol affects the gaseous abundances of major absorbers (e.g., Budaj et al. 2015). However, within a narrow wavelength range, these different degrees of freedom can be degenerate and conspire to shape transit spectra in similar ways, even when species and size-distributions vary. Researchers have thus been left to make educated guesses as to what species are present. Expanding on the work of Lecavelier Des Etangs et al. (2008), Vahidinia et al. (2014) demonstrated that an inflection point in a Rayleigh scattering slope, as is present for HD189733b, can indicate that a transit spectrum is probing both above and below a cloud or haze deck. If present, this feature can narrow down the possible condensate species by constraining the cloud base to a specific point on the inferred atmospheric T–P profile. They applied their model to the transit spectrum of HD189733b, but data was not yet of a quality to provide unambiguous results.

After considering the large body of work positing which aerosol species are likely to be present, we have chosen to consider an extensive though not exhaustive list of 15 candidates in our study. These are listed in Table 2 and the corresponding indices of refraction and extinction efficiencies for 0.1, 1 and 10 micron particles are shown in Figures 19 and 20 in the Appendix. For condensing species, we include NH_3, H_2O, KCl, Na_2S, NaCl, Mg_2SiO_4–Fe_2SiO_4 sequence, $MgSiO_3$–$FeSiO_3$ sequence, Fe, TiO_2, and Al_2O_3. This leaves out many of the species that have been considered, but includes those considered most likely to form based upon microphysical modeling (Helling 2019; Gao et al. 2020), brown dwarf spectral modeling (Leggett et al. 1998; Ackerman & Marley 2001; Tsuji 2002), and the clouds and hazes seen on solar system planets (Marley & Robinson 2015). The condensation curves for these species are shown in Figure 2. For photochemical hazes, we include Titan tholins, poly-HCN, a soot from propane burning, a PAH-dominated soot, and a soot resulting from burning vegetation. These are not predicted to be the exact hydrocarbon hazes present in exoplanet atmospheres (He et al. 2018a; He et al. 2018b; Hörst et al. 2018), but they represent a range of plausible optical properties. These species are chosen mainly because they had readily available lab measurements of refractive indices across the wavelengths of interest. For the interested reader, we include a brief summary of the literature surrounding the likely makeup of exoplanet aerosols in the remainder of this section.

The natural place to start is to estimate the temperatures of objects and then consider which molecules made of available atomic species can exist at those temperatures. Looking purely at volatility, a number of studies have compiled lists of ∼30–40 candidate species that might exist at temperatures of 700–2500 K and have readily available lab measurements of complex indices of refraction (Sudarsky et al. 2003; Morley et al. 2012; Budaj et al. 2015; Wakeford & Sing 2015; Kitzmann & Heng 2018). Modeling transit spectra which include these aerosols shows that, for some species, relatively strong resonance features may show up in the continuous NIR–IR coverage of the JWST (Wakeford & Sing 2015; Parmentier et al. 2016; Pinhas & Madhusudhan 2017; Mai & Line 2019). It will all depend on which species are present,

Table 3
Priors Used in MCMC Retrievals

Parameter	Prior	Description
P_0	0.01 bar $< P_0 <$ 10 bar	Reference pressure corresponding to known radius
Z	$0.1 < Z/Z_\odot < 3.16$	Bulk metallicity
T	50 K $< T <$ 5000 K	Temperature
a_m	0.001 μm $< a_m <$ 100.0 μm	Modal particle size
σ_a	$1.0 < \sigma_a < 50.0$	Width of log-normal particle-size distribution
α	$0.001 < \alpha < 100$	Ratio of aerosol scale height to gaseous scale height
$P_{\rm top}$	10^{-7} bar $< P_{\rm top} < P_0$	Top-pressure cut-off of aerosol
F	$0 < F < 1$	Fraction of available material bound up in aerosol

Note. In many cases transit spectra probe below the reference pressure and reference radius, so our assumption of $P_{\rm top} < P_0$ would be a poor one. However, for all the fiducial atmospheres explored in this study the reference pressure and radius are well below where the atmosphere has become opaque to all wavelengths. A follow up study without this prior may reveal some degeneracies avoided in this work.

their sizes and altitudes in atmospheres. Such studies have lead to the expectation that the higher SNR and broader wavelength coverage of future transit spectroscopy with the JWST and ARIEL could allow us to identify which species are present in many cases.

Other researchers have sought to winnow or rank this list of candidates by considering microphysical models of haze and cloud formation and the subsequent evolution of particle sizes and lifetimes in dynamic atmospheres (Zahnle et al. 2016; Lavvas & Koskinen 2017; Kawashima & Ikoma 2018; Kawashima & Ikoma 2019; Helling 2019; Helling et al. 2019; Powell et al. 2019; Gao et al. 2020). For condensate species, several studies find that TiO_2 is energetically the most likely to form via pure condensation (Helling et al. and Powell et al. Woitke Gao), while other species likely need seed particles. However, there is likely very little Ti in most atmospheres (Anders & Grevesse 1989). It may be that TiO_2 forms seeds which other aerosols condense onto. In that case, such aerosols would likely incorporate the optical properties of their outer layers rather than their tiny core of TiO_2 (Powell et al. 2019). Gao et al. (2020) predict that planets with temperatures below 900 K will predominantly form photochemical hazes, planets with temperatures above 2000 K will be clear, and in between silicate clouds will dominate. When it comes to photochemical hazes, the list of possible species and mixes of species grows significantly. While the exact chemical mix of haze particles is hard to predict, it is widely agreed that any hazes will be dominated by hydrocarbons (Kawashima & Ikoma 2018; Adams et al. 2019; Gao et al. 2020). This is because the exoplanets probed by transit spectroscopy tend to be warm (typically 500–1000 K), and receive a large amount of UV irradiation. If the atmospheres are CH_4-dominated rather than CO-dominated, this is a perfect environment for hydrocarbon hazes to form easily through photochemical reactions triggered by photodissociation of methane (e.g., Yung et al. 1984). Theoretical studies have modeled haze production rates under different physical conditions and assumptions about metallicity and levels of UV flux, and assessed the effect on transit spectra (Kawashima & Ikoma 2018; Kawashima & Ikoma 2019; Kawashima et al. 2019). Lab work is beginning to experiment with what types of hazes result as temperatures and input abundances vary (He et al. 2018a; He et al. 2018b; Hörst et al. 2018); however, optical properties are not yet available for the resulting hydrocarbon mixtures.

These types of detailed and approximate microphysical models have proven useful in studying clouds and hazes on Earth and elsewhere in the solar system, but their adaptation to exoplanets is still in its infancy (Helling 2019; Powell et al. 2019; Gao et al. 2020). So far they have been mainly limited to making predictions (e.g., Powell et al. 2019 predict observable effects from morning-evening asymmetries for hot Jupiters), but the data of the JWST and ARIEL should start to test these predictions. If we can obtain credible empirical measures of aerosol properties from observations (species, size distributions, spatial positions), then detailed microphysical models can provide profound insight into the physical processes at work.

Other hints at the makeup of exoplanet clouds arise from inferences of condensates appearing and disappearing as temperatures change. Examples include the off-set peaks in some optical phase curves of hot Jupiters (Parmentier et al. 2016), the appearance and disappearance of reflective clouds on the elliptically orbiting Kepler-434b (Dittmann et al. 2020), and the strengthening and weakening of Fe lines in ultra high resolution spectroscopy WASP-76b (Ehrenreich et al. 2020). These works postulate MgS, KCl, NaCl, and condensates which contain Fe.

2.3. Simulated Data, Retrieval Framework, and Bayesian Information Criterion

We simulate data reminiscent of the JWST by binning our transit spectra to $R\sim100$ from 0.7 to 12 μm. This is recommended by Greene et al. (2016) as an optimal compromise between SNR and spectral information. For noise, we take the Pandexo[3] errors for HD209458b with NIRISS, NIRCam I and II, MIRI to get the single-transit depth precision. These are then scaled by $\sqrt{N_{\rm obs}}$ to represent the desired number of transit observations and added in quadrature with the systematic noise floors suggested in Greene et al. (2016). The noise floor ranges from 20 ppm for NIRISS, 30 ppm for NIRCam, up to 60 ppm for MIRI.

We use `emcee`, a pure Python implementation of Goodman & Weares affine invariant MCMC ensemble sampler, to carry out retrievals with METIS providing forward models and the aerosol parameterizations described in Section 2.1. Each chain is run to have a total length of 140,000 steps, which proved adequate for converged fits. During these retrievals we use the priors summarized in Table 3.

In order to determine which aerosol species is preferred for each simulated transit spectrum, we compute the Bayesian

[3] https://exoctk.stsci.edu/pandexo/

Table 4
Model Parameters, Signal-size Estimates, and the Aerosol Species Considered for Our Four Fiducial Atmospheres

T (K)	M (M_J)	P_0 (bar)	R_0 (R_J)	Z ($Z_\odot$)	R_* ($R_\odot$)	Reference Transit Depth: $(R_0/R_*)^2$	Scale Height Δ Depth	Possible Aerosols
1800	1.0	1.0	1.5	3.0	1.0	23,000 ppm	440 ppm	Fe, TiO_2, Al_2O_3, hazes
1400	1.0	1.0	1.2	3.0	1.0	15,000 ppm	180 ppm	Mg_2SiO_4, $MgSiO_3$, Fe, hazes
1000	1.0	1.0	1.0	3.0	1.0	10,000 ppm	70 ppm	Na_2S, NaCl, hazes
700	0.0203	1.0	0.2389	3.0	0.2064	14,000 ppm	800 ppm	Na_2S, KCl, hazes

information criterion (BIC) for each candidate aerosol (reported in Tables 5–8). To compute BIC values we take the median values of each parameter from the finished MCMC chains as an initial guess and run a bounded optimization of the likelihood function using `scipy.optimize`. The BIC is then taken to be:

$$\mathrm{BIC} = k\ln(n) - 2\ln(L), \tag{3}$$

where k is the number of parameters in the model, n is the number of wavelength bins in the transit spectrum, and L is the model transit spectrum which maximizes the likelihood function. A lower BIC value indicates that one model is preferred over another. Note that, given the number of parameters in each model and the number of wavelength bins simulated to attain approximate JWST-like observations, the BIC value for a given model and data set can only reach a minimum of $k\ln(n)$. When we use the slab-shaped aerosol the minimum possible BIC is ∼39.5, and for the phase equilibrium cloud the minimum possible BIC is ∼33.8.

3. Fiducial Atmospheres When Clear

Before we present the main findings of this study (focused on the promising outlook for using the JWST to study transit spectra of cloudy and hazy atmospheres), we first examine several fiducial atmospheres when they are clear. This section will provide useful context to help readers interpret later results by showing how information about atmospheric properties is embedded in transit spectra when clouds and hazes are absent. The parameters for four fiducial atmospheres are summarized in Table 4. The range of temperatures is chosen to hit each condensate that may form in the warm–hot exoplanets most suitable for study with transit spectroscopy (see black dashed lines in Figure 2). A metallicity on the higher end of our range is chosen so that the condensate species which include rarer elements are present in non-negligible amounts. We assume isothermal structures with temperatures of 700 K, 1000 K, 1400 K, and 1800 K, respectively. The 1000, 1400, and 1800 K planets have masses and radii chosen to represent hot Jupiters around Sun-like stars. All are assumed to have the same mass but have increasing reference radii with temperature, so the planets have different surface gravities. The 700 K planet has a mass, radius, and stellar radius chosen to approximate a warmer version of the mini-Neptune GJ1214b. Along with temperatures, the surface gravities, and chemical abundances vary between the objects.

Figure 3 shows the fiducial clear transit spectra in the left-hand column and a measure of which pressure levels are shaping the transit spectra at each wavelength in the right-hand column. This calculation is done by setting the opacity in a given pressure layer to zero and then computing the resulting transit spectrum without that layer's contribution. This is then compared to the full transit spectrum including the opacity from all layers. If a layer is contributing to the transit spectrum, then setting its opacity to zero will result in a large difference between the full spectrum and the spectrum missing one layer. We will refer to this calculation hereafter as the "transit contribution function." In the figure, lighter-colored, yellow and orange portions represent the parts of the atmosphere that are shaping the transit spectrum, while darker blue portions are pressure levels that do not contribute much to the transit spectrum. One can see that, at wavelengths where the low pressures (high altitudes) are shaping the transit spectrum, a correspondingly larger transit depth is seen in the transit spectrum on the left.

In the 0.5–1.0 μm range, all four transit spectra are probing 10^{-1}–10^{-3} bar. The 700 K case has Rayleigh scattering blueward of 0.7 μm. The 1000 and 1400 K planets have prominent sodium and potassium doublets at 0.66 and 0.77 μm. In the 1800 K atmosphere, metal hydrides like FeH, CrH, MgH, and CaH cause the additional features in the optical portion of the spectrum. All temperatures have prominent water absorption features across the 1–15 μm range, augmented by CH_4 at the edges and in between water features at 1.5, 2.25, and 3.5 μm. There is a strong CO absorption feature at 4.7 μm, and another smaller one at ∼2.3 μm. As the temperature lowers from 1800 K down to 700 K, CH_4 abundances increase and CO abundances decrease (Sharp & Burrows 2007). In the 1–2 μm range, peaks of absorption features in the transit spectra probe around 10^{-3}–10^{-4} bar, while between absorption features transit spectra probe pressures of around 10^{-2} bar. Longward of 2 μm, the peaks of absorption features probe around $10^{-4.5}$–$10^{-5.5}$ bar. The windows between absorption features reach down to only 10^{-4} bar. In the CO feature around 4.7 μm, a very high altitude/low pressure of around 10^{-6} bar is shaping the transit spectrum.

Figure 4 demonstrates how perturbing the non-aerosol parameters in our model (reference pressure, temperature, and metallicity) changes the resulting transit spectra. Each column contains transit spectra perturbing a different parameter, and each row shows a different one of the fiducial planets.

Altering the reference pressure, P_0, keeps the relative shape of the transit spectra almost the same, mostly shifting the average transit depth up or down (see the left column of Figure 4). To demonstrate the subtle change in shape that results from changing P_0, Figure 5 shows the transit depth at each wavelength divided by the average depth over all wavelengths. The shape only changes for wavelengths around 1.5 μm and shorter. This indicates that changing P_0 has a different effect on Rayleigh scattering than it does on the gaseous absorption and scattering. The effect is barely perceivable in the higher surface gravity 1000, 1400, and 1800 K planets, but for the lower surface gravity 700 K planet, there is a non-negligible change in shape.

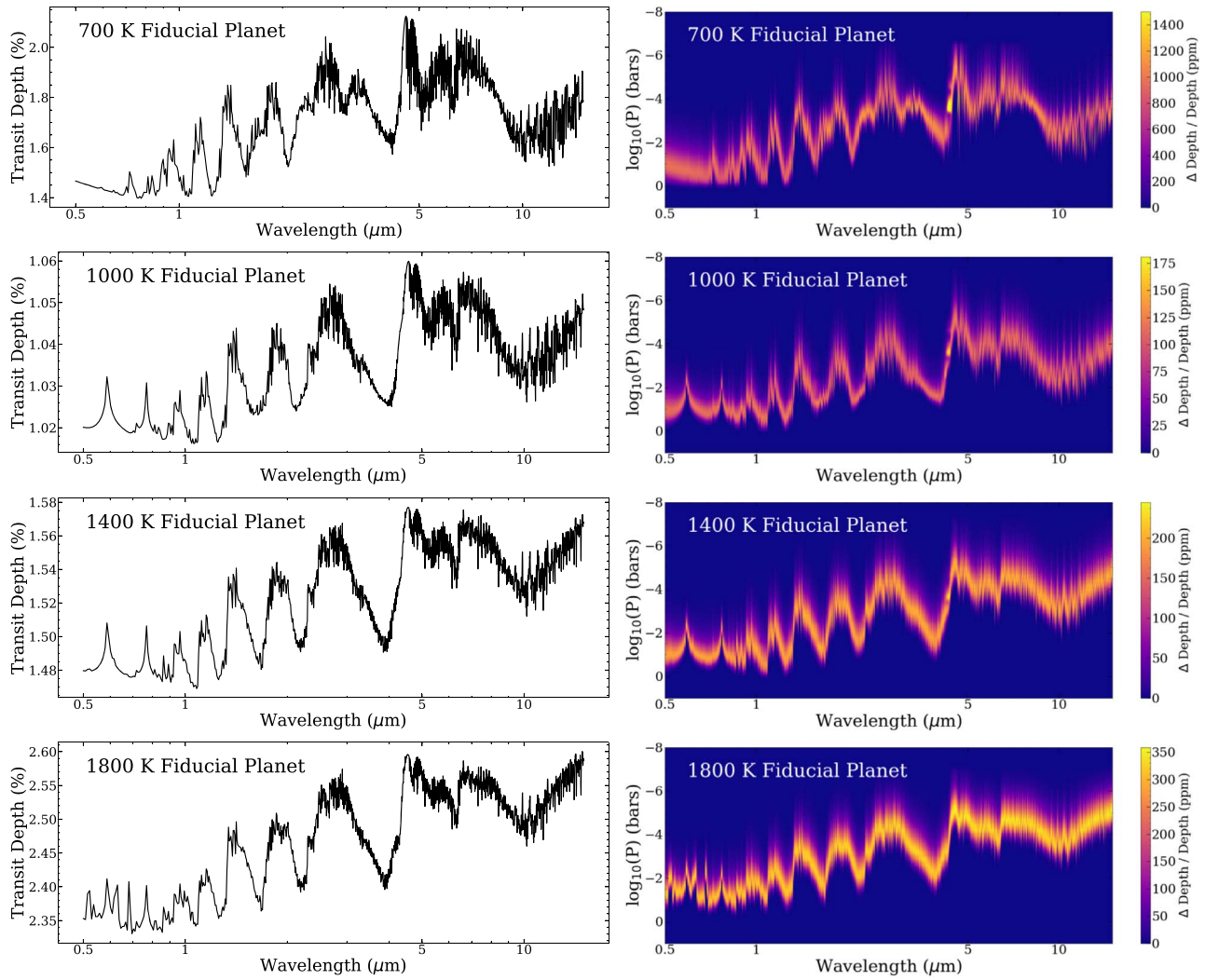

Figure 3. The left column shows transit spectra for the four fiducial atmospheres with parameters listed in Table 4. The right column shows a calculation of which pressure levels are contributing most to the transit spectrum at each wavelength. Lighter-colored, yellow and orange portions of the figure represent the parts of the atmosphere that are shaping the transit spectrum, while darker blue portions are pressure levels that do not contribute to the transit spectrum.

Changing the metallicity, Z, has a more subtle effect within the range we explore (see the center column of Figure 4). It systematically increases or decreases abundances of most opacity sources across the board, but also alters the relative thermochemical equilibrium abundances of a few important opacity sources. Finally, it can also change the scale height of the atmosphere by changing the mean molecular weight. Figure 6 isolates the change in shape as metallicity varies. This figure shows that the relative amounts of CH_4 (around 3.5 μm) and CO (around 5 μm) are changing with metallicity in the 700 and 1000 K fiducial atmospheres, and the relative strength of Rayleigh scattering versus the gaseous absorption is changing for all the fiducial atmospheres. In order to get a handle on metallicity, one must have measurements that include some of the wavelengths that do not lie directly on top of each other in this figure, and measurements at wavelengths that do. Otherwise, there is either no change with metallicity, and/or a degeneracy between changing the reference pressure and the metallicity. For all four temperatures, the relative differences between wavelengths blueward of 0.75 μm and wavelengths redward of 0.75 μm can show metallicity changes. Unfortunately, these short wavelengths are very prone to being covered by aerosols since they are reaching deeper into the atmosphere to pressures of around 10^{-2} bar. When the temperature is 700 K, as metallicity varies some longer wavelengths around 3.5, 5, and 8 μm change relative to the rest of the transit spectrum. These changes occur around pressures of 10^{-4} bar, so they are more likely to be detectable above a cloud or haze, but still in danger of being obscured by a high-altitude aerosol. When the temperature is 1000 K, the depth and breadth of water absorption features vary slightly with metallicity, and changes are apparent in the windows at 1.8, 2.25, and 4.25–4.75 μm (i.e., where CH_4 is peaking through). These wavelengths are probing around $10^{-2.5}$–10^{-3} bar. For 1400 and 1800 K, there is really not much change in shape with metallicity that is probed above a pressure of 10^{-2} bar. This hints that, if any aerosols are present at altitude, it may be difficult to make metallicity measurements of exoplanets hotter than 1000 K—or at least measurements that are precise enough to be meaningful within the metallicity range explored here. Differences between 3 and 100–1000 $\times$ $Z_\odot$ could still be discernible.

Tweaking the temperature, T, has a significant effect on both the shape and baseline depth of the transit spectra, see Figure 7 and the right-most column of Figure 4. First of all, the

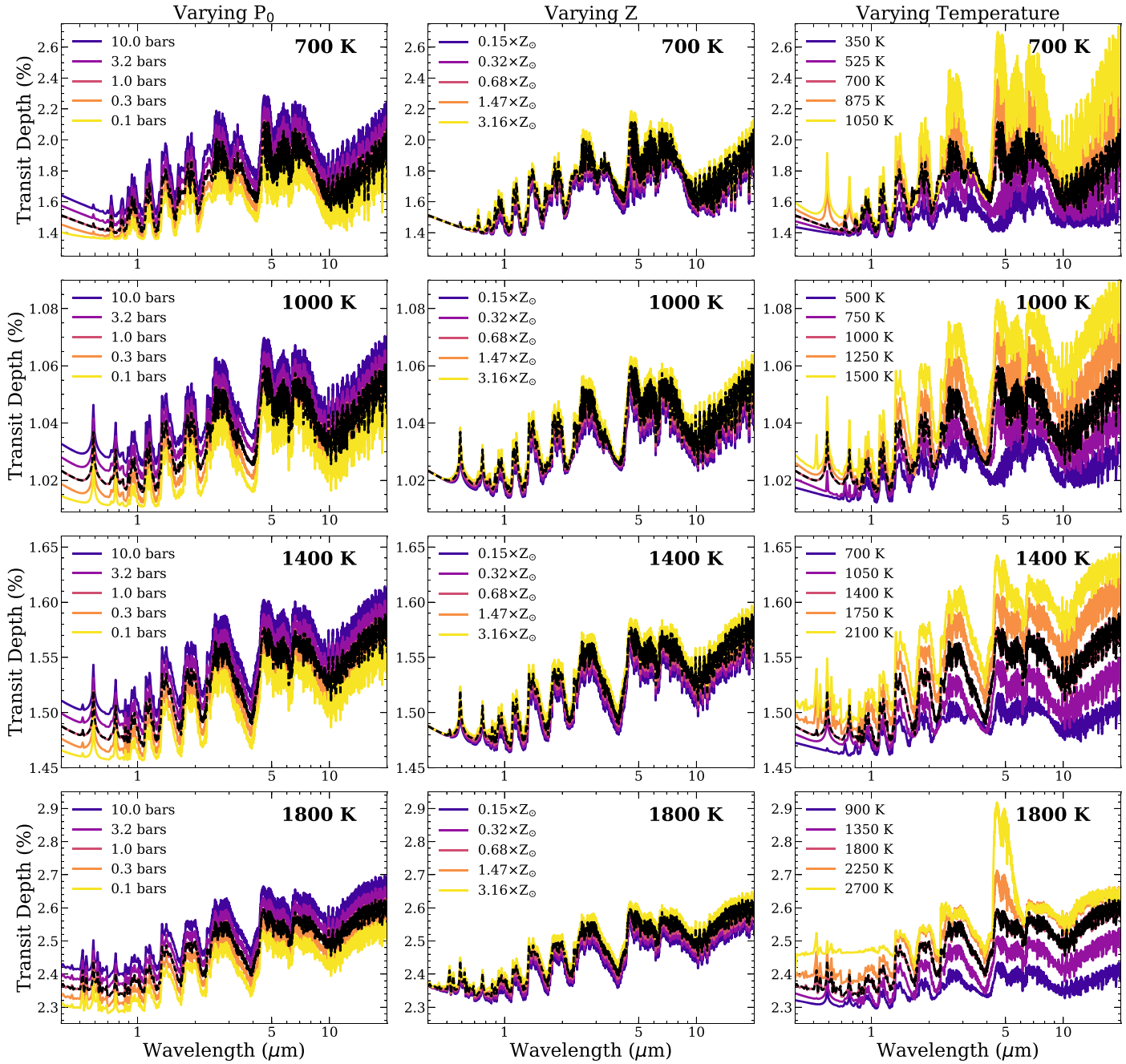

Figure 4. Demonstration of the transit spectra's sensitivity to the reference pressure P_0, the metallicity Z, and the temperature. We vary each parameter about the fiducial values for each of our four fiducial atmospheres (black dashed lines show fiducial transit spectra). See Table 4 for a summary of the fiducial atmospheres. Each column varies a different parameter and each row shows a different fiducial atmosphere. Within each row the y-axis bounds are kept the same for easier comparison.

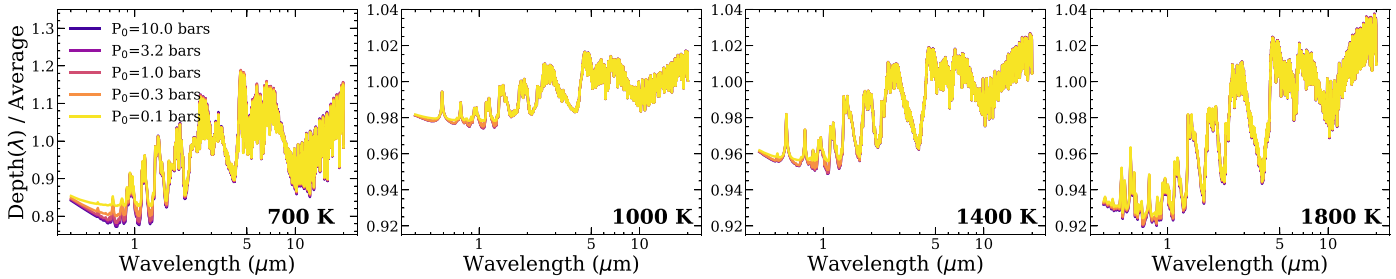

Figure 5. This figure shows the transit depth at each wavelength divided by the average transit depth as the reference pressure changes. This is meant to isolate how changing the reference pressure alters the shape of the transit spectrum, not just the baseline. Each panel shows a different fiducial temperature atmosphere. Note that there is a different y-axis scale for the 700 K atmosphere than for the 1000, 1400, and 1800 K atmospheres.

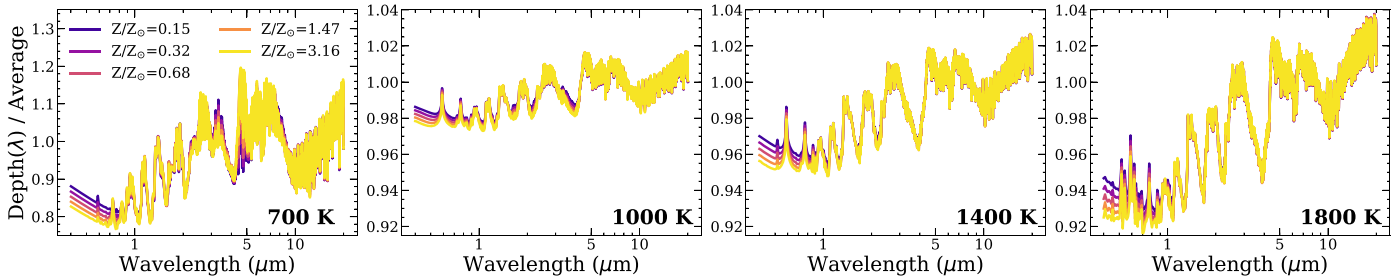

Figure 6. This figure shows the transit depth at each wavelength divided by the average transit depth as the metallicity changes. This isolates how changing the metallicity alters the shape of the transit spectrum, not just the overall opacity. Each panel shows a different fiducial temperature atmosphere. One can see that, within the small metallicity range considered, the change in mean molecular weight due to the change in metallicity is not large enough to significantly impact the pressure scale height. If this were the case, then the spectra would be stretched out and squished relative to each other across all the wavelengths. Changing metallicity mainly influences the balance of CH_4 and CO (see panels for 700 and 1000 K atmospheres around 2–5 μm) and the amount of Rayleigh scattering relative to the other gaseous absorption (see wavelengths shorter than 1 μm in all the panels).

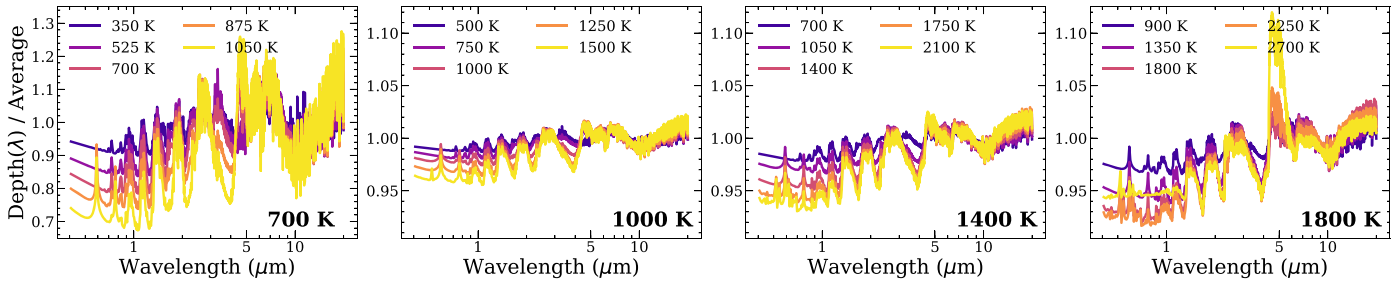

Figure 7. This figure shows the transit depth at each wavelength divided by the average transit depth as the temperature changes. This isolates how changing the temperature alters the shape of the transit spectrum from any shifts upwards or downwards that are constant for all wavelengths. Each panel shows a different fiducial atmosphere. For the 1000, 1400, and 1800 K planets, the mass is always one Jupiter mass. This means that increasing temperature leads to increased scale heights, so for the 1800 K object we see larger variation across wavelengths. The 700 K object has a much smaller mass, so it is scale height is an order-of-magnitude larger than the others even though it has a cooler temperature.

temperature sets the equilibrium chemistry, so changing the temperature alters which features are present and their relative strengths. At certain junctures, the change in temperature can dramatically change the shape: for example, between 700 and 800 K when the Na doublet becomes prominent (see the top-right panel around 0.6 μm), between 1500 and 1700 K when metal hydrides start shaping the optical (see the bottom two panels in the right-most column at wavelengths shorter than 1 μm), and above 2000 K when the CO feature at 4–5 μm grows extremely prominent. Around 2500 K, H^- opacity starts to kick in blueward of 1 μm (see yellow line in bottom right-most panel). For a full accounting of which opacity source is dominating each part of these transit spectra, we refer the reader back to Sharp & Burrows (2007) and Burrows & Sharp (1999). Changing the temperature also changes the pressure scale height, either stretching or squashing the features of the transit spectra. When looking at Figure 7, note that the 700 K planet has the smallest surface gravity, then the 1800 K planet, then the 1400 K planet, and then the 1000 K planet. We have kept the y-axis scale consistent for the 1000, 1400 and 1800 K planets.

Figures 4–7 show that changes to the temperature and the reference pressure have larger effects than changes to the metallicity within our range of $Z = 0.1$–$3.16 \times Z_\odot$. They also show that changing the reference pressure and the metallicity can have similar effects on the transit spectrum if only limited wavelength coverage or low precision measurements are available. We see the impact of these trends play out in retrievals, as one would expect. Constraints on temperature and reference pressure are generally very tight, while constraints on metallicity are a bit looser. When thick clouds or hazes overpower the gaseous opacity in the optical wavelength range, the degree of degeneracy between reference pressure and metallicity tends to increase.

4. Gas versus Aerosol Opacity from Optical to IR

Now that we have looked at the transit spectra of our fiducial atmospheres when they are clear, we will move on to explore the effects of adding in different species and sizes of aerosols. It is widely hoped that the broader wavelength coverage of the JWST will enable us to identify which aerosol species are present in exoplanet atmospheres and to access the stronger gaseous absorption features at longer wavelengths, even if clouds and hazes are diminishing the signal. Example transit spectra containing each species are shown in Figure 8 and compared to the corresponding clear transit spectrum (light gray dashed line). The spectra shown in Figure 8 assume our fiducial 1000 K hot Jupiter around a Sun-like star, a log-normal particle-size distribution with a dispersion of 2.5 and the three modal particle sizes indicated, and finally that a quarter of the available material by number of molecules went into forming the aerosols ($F = 0.25$). Particles are allowed to form as high up into the atmosphere as there is sufficient material. Since we are using the slab parameterization, there is no link between the Clausius–Clapeyron line for condensing aerosol species and the temperature–pressure profile of the atmosphere. This allows us to compare the effects of all the different aerosol species against a consistent backdrop of gaseous absorption. This type of calculation has formed the basis for the community's hopes that the JWST will provide a smoking gun revealing which

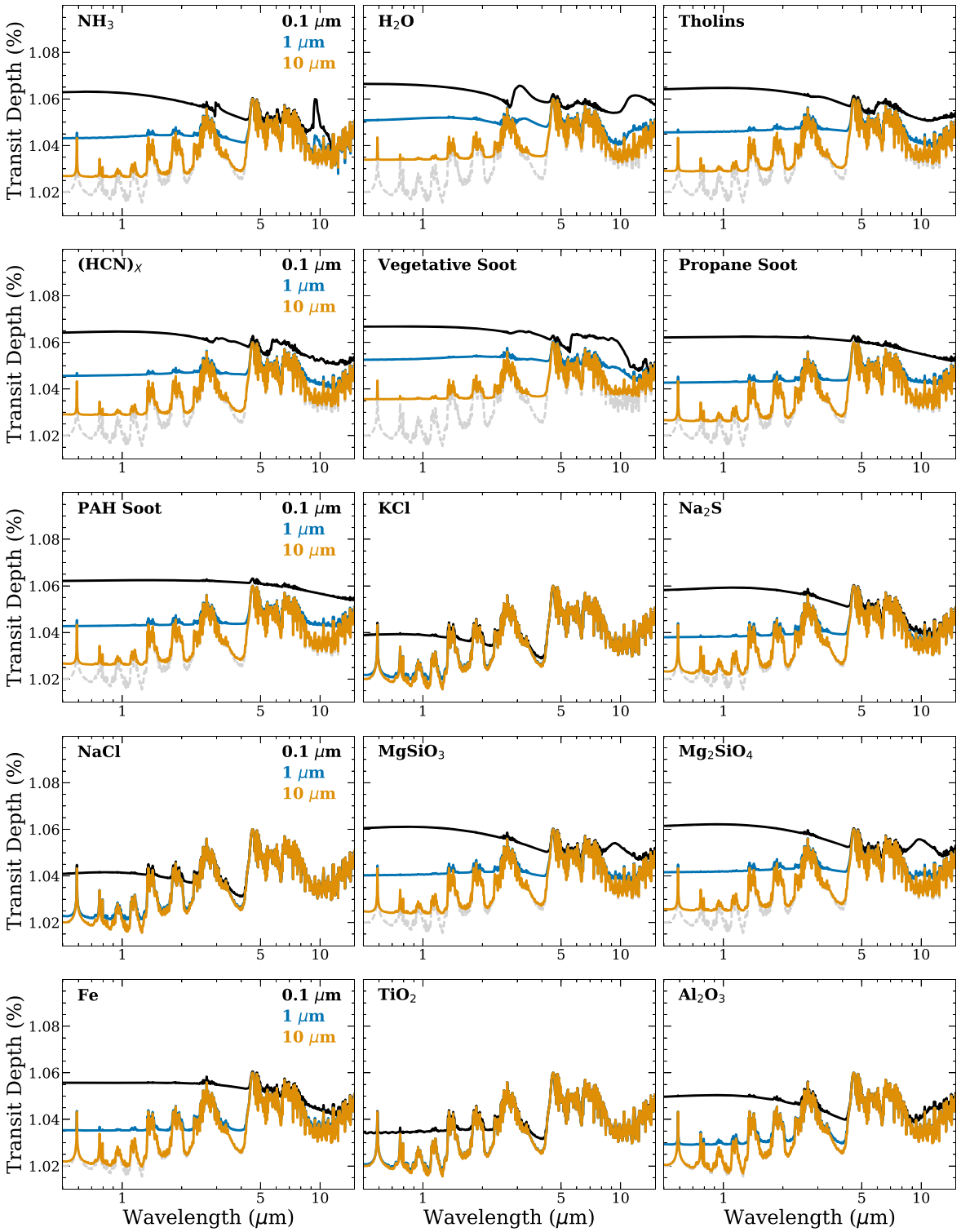

Figure 8. Transit spectra for all the aerosol species in Table 2 added to the 1000 K fiducial atmosphere as a slab aerosol with $Z = 1.05 \times Z_{\odot}$, $F = 0.25$, and $P_{\rm top}$ set to be at the top of the atmosphere. Log-normal particle-size distributions with different modal particle sizes are compared, always with a dispersion of $\sigma_a = 2.5$. Since there is a consistent value of Z and F, this means that a smaller modal particle size makes for many more aerosol particles. The gray dashed line is the clear transit spectrum for the same 1000 K fiducial atmosphere. Note that some of the condensing species would certainly not form in a 1000 K atmosphere, but we have placed them in one for the sake of comparison. Since the slab aerosol parameterization has no dependence on the T–P profile intersecting with the Clausius–Clapeyron line for a given condensate species, any species can be put in any temperature atmosphere.

aerosols are present (Wakeford & Sing 2015; Pinhas & Madhusudhan 2017; Kitzmann & Heng 2018).

Looking at Figure 8, one can see that the contributions from aerosols in the 0.4–2 μm wavelength range are generally flat or consist of a smooth monotonic slope for a variety of species and particle sizes. These are the wavelength ranges readily observed to date, so it is no wonder we have not been able to identify which species are present. Species start to look more

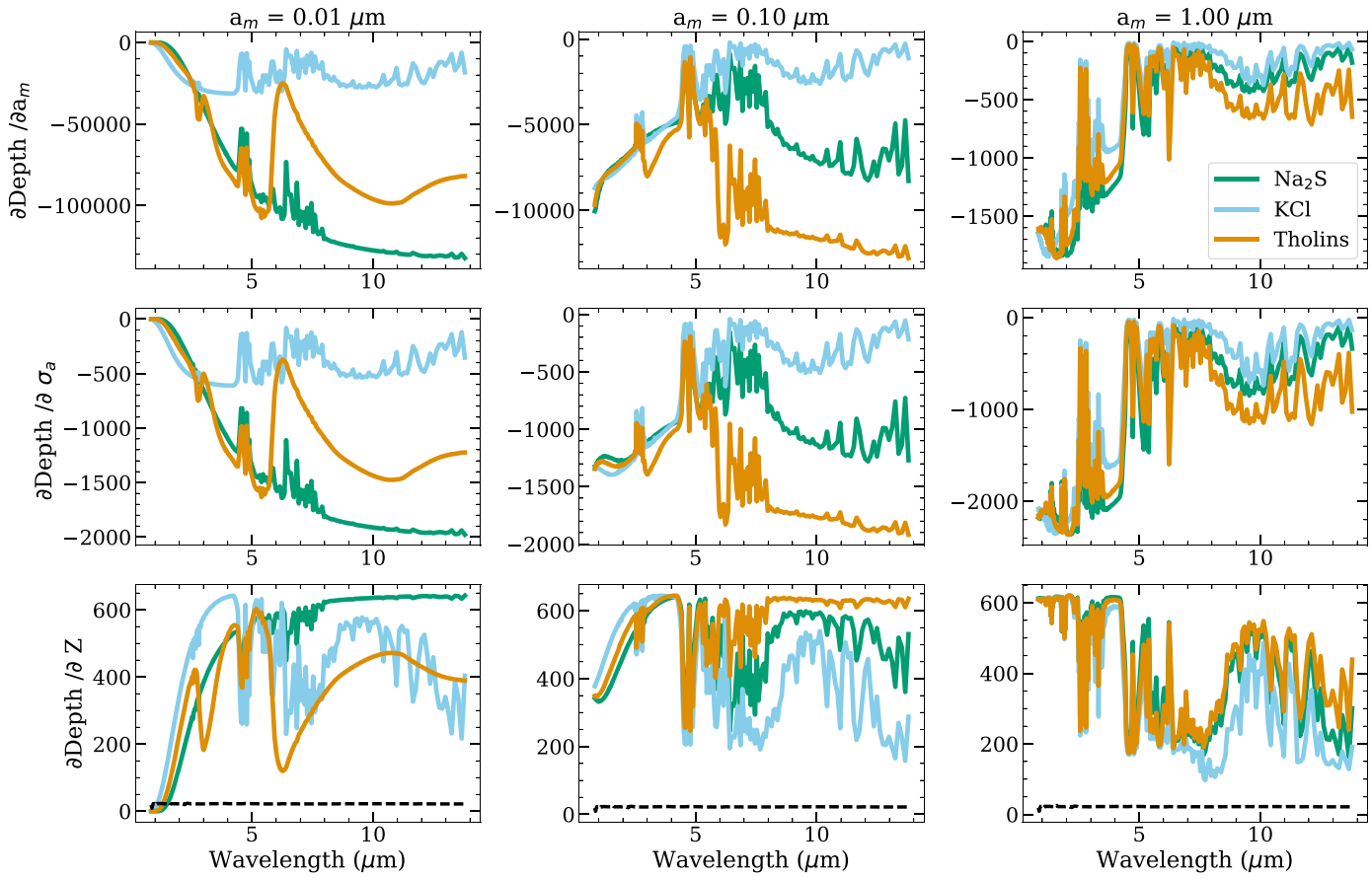

Figure 9. Transit-depth Jacobians with respect to modal particle size, size dispersion, and metallicity. These are computed for our 700 K fiducial atmosphere when Na_2S (green), KCl (light blue), and Titan tholins (orange) are included as slab aerosols. The top row is the partial derivative of the transit depth with modal particle size, the second row is the partial derivative with the size dispersion, and the bottom row is the partial derivative with metallicity. In the metallicity panels we also include a dashed black line showing the Jacobian for a clear atmosphere. Each column shows the Jacobians calculated for a different modal particle size as labeled above. The size dispersion is $\sigma_a = 2.5$ for every case. We set F for each aerosol species such that $F\times$ is the solar abundance of the limiting atomic species equal to 3×10^{-6}. This guarantees that the aerosols would not behave as a simple gray opacity source. The top-pressure cut-off for the slab aerosol was set to 10^{-8} bar, which is well above where there is no longer enough material to form many aerosol particles. When Jacobians are further from zero, it means that the transit depth for that wavelength is more steeply dependent on whichever parameter was used for the partial derivative.

distinct from 3 to 15 μm as spectral features arising from resonant bending/vibrational/rotational modes may be present (e.g., in NH_3, H_2O, Titan tholins, $(HCN)_X$, vegetative soot, $MgSiO_3$, Mg_2SiO_4, and Al_2O_3). In the absence of such distinct features, there may still be a unique, non-gray shape to the smooth aerosol opacity (e.g., for KCl, Na_2S, NaCl, or Fe). Figure 8 hints at the advantage of broad wavelength coverage for both recognizing aerosols and for measuring gaseous properties when aerosols are present. It also demonstrates a point that we will reinforce in later results: there is a tension between obtaining strong constraints on aerosol properties and obtaining strong constraints on gaseous absorption.

Whether or not aerosol spectral features are actually observable depends on the relative strengths of aerosol opacities and gaseous opacities at wavelengths where aerosol spectral features peak, as well as whether particle-size distributions are such that these features are present at all. With the assumptions made here (no top-pressure cut-off, $Z = 1.05$, and $F = 0.25$), the smaller modal particle size of 0.1 μm forms many more aerosol particles and typically overpowers gaseous absorption at most wavelengths (black lines). These type of spectra, dominated by aerosol opacity across most wavelengths, would make it easy to identify which aerosol species is present and what the particle-size distribution is, but will not provide much of the information about the gaseous absorption. At the opposite end, the 10 μm modal particle distribution formed from the same available mass of material makes many less aerosol particles, and we see that aerosols fill in the deepest troughs in gaseous absorption features, but do not overwhelm the gaseous absorption peaks (orange lines). In these examples, the spectra will not provide much information about the aerosol species or properties, but you could expect to get strong constraints on things like temperature, reference pressure, and metallicity. The spectra with a 1 μm modal particle size fall in between (blue lines). Aerosols tend to overpower gaseous opacities at shorter wavelengths, where water absorption is weaker, but not at longer wavelengths. The windows between water features at 4 and 10 μm provide the best chance of detecting aerosol features directly. For some species, the 1 μm spectra look like they could provide a smoking-gun signature of which aerosol species is present, while also allowing constraints on the gas-phase abundances (for example, see the blue lines in the panels for NH_3, H_2O, and Mg_2SiO_4).

As we have seen from the spectra in Figure 8, and might have expected intuitively, more wavelength coverage provides more information. However, one might ask: are some of these wavelengths more information dense than others? One way to

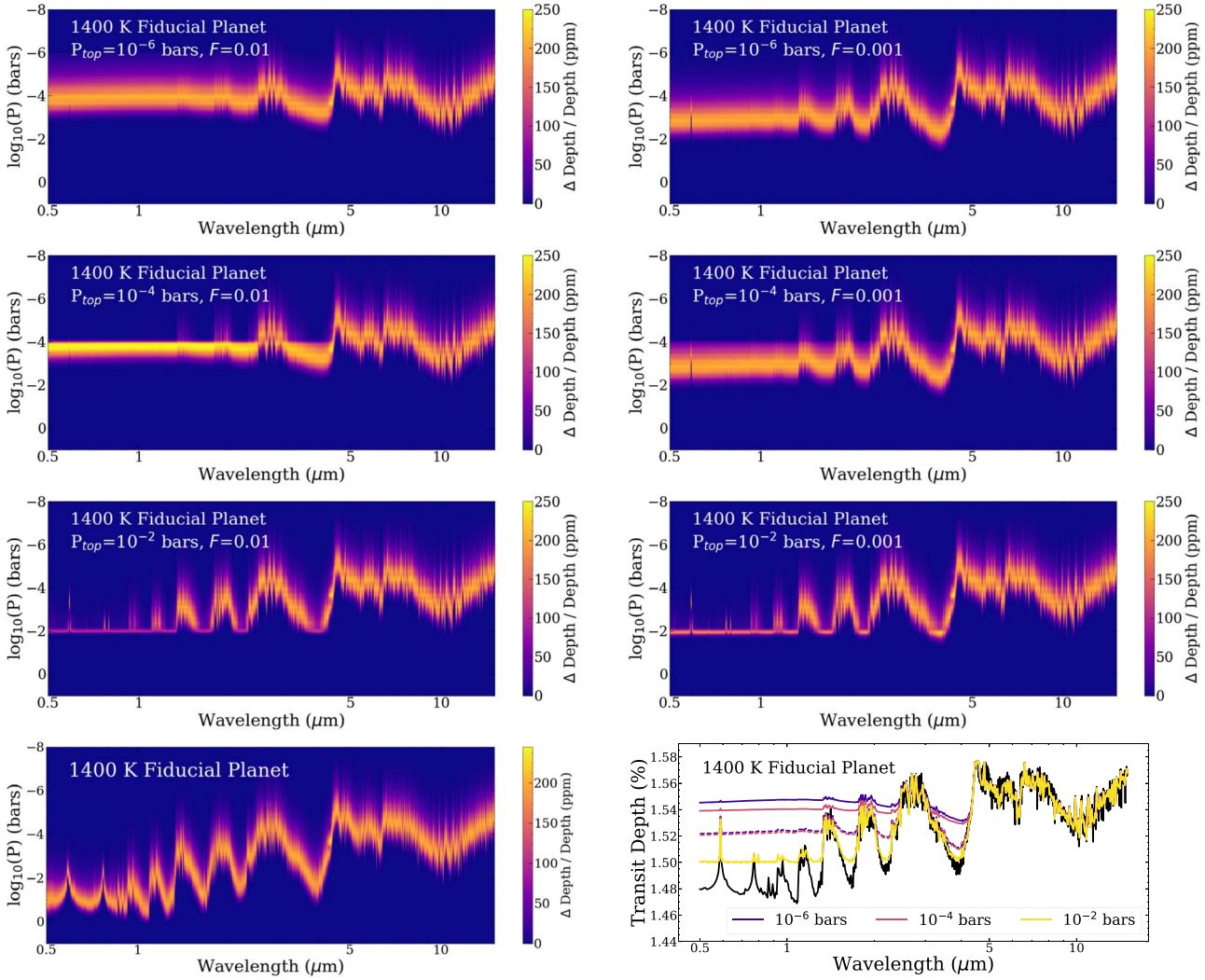

Figure 10. The top three rows show contribution functions for our 1400 K fiducial atmosphere with a tholin slab aerosol with different top-pressure cut-offs. The left column has $F = 0.01$ and the right column has $F = 0.001$. All panels have $Z = 1 \times Z_{\odot}$, $a_m = 0.1$, and $\sigma_a = 3$. The bottom-left panel repeats the clear contribution function for comparison. Lighter yellow and orange colors indicate which pressures are shaping the transit spectrum at a given wavelength. Darker purple and blue regions indicate pressures that do not shape transit spectra at a given wavelength. The lower pressures (higher altitudes) are purple because they are too low in density/opacity to block much light. The higher pressures (lower altitudes, deeper in the atmosphere) are purple because the atmosphere becomes optically thick to that wavelength at lower pressures. The bottom-right panel shows the corresponding transit spectra for these cases. Solid lines show the higher $F = 0.01$ case and dashed lines show the lower $F = 0.001$. Note that for 10^{-2} bar the dashed and solid yellow lines lie essentially on top of each other. This figure illustrates how a steep top-pressure cut-off results in gray behavior while a gradual drop in the amount of aerosol can result in distinctive spectral signatures (compare the yellow lines to the solid purple line for example). It also shows how changing the amount of material bound up into aerosol particles through F also dictates how high up in the atmosphere a significant number of particles can form (compare the dashed pink and purple lines to the solid pink and purple lines).

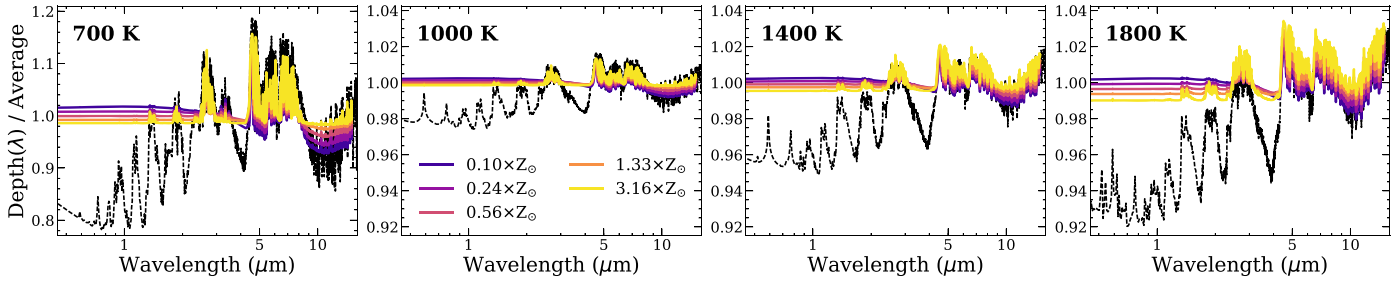

Figure 11. We show the transit depth for each wavelength divided by the average transit depth over all wavelengths as we vary metallicity, now including a Titan tholin slab aerosol like the one in Figure 10. Each panel shows a different one of our four fiducial atmospheres. The dashed black line shows the same type of plot for a $Z = 1 \times Z_{\odot}$ clear atmosphere.

assess this is to compare the Jacobians of our models for transit depth across wavelengths. We computed the partial derivatives of transit depth with modal particle size, log-normal size dispersion, and metallicity for transit spectra with a variety of particle sizes and aerosol species (Figure 9 here and Figures 21–23 in the Appendix). The aerosols are roughly

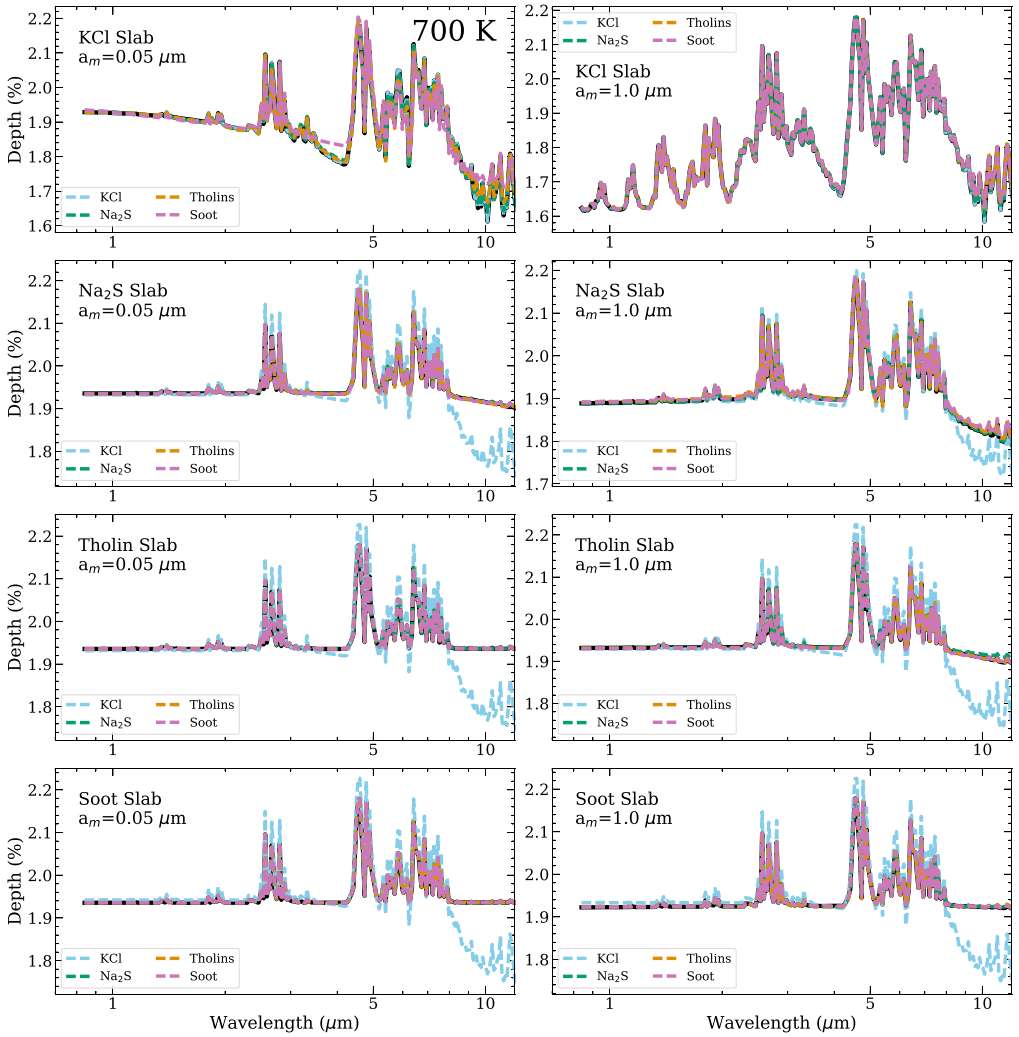

Figure 12. Transit spectra from MCMC experiments for the 700 K aerosol grouping with a slab aerosol. Each row has a different true aerosol in the simulated data, shown as the solid black line. For the 700 K fiducial atmosphere the errors for 10 stacked JWST transits are negligible compared to the transit signal, so the shaded gray error envelope is not discernible. In the left column a modal particle size of 0.05 μm was used for the simulated data. In the right column a modal particle size of 1.0 μm was used for the simulated data. Otherwise, F was kept at 1, $P_{\rm top}$ at $10^{-4.5}$ bar, and σ_a at 2.5 when generating all the simulated data. Colored dashed lines show the transit spectra corresponding to the *median* parameters of the MCMC chains run assuming different aerosol species. In many panels all of the species besides KCl fit the data very well, so curves lie right on top of each other. Table 5 shows the BIC values corresponding to each of the fits included here. Looking at the BIC values, one can see that for the 0.05 μm modal particle size, tholins and soot are virtually indistinguishable. For the 1 μm modal particle size, the true species is always preferred in a BIC comparison.

grouped by the temperatures at which they may condense, with species meant to represent hydrocarbon hazes added in where there are fewer than three candidate condensate species. If the *absolute value* of the Jacobian is large, then it indicates that the measurement at that wavelength is sensitive to the parameter in question.

Figure 9 shows Na_2S, KCl, and Titan tholins, some aerosol species that may be present in a 700 K atmosphere. Figure 21 in the Appendix shows Na_2S, NaCl, and Titan tholins, some species that may be present in a 1000 K atmosphere. Figure 22 in the Appendix shows Mg_2SiO_4, $MgSiO_3$, and Fe, some species that may be present in a 1400 K atmosphere. Figure 23 in the Appendix shows Fe, Al_2O_3, and TiO_2, some species that may be present in a 1800 K atmosphere. For the top and middle row of each figure, the partial derivatives are negative, so the lower, more negative values, represent more information/sensitivity to particle size and the spread in the size distribution, respectively. For the bottom row, the partial derivatives are positive, so higher more positive values represent more information/sensitivity to the metallicity. In computing these Jacobians, we have used the four fiducial atmospheres of Table 4, log-normal size distributions with a dispersion of 2.5, and the modal sizes listed at the top of each column and assumed the slab-type aerosol with a very high top pressure. In Figure 8 we used the same value of F for all the species, but in the Jacobian calculations we chose a different F for each aerosol species such that $F \times$ the solar abundances of the limiting species is roughly 3×10^{-6}, so for things like Al_2O3, TiO_2, KCl, and NaCl F is around 1, for Fe, silicates, and Na_2S F is order 0.1, and for H_2O, NH_3, and hydrocarbons like tholins F is order 0.01. We chose this approach so that the wavelength dependence of the aerosol optical properties would be highlighted over the differing baseline abundances of the limiting atomic species. In some Jacobians, the jagged patterns of gaseous absorption are still clearly visible (for example, see the wavelengths longer than $\sim$4 μm for Na_2S and KCl marked by green and blue lines in the far-right column of 9), while in others the Jacobians look smoother indicating that aerosol

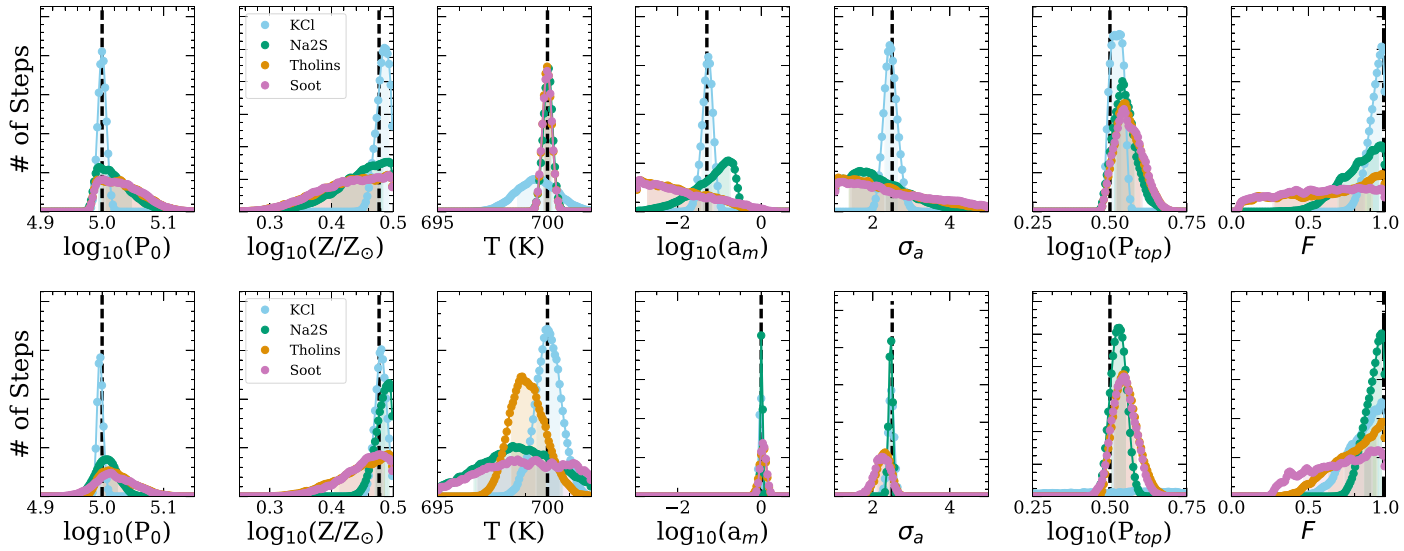

Figure 13. Posteriors for model parameters when the correct aerosol species is used in the fit. The top row shows results when the log-normal particle-size distribution had a mode of 0.05 μm, while the bottom row had a modal particle size of 1 μm. Each color corresponds to results for a different species. Shading indicates the region of the posterior which falls between the 16th and 84th percentile. Vertical dashed lines mark the true value of each parameter. Units for P_0 and $P_{\rm top}$ are in Pascals. Table 3 summarizes the priors used for MCMC chains and the meaning of all the parameters. Note that, in many panels, the soot posterior is lying almost exactly over the tholin posterior.

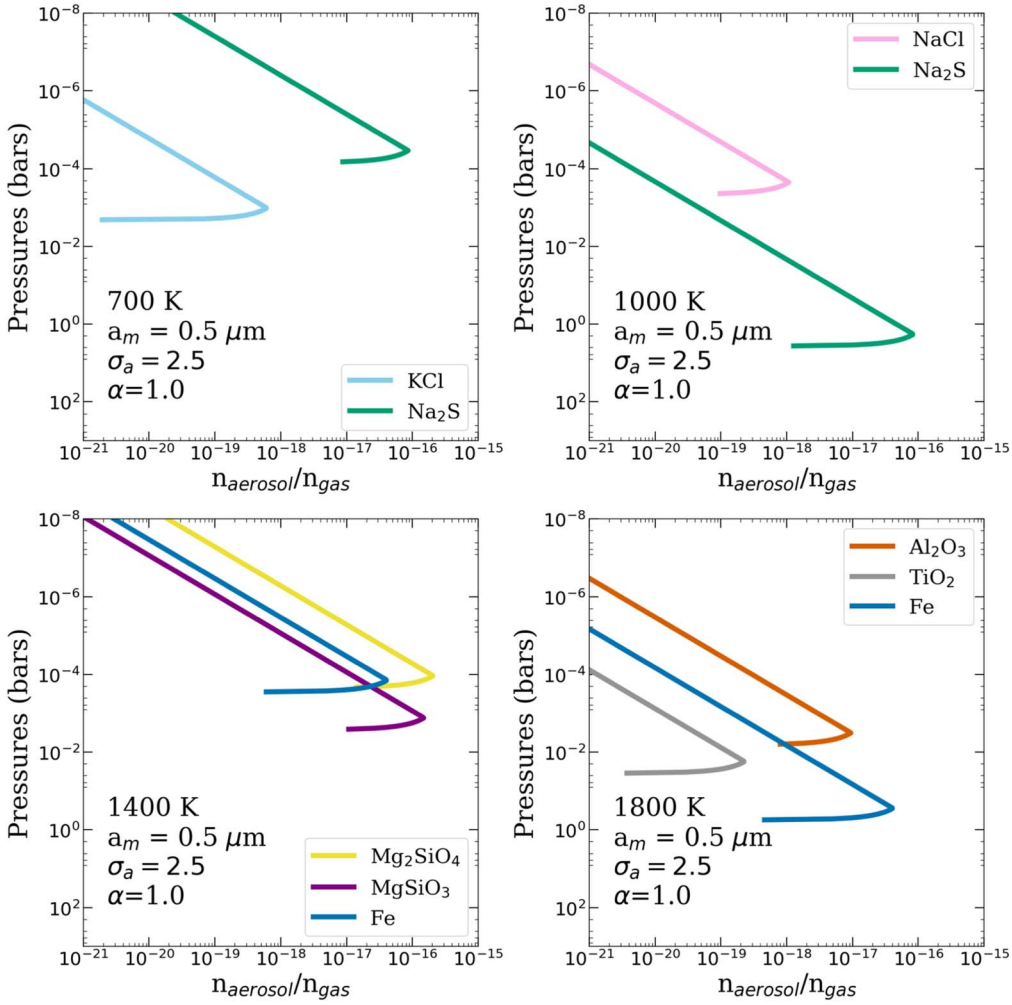

Figure 14. The profiles of the ratio of aerosol particle number density ($n_{\rm aerosol}$) over gas number density ($n_{\rm gas}$) for species that might condense at 700, 1000, 1400, and 1800 K. Note that one aerosol *particle* is made up of many aerosol *molecules*. The base of the cloud is assumed to occur where the *T*–*P* profile intersects with the Clausius–Clapeyron line for each respective species. These profiles assume a log-normal particle-size distribution with a modal size of 0.5 μm and a dispersion of 2.5, that $\alpha = 1$, and that the atmosphere has a metallicity of $Z = 1 \times Z_{\odot}$.

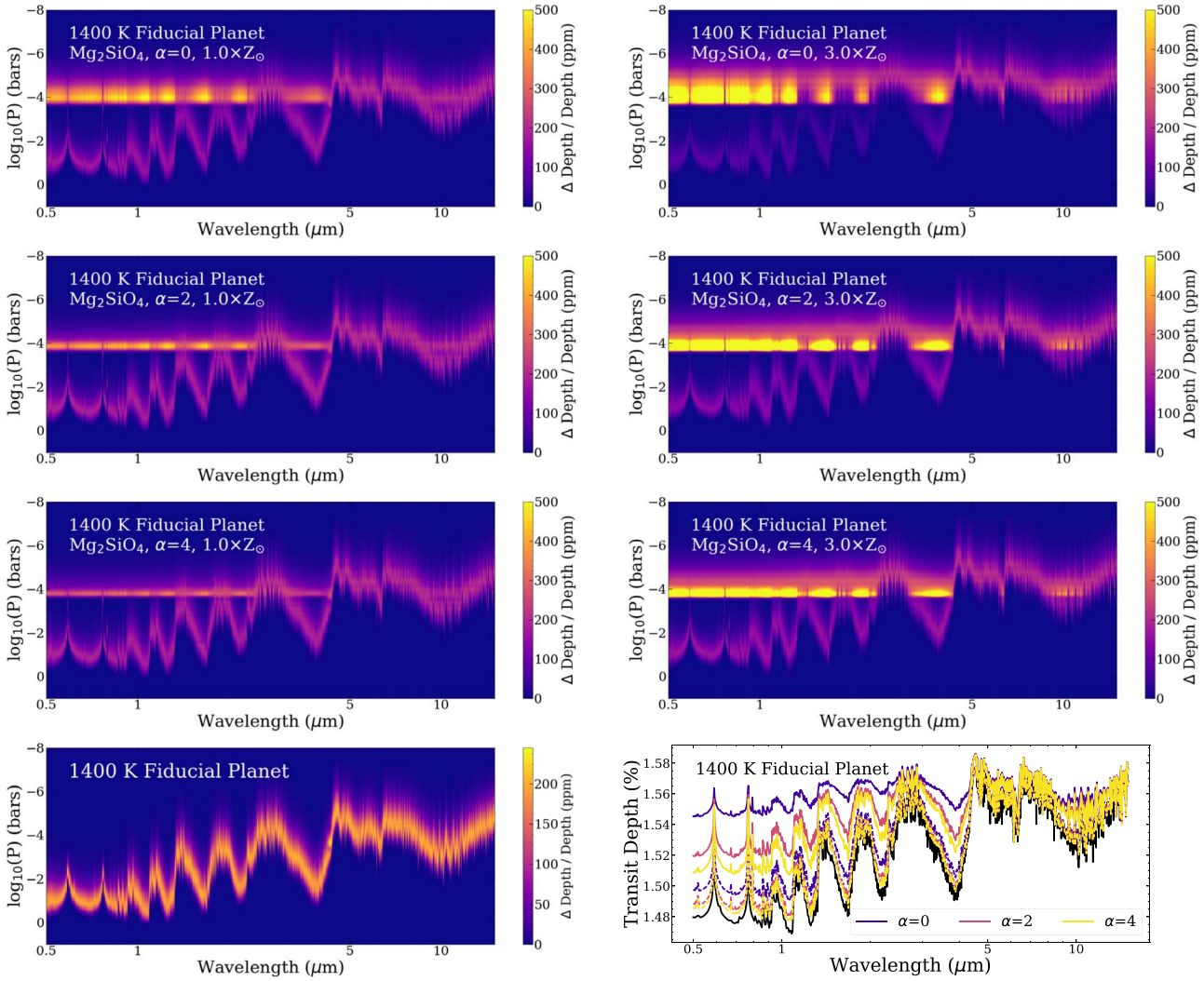

Figure 15. Transit contribution functions for the 1400 K fiducial planet with a phase equilibrium forsterite cloud for varying metallicities and α. In all cases the log-normal particle-size distribution has a modal particle size of 1 μm and a size dispersion of $\sigma_a = 3$. In the left column, the atmospheres have a metallicity of $Z = 1 \times Z_\odot$ and, in the right column, the atmosphere $Z = 3 \times Z_\odot$. In the top row $\alpha = 0$, in the second row $\alpha = 2$, in the third row $\alpha = 4$, and in the bottom-left panel we show the transit contribution function for a clear atmosphere. In the bottom-right panel we show the transit spectra that correspond to the transit contribution functions. Solid lines indicate transit spectra for the higher metallicity atmospheres and dashed lines indicate the transit spectra for lower metallicity atmospheres.

opacity is totally dominating (for example, see the orange line for tholins in the panels in the left-most column of 9). Where gaseous absorption patterns are imprinted in the Jacobians, one sees local minima of sensitivity to aerosol properties and to metallicity (for example, see the 4–8 μm region in most of the curves in 9). There is a lot wrapped into these figures, so we break the implications into four main themes:

1. Some wavelengths tend to be dominated by aerosol opacity while others tend to be dominated by gaseous opacity. For 0.1 and 1.0 μm modal particle sizes, the shortest wavelengths (under 2 μm) and the longer wavelengths (over 8 μm) tend to be most sensitive to particle size and the breadth of the particle-size distribution for a variety of species (though Fe in the 1800 K atmosphere, NaCl and KCl do not show as strong of an aerosol sensitivity at the longer wavelengths). In the 4–8 μm range, the Jacobians for modal particle size and size dispersion tend to show less sensitivity, indicating that these wavelengths are still dominated by gaseous opacity, even when aerosols are present. In particular, the profile of the CO feature at 4.5 μm is always apparent as a local minimum in sensitivity to modal particle size and breadth of the particle-size distribution. We attribute this trend to two things. First, the gaseous absorption is strong at these wavelengths. We saw in the previous section that the transit spectrum at these wavelengths is formed at low pressures of 10^{-6} bar for clear atmospheres (see Figure 3). Second, many aerosol species have a drop in their extinction efficiencies around this wavelength range, at least for small particles (see Figure 20). For a 0.01 μm modal particle size, the shortest wavelengths are less sensitive to modal particle size and the dispersion of the particle-size distribution compared to the 0.1 μm and 1.0 μm cases.
2. A result of item 1 is that the gaseous CO and water absorption from ~4 to 8 μm may remain detectable even if the optical and NIR portion of a transit spectrum is flattened or smoothed by significant aerosol extinction. Targets for which no gaseous absorption features are currently detected may prove more forthcoming with the JWST. The likelihood of finding gaseous absorption at

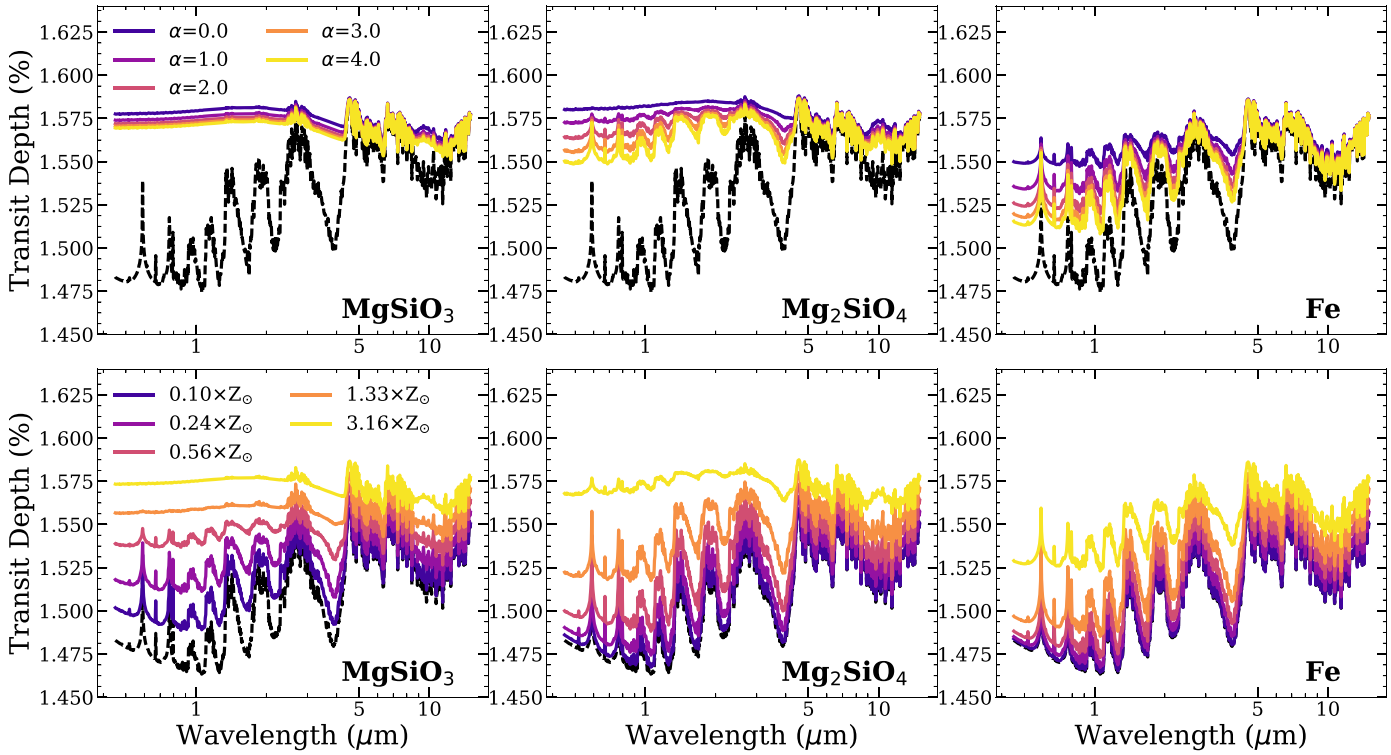

Figure 16. A demonstration of the 1400 K planet's sensitivity to metallicity and α when an equilibrium cloud of $MgSiO_3$ (left column), Mg_2SiO_4 (center column), or Fe (right column) is present. The top row shows transit spectra with varying α and the bottom row shows transit spectra with varying Z. In all cases we assume $a_m = 0.5$ μm and $\sigma_a = 2.5$. When we are varying α, Z is fixed at $3 \times Z_\odot$, and when we are varying Z, we fix α at 2. In each panel a black dashed line shows the transit spectrum for the clear 1400 K atmosphere.

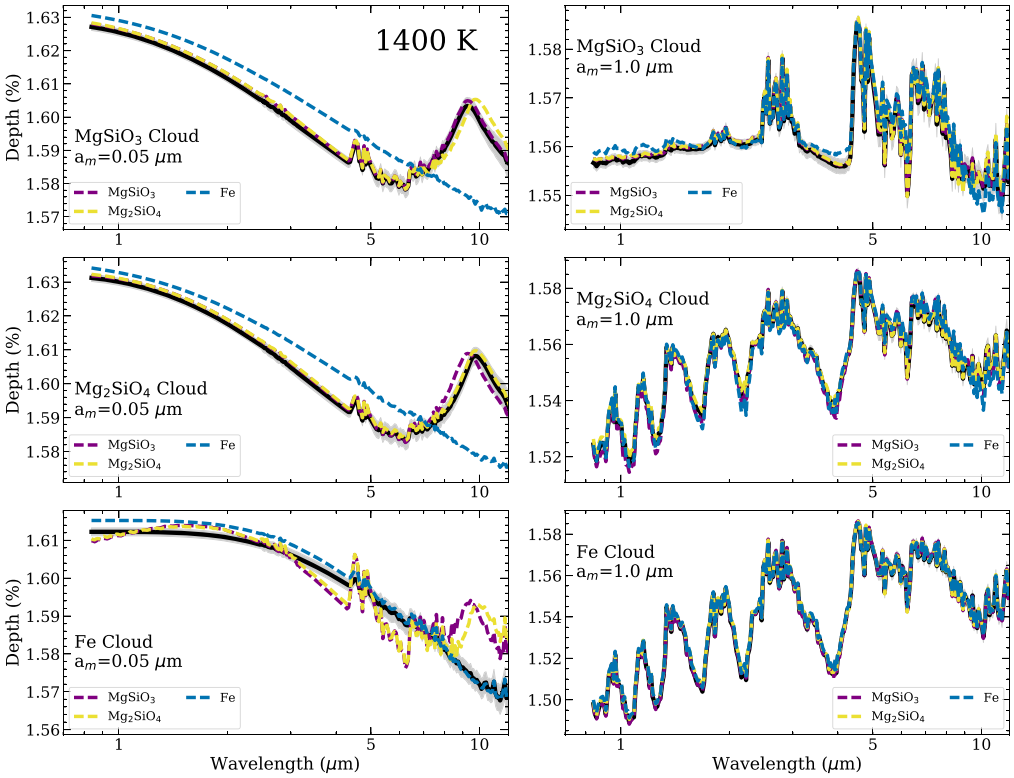

Figure 17. Results for MCMC experiments with the 1400 K atmosphere and phase equilibrium clouds. The solid black lines with shaded gray error envelopes indicate the simulated data. Dashed lines show the spectra corresponding to *median* parameters from the MCMC chains. Different colors show the results for fits with $MgSiO_3$ clouds, Mg_2SiO_4 clouds, and Fe clouds. In the top row the true cloud species is $MgSiO_3$, in the middle row it is Mg_2SiO_4, and in the bottom row it is Fe. On the left-hand side the modal particle size is 0.05 μm and on the right side the modal particle size is 1 μm. α is always 2 and σ_a is 2.5. Other parameter values can be found in Table 4. The top two sections of Table 7 summarize the BIC values for all of these MCMC fits.

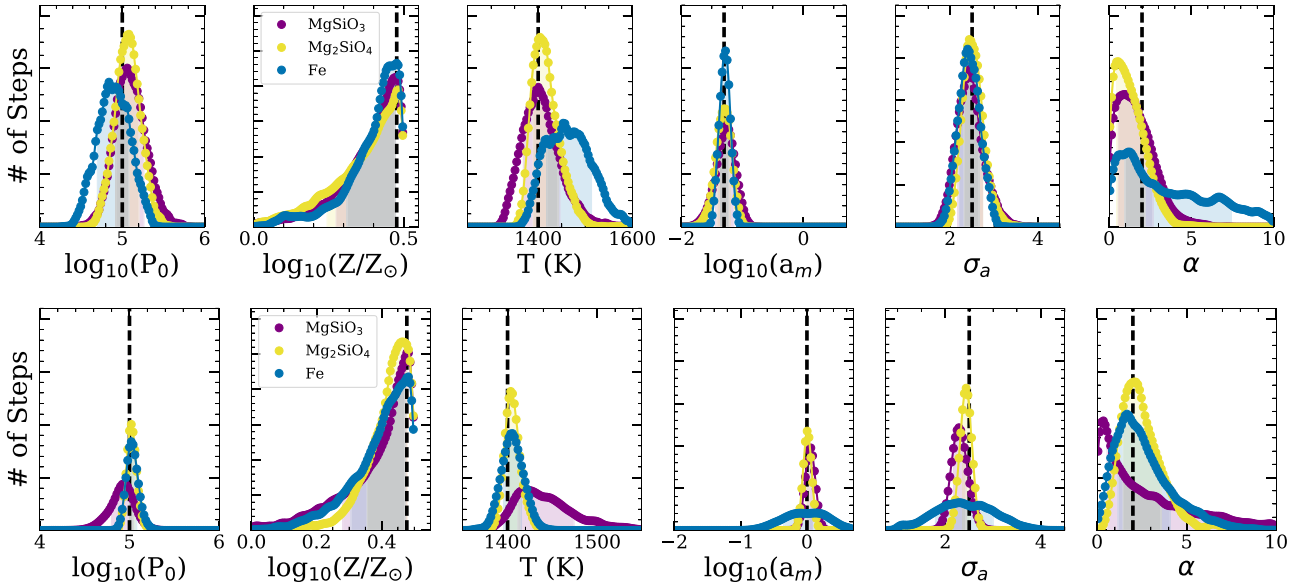

Figure 18. Posteriors for all parameters when the correct cloud species is used to fit data simulated with the phase equilibrium cloud model in the 1400 K fiducial atmosphere. The top row used data simulated with a modal cloud particle size of 0.05 μm, and the bottom row was simulated with a larger modal cloud particle size of 1.0 μm. Each color represents a different condensate species. Vertical lines indicate the true values of parameters, and shaded regions mark the parts of the posterior that fall between the 16th and 84th percentile. This would represent the one-sigma uncertainties if the posteriors were Gaussian.

longer wavelengths for planets which appear featureless with current data will, of course, depend on which species of aerosol is present, what quantity of aerosol is present, and how high up into the atmosphere it extends. In our parameterization, a large value of F and Z and smaller particle sizes tend to result in transit spectra where aerosol opacity completely overwhelms gaseous absorption at all wavelengths. We have also only considered metallicities ranging from slightly sub-solar to roughly the metallicity of Jupiter. Planets with much higher metallicities shrink gaseous absorption features and provide more material for aerosol production. Nonetheless, the spectra shown in Figure 8 and the trends in the Jacobian figures demonstrate that one can construct feasible aerosol scenarios which smooth the optical and NIR portions of transit spectra while still revealing gaseous absorption features from ~4 to 8 μm.

3. The newly available continuous long-wavelength coverage of the JWST incorporates wavelengths where different aerosol species look most distinct. The Jacobians for different species are more similar to each other at optical wavelengths than the infrared wavelengths for modal particle sizes of 0.1 and 1 μm (look particularly at Figures 21–23 rather than Figure 9). The exceptions are 0.1 μm Iron which has enhanced sensitivity in the optical, and $MgSiO_3$ and Mg_2SiO_4 which tend to have very similar Jacobians across all wavelengths not just in the optical. They only have significant differences in their Jacobians when the resonance feature around 10 μm is visible (see column for modal particle size 0.01 μm in Figure 22).
4. These Jacobian calculations reinforce the idea that there is a tension between learning about aerosol properties and learning about gaseous atmospheric properties, but also indicate a possible sweet spot where we can have our cake and eat it too. For the 700, 1400, and 1800 K fiducial atmospheres, transit spectra with aerosols included are much more sensitive to metallicity than transit spectra for clear atmospheres (shown as a gray line in the panels in the bottom row of each figure). For the 1.0 μm case, the Jacobians for modal particle size are small and the gaseous absorption peaks are almost all apparent. For the 0.01 μm case, the Jacobians for modal particle size are largest by an order of magnitude and, at many wavelengths, no gaseous absorptions effects are discernible at all. Our scaled F was chosen such that a size distribution with mode 0.75 would show some gas absorption, but also non-gray aerosol effects. This means that there is plenty of aerosol material for the 0.01 μm modal size to overpower gaseous opacities, and that the 1 μm modal size tends to just fill in the windows between absorption features in a slightly non-gray manner.

These example transit spectra and Jacobian calculations lend further credence the community's hope that the extensive wavelength coverage and high precision of the JWST and ARIEL may enable clearer measurements of both the gas phase and the properties of any aerosols present in exoplanet atmospheres. Different wavelengths of light probe different pressure layers in the atmosphere as they encounter a different combination of aerosol opacity and gaseous opacity. Smooth spectra in the sparse optical–NIR range currently available do not obviate the possibility of information-filled NIR–midIR JWST transit spectra. In the remainder of the paper, we will see how these results bear out in MCMC retrievals with slab hazes and clouds and phase equilibrium clouds, and how the picture changes as we alter the spatial positions of particles in a wider variety of ways than shown in this section. We emphasize again, that ultimately these conclusions will depend on the ground truth of the conditions in the atmospheres of transit spectroscopy targets.

5. Slab-type Hazes and Clouds

In this section, we will demonstrate the range of behavior that can be produced by the slab aerosol, and then we will test

how well aerosol species and properties can be retrieved (along with other atmospheric parameters). The slab aerosol is a useful model to consider because it does not make strong assumptions about where in the atmosphere photochemical hazes and condensate clouds will form. Its only assumptions are that the same aerosol size distribution is present at all pressures which contain aerosol, and that the base of the haze or cloud will extend down to pressures too high to be probed by transit spectroscopy.

There are three regimes of transit spectra that can arise when a slab haze or cloud is included in an atmosphere. First, one can get transit spectra with a completely gradual cloud top exhibiting variation in aerosol extinction with wavelength (like we saw in the previous section). Second, one can have an aerosol that manifests as a purely gray opacity added onto the gaseous absorption. Finally, one can get transit spectra which exhibit the non-gray behavior described in regime 1 at some wavelengths (where the aerosols have a smaller total cross section), but which are also flattened by a top-pressure cut-off at other wavelengths (where the aerosols have a larger total cross section).

In the first regime, the top-pressure cut-off had no effect on the transit spectrum because it is at such a high pressure that the cloud or haze is optically thin to all wavelengths of light by the time it is reached. This enables the full variation of the aerosol's wavelength-dependent opacity to be imprinted on the transit spectrum. Alternatively to setting a very high $P_{\rm top}$, one could achieve this behavior by setting F and Z to be very low, or by specifying a larger modal particle size such that less total particles form. If the aerosol opacity is stronger than the gaseous absorption across a range of wavelengths, then this will produce a transit spectrum with lots of information about species and particle-size distributions. An atmosphere can fall into the second regime if there is a steep top-pressure cut-off at an altitude where the haze or aerosol is optically thick across all wavelengths. It might also result if the aerosol is so optically thin that it just barely fills in troughs in between absorption peaks. If the particle-size distribution is simply very broad or has a large modal particle size, then one will also see only gray effects on the transit spectrum, because large particles do not have as much variation in extinction efficiency with wavelength (see orange lines in Figure 20). A gray aerosol can sometimes put a strong constraint on $P_{\rm top}$, but will likely place only an upper limit on F. There can be strong degeneracies between modal particle size, F, and Z depending on which species is included and what $P_{\rm top}$ is. Transit spectra in the third regime can enable one to constrain $P_{\rm top}$, particle-size distributions, and perhaps F and Z, though this will depend on whether the aerosol is obscuring the gaseous signatures of metallicity or not. This third regime is thus the one most suitable for fitting with our full slab-aerosol model. The first regime would be better to leave out $P_{\rm top}$, and the second regime would be better fit by only $P_{\rm top}$ and no additional aerosol-related parameters.

The particle-size distribution, F, $P_{\rm top}$, Z, and the species of aerosol dictate which of these three regimes manifests in the transit spectrum. The total available material to incorporate into aerosols depends on which species of aerosol is forming and the metallicity of the atmosphere. This means that the same combination of F, $P_{\rm top}$, and particle size can fall into a different regime depending on which species and metallicity have been specified. Examples of this interplay are shown in Figure 10. Each panel in Figure 10 shows the transit contribution function for the 1000 K fiducial planet with a tholin haze added with modal particle size 0.1 μm and $\sigma_a = 3$. The first three rows have a different top-pressure cut-off. The left column has $F = 0.01$ and the right column has $F = 0.001$. The bottom-left panel shows the contribution function of the clear atmosphere, for comparison. The transit spectra corresponding to each of the contribution functions are shown in the bottom right. Dashed lines are for spectra with $F = 0.001$, and solid lines are for spectra with $F = 0.01$.

The transit spectra corresponding to the top-left panel, the top-right panel, and the right panel in the second row fall into regime 1, in which there is a gradual top to the haze, allowing the full range of tholin spectral signatures to show up in the transit spectrum (see purple solid line, the purple dashed line, and the pink dashed line in the bottom right panel). Both panels in the third row, with top pressures of 10^{-2} bar, contain a gray aerosol. These correspond to the transit spectra shown with yellow lines in the bottom right panel. The left panel in the second row falls into regime 3, and its transit spectrum is shown by the pink solid line in the bottom-right panel. In this case, the wavelengths shorter than $\sim$4 μm are gray, evidence for the steep top-pressure cut-off at 10^{-4} bar, but the wavelengths from 4 to 5μm have a non-gray aerosol signature encoding information about the particle-size distribution. One can see how varying F and $P_{\rm top}$ shifts the transit spectrum about between regimes 1–3, even for a fixed metallicity, species of aerosol, and particle-size distribution.

What if we change the metallicity? We saw the effect of changing metallicity on a clear atmosphere in Section 3 where we learned that, to measure Z well, we must compare wavelengths where Rayleigh scattering, CH_4, or CO absorption dominate to wavelengths where H_2O absorption dominates.

If metallicity changes in an atmosphere with a slab aerosol, the values of F and $P_{\rm top}$ which set the bounds between regime 1–3 will also change. Changing the metallicity of a cloudy or hazy atmosphere changes the total amount of available material to incorporate into aerosols; so, for a given F, increasing Z means more aerosols are present. Figure 11 shows the transit depth at each wavelength divided by the average transit depth as we change the metallicity in a hazy version of our four fiducial atmospheres. F is kept at 0.005, $P_{\rm top}$ is kept at 10^{-4} bar, a_m is kept at 0.1 μm, and σ_a is kept at 2.5, while Z varies. Varying Z shifts the wavelengths longward of 2 μm from clearly showing tholin-like behavior at low metallicities to simply containing a gray opacity along with the gaseous absorption at high metallicities. Meanwhile, the transit spectra in the optical wavelength range up through 2 μm stay nearly constant, since the aerosols are always optically thick at the top-pressure cut-off, regardless of Z. When $Z = 0.1 \times Z_\odot$, the atmosphere falls into regime 3 with gray absorption at wavelengths blueward of 2 μm, but non-gray signatures redward of 2 μm. When $Z = 3.16 \times Z_\odot$, there is only a gray aerosol opacity like regime 2.

Comparing Figure 11 to the equivalent figure for clear atmospheres (Figure 6), one can see that there is a larger difference in shape for the hazy transit spectra than for the clear transit spectra. But, since F and Z can be highly degenerate in forming the aerosol opacity, this sensitivity to metallicity will not always translate into a precise measurement. If we want to get a handle on the atmospheric metallicity, we need the cloud top to not obscure wavelengths which break the degeneracy between metallicity and reference pressure (see Figure 6), or to thoroughly understand how metallicity shapes the amount of

aerosol present (see Figure 11). An example of this is the 700 K planet which shows the metallicity dependence of the 3.3 μm CH_4 feature even when aerosols are present at a pressure of 10^{-4} bar (see left-most panel of Figure 11). Note that these examples looked specifically at Titan tholin slab hazes, but the qualitative trade-offs between P_{top}, F, Z, and particle size will occur for other species of clouds or hazes too. The quantitative details will be different since each species has a different limiting constituent with a different solar abundance and each species has a different density.

When we simulate data with slab-type aerosols and attempt to do retrievals, we will find results consistent with these model sensitivity studies. If nature presents us with the unfortunate reality of an exoplanet atmosphere in regime 2 with gray aerosols obscuring almost all the gaseous absorption, we could end up with transit spectra that contain very little information about what aerosols are present and very little information about the gaseous absorption. On the other hand, we could have something in regime 1 or 3. That is, a thinner cloud deck or haze layer situated such that it gradually tapers before its top-pressure cut-off, imprinting lots of non-gray behavior while still allowing some gaseous absorption to show through. To really warrant the full slab aerosol parameterization in our MCMC fits, we need an atmosphere to fall into regime 3, where some wavelengths are cut off by P_{top} while others imprint some non-gray aerosol spectral signatures. The likelihood of one scenario over another is beyond the scope of our study, since it will depend on the details of vertical mixing, photochemistry, and microphysics in an atmosphere. Such processes have long been explored on Earth and other solar system bodies, and have begun to be applied to the study of exoplanet aerosols (Ackerman & Marley 2001; Lee et al. 2016; Gao et al. 2018, 2020; Gao & Benneke 2018; Ohno & Okuzumi 2018; Powell et al. 2018, 2019; Helling 2019; Kawashima & Ikoma 2019). Future observations with the JWST and ARIEL will hopefully reveal whether existing microphysical models are capturing the true behavior in exoplanet atmospheres.

5.1. Slab MCMC Experiment Results

In order to assess how well JWST-like transit spectra will be able to distinguish which aerosol species are present in exoplanets and how well parameters can be retrieved from hazy transit spectra, we perform a series of experiments. For each of the four fiducial temperatures we simulated JWST-like transit spectra for atmospheres with candidate aerosols that either condense in that temperature range, or are formed through photochemical processes. We then use the MCMC model to fit all of the transit spectra with the correct species of aerosol and all of the other candidate aerosols in the same grouping. By examining the quality of the fits and the retrieved parameters, we can determine whether the true aerosol would be preferred by a blind retrieval. The posteriors from the fits done with the correct aerosol species for a given simulated data set indicate how well measurements can be made for hazy transit spectra if you have identified the correct aerosol species.

We use the groupings of aerosols listed in Table 4. The slabs have a top-pressure cut-off of $10^{-4.5}$ bar, $F = 1.0$, and an overall atmospheric metallicity of $Z = 3 \times Z_{\odot}$. For each of these spatial distributions, we generate one spectra with a smaller modal particle size ($a_m = 0.05\ \mu$m) and one with a larger modal particle size ($a_m = 1.0\ \mu$m), always assuming a log-normal size distribution with dispersion $\sigma_a = 2.5$. The

Table 5
BIC Values for Retrievals on the 700 K Fiducial Atmosphere

True Species	KCl BIC	Na_2S BIC	Tholins BIC	Soot BIC	Max Depth–Min Depth (ppm)
Equilibrium Cloud 0.05 μm					
KCl	**35.4**	3769.7	⋯	⋯	6000
Na_2S	28852.0	**40.0**	⋯	⋯	6600
Equilibrium Cloud 1.0 μm					
KCl	**34.9**	67.8	⋯	⋯	7400
Na_2S	2483.1	**48.7**	⋯	⋯	6900
Slab 0.05 μm					
KCl	**67.8**	718.9	1750.4	10462.0	5700
Na_2S	23024.5	**39.6**	62.5	52.6	2900
Tholins	29748.4	**39.58**	**39.57**	**39.57**	2400
Soot	29772.7	**39.58**	**39.59**	**39.57**	2400
Slab 1.0 μm					
KCl	**41.2**	152.4	335.4	452.8	5900
Na_2S	5361.4	**43.3**	209.8	524.4	4000
Tholins	2786.4	84.9	**56.1**	129.7	2800
Soot	25788.5	89.1	95.7	**39.5**	2600

Note. Bold values in each row mark the preferred species based on a BIC comparison. The far-right column lists the maximum variation of depth within the transit spectrum. This provides a rough estimate of the signal size of the transit spectrum.

noise for each simulated spectrum came from scaling Pandexo's[4] noise calculation for HD209458b based on the different transit depths of our fiducial planets and assuming 10 transits are observed with each JWST instrument/mode and then stacked. This is then added in quadrature with the noise floor suggested by Greene et al. (2016). Stacking 10 transits yields a transit depth precision right at the noise floor for all the wavelengths shorter than 8 μm (that is 20, 30, and 60 ppm). Toward longer wavelengths the precision rises roughly linearly from around 60 ppm at 8 μm upwards of 100 ppm at 12 μm. In Table 4 there is a column listing the transit depth corresponding to the reference pressure R_0. The SNR for a single depth measurement is just that depth measurement divided by the precision of the measurement. However, the actual signal of the transit spectrum relies on detecting variation between wavelengths, so we also include a column listing the change in transit depth associated with changing the planet radius by one pressure scale height. Transit spectra typically vary with wavelength by an amount equal to several scale heights. This measure indicates that the SNR for detecting variation between wavelengths will be highest for the 700 K fiducial planet, then the 1800 K object, next the 1400 K object, and finally the 1000 K object. This ranking is driven by the fact that planets with low surface gravities and higher temperatures have larger scale heights. We provide another measure of the signal size for each simulated transit spectrum in Tables 5–8. The final column lists the difference between the maximum depth of the transit spectrum and the minimum depth of the transit spectrum. This measure of the signal accounts for the aerosol

[4] https://exoctk.stsci.edu/pandexo/calculation/new

Table 6
BIC Values for Retrievals on the 1000 K Fiducial Atmosphere

True Species	NaCl BIC	Na_2S BIC	Tholins BIC	Soot BIC	Max Depth–Min Depth (ppm)
Equilibrium Cloud 0.05 μm					
NaCl	**37.5**	366.3	⋯	⋯	330
Na_2S	324.94	**34.0**	⋯	⋯	270
Equilibrium Cloud 1.0 μm					
NaCl	**34.0**	49.2	⋯	⋯	450
Na_2S	178.5	**37.6**	⋯	⋯	210
Slab 0.05 μm					
NaCl	**40.8**	49.5	63.5	118.7	310
Na_2S	81.7	*41.0*	47.0	**40.0**	140
Tholins	102.4	41.9	**39.52**	**39.47**	110
Soot	102.2	**39.55**	42.3	**39.48**	110
Slab 1.0 μm					
NaCl	**39.5**	42.4	41.8	45.0	320
Na_2S	47.4	*44.0*	**40.6**	**40.7**	200
Tholins	78.6	**39.63**	**41.3**	**39.65**	120
Soot	91.5	**40.1**	**39.7**	*42.8*	140

Note. Bold values in each row mark the preferred species based on a BIC comparison. Italic values mark instances where the true species was disfavored by the BIC. The far-right column lists the maximum variation in the transit depth for use as an estimate of the signal size.

incorporated into the atmosphere. We will divide by 20 ppm to give a rough estimate of the SNR for spectral signatures. By this measure, the SNR for the cloudy and hazy versions of the 700 K planet range from around 100–400. The 1000 K planet SNRs are only around 5–20. The 1400 K planet SNR is a bit higher at 15–50, and the 1800 K planet SNR is 40–130.

For the 700 K grouping, we test soot, tholins, KCl, and Na_2S. The resulting best-fit transit spectra are shown in Figure 12, and histograms of the posteriors for fits with the correct aerosol species are shown in Figure 13. The bottom two sections of Table 5 summarizes the BIC for all of these fits. With $F = 1.0$ and metallicity $Z = 3.0 \times Z_{\odot}$, most of the slab aerosols show up as regime 2, essentially gray absorbers in the transit spectra. The exceptions are KCl which has much less constituent material to form from and Na_2S which has a slight downward slope from 8 to 12 μm. It is thus unsurprising that it is only in the case of small KCl particles that a model with soot is not able to mimic the true aerosol species. If the size and spatial distributions of aerosols are such that we get gray absorption across all wavelengths, it will be impossible to unambiguously distinguish which species is present. As we saw in the previous section, a smaller value of F or Z and a higher top pressure such that the aerosol layer is not optically thick all the way up to $P_{\rm top}$ is necessary for species to look distinct. It is feasible that F will be much less than 0.5. We chose such large values of Z and F in order to make sure KCl and Na_2S had non-negligible effects (and later NaCl, TiO_2, and Al_2O_3).

The posteriors and best-fit transit spectra for all the other fiducial atmospheres are shown in Figures 24–29 in the Appendix. The bottom two sections in Tables 6–8 summarize BIC. For the 1000 K grouping (Figures 24 and 27 in the Appendix), we test soot, tholins, NaCl, and Na_2S. Again, we see that the simulated data with soot and tholins are nearly flat, while the Na_2S and NaCl which contain less common atomic constituents exhibit non-gray behavior. The soot nearly fits all the species within the error bar, but is certainly a weaker fit than the true species in all cases, aside from 1.0 μm NaCl and 0.05 μm tholins. For the 1400 K grouping (Figures 25 and 28 in the Appendix), we test soot, tholins, iron, enstatite, and forsterite. All of the species are able to mimic each other very well when the modal particle size is 0.05 μm and they are essentially behaving as gray absorbers. None of the BIC values are more than 0.01 different than each other (see second from bottom section of Table 7). However, when the particles are 1.0 μm the silicate species have a slight arch to them from 0.7 to 4 μm and have a hint of a bump at the 10 μm feature. Tholins are more opaque from 0.7 to 4 μm than in the 10 μm window. Since the data are very high SNR, these subtle changes are enough that the true species is generally a better fit than the mimicking species. A look at the BIC values shows the silicates would be distinguished from Fe, tholins, or soot (see the bottom section of Table 7). For the 1800 K grouping (Figure 26 and Figure 29 in the Appendix), we test soot, tholins, iron, Al_2O_3, and TiO_2. In this temperature range, each species is able to mimic all others, aside from when soot is used to fit TiO_2 with 0.05 μm modal particle size. Looking back at Figure 3, we can see that gaseous absorption in the 10 μm window extends up to 10^{-4}–10^{-5} bar. This means that with our top-pressure cut-off of $10^{-4.5}$ bar none of them are really showing up in this wavelength range. That means that the aerosols only need to adapt to mimic wavelengths shorter than 4 μm.

These MCMC experiments on the slab-aerosol model agree well with our expectations from the parameter sensitivity studies. If aerosols are present in such a way that the transit spectrum falls into regime 2, they can be adequately treated as a gray opacity source. We only get an upper bound on particle size and the breadth of the size distribution, and it will be difficult to determine which species of aerosol is dominant. If aerosols fall into regime 1 or 3, then we can learn what species and size particles are present. Whether or not we can also gauge the overall atmospheric metallicity and temperature will depend on whether the aerosol is fully overshadowing the gaseous absorption at key wavelengths. Alternatively, if we can accurately couple microphysics to gas-phase chemistry within the retrieval framework, then the aerosols themselves can be highly sensitive to the metallicity.

6. Phase Equilibrium Clouds

Now we will move on to explore the range of behavior that can result when we use a phase equilibrium cloud model. Recall that this model incorporates some assumptions based on the thermodynamic properties of each species to set how much material will be incorporated into the cloud and where the base of the cloud forms, described in detail in Section 2.1. This means that the only additional free parameters on top of the structural parameters are the relative scale height between the aerosol particles and the gas (set by α), and the parameters used to describe the particle-size distribution. This treatment of clouds is intended to give a taste of how physically motivated assumptions based upon our understanding of cloud formation in the solar system might help us learn more from transit

Table 7
BIC Values for Retrievals on the 1400 K Fiducial Atmosphere

True Species	Mg_2SiO_4 BIC	$MgSiO_3$ BIC	Fe BIC	Tholins BIC	Soot BIC	Max Depth–Min Depth (ppm)
Equilibrium Cloud 0.05 μm						
Mg_2SiO_4	**34.8**	61.0	1064.0	⋯	⋯	480
$MgSiO_3$	60.9	**35.4**	1108.5	⋯	⋯	490
Fe	452.4	509.5	**34.3**	⋯	⋯	450
Equilibrium Cloud 1.0 μm						
Mg_2SiO_4	**34.6**	160.3	166.6	⋯	⋯	680
$MgSiO_3$	40.4	**35.4**	78.3	⋯	⋯	370
Fe	41.3	54.2	**33.9**	⋯	⋯	960
Slab 0.05 μm						
Mg_2SiO_4	**39.48**	⋯	**39.48**	**39.48**	**39.48**	270
$MgSiO_3$	**39.47**	⋯	**39.48**	**39.48**	**39.50**	270
Fe	**39.78**	⋯	**39.78**	**39.78**	**39.78**	280
Tholins	**39.48**	⋯	**39.47**	**39.47**	**39.47**	270
Soot	**39.48**	⋯	**39.48**	**39.48**	**39.48**	270
Slab 1.0 μm						
Mg_2SiO_4	**39.7**	⋯	47.1	49.0	52.0	330
$MgSiO_3$	**40.5**	⋯	50.1	49.7	46.8	360
Fe	43.9	⋯	**39.5**	44.6	**39.7**	420
Tholins	47.5	⋯	**40.3**	**40.1**	44.4	320
Soot	**40.37**	⋯	**40.34**	**40.37**	**43.1**	300

Note. Bold values in each row mark the preferred species based on a BIC comparison. We also include the maximum variation in the transit spectrum, one measure of the signal size.

Table 8
BIC Values for Retrievals on the 1800 K Fiducial Atmosphere

True Species	TiO_2 BIC	Fe BIC	Al_2O_3 BIC	Tholins BIC	Soot BIC	Max Depth–Min Depth (ppm)
Equilibrium Cloud 0.05 μm						
TiO_2	**33.9**	1542.9	118.8	⋯	⋯	1250
Fe	11879.0	**34.1**	6261.1	⋯	⋯	1400
Al_2O_3	1837.6	2795.4	**34.5**	⋯	⋯	1250
Equilibrium Cloud 1.0 μm						
TiO_2	**34.0**	57.7	43.6	⋯	⋯	2600
Fe	411	**317.2**	335.4	⋯	⋯	1100
Al_2O_3	76.2	403.5	**34.0**	⋯	⋯	1700
Slab 0.05 μm						
TiO_2	**39.7**	182.9	69.8	89.7	337.5	1200
Fe	42.35	**39.77**	**39.79**	**39.75**	**39.78**	800
Al_2O_3	50.9	84.9	**40.3**	56.8	75.4	860
Tholins	42.05	**39.60**	**39.55**	**39.58**	**39.61**	800
Soot	42.1	**39.57**	**39.60**	**39.59**	**39.59**	800
Slab 1.0 μm						
TiO_2	**39.5**	54.1	40.8	41.8	41.6	2300
Fe	59.8	**39.6**	66.0	52.2	52.7	1100
Al_2O_3	47.7	95.8	**39.7**	117.7	97.2	1400
Tholins	61.2	**40.85**	58.3	**40.76**	**39.97**	850
Soot	45.8	75.8	42.4	43.5	**39.9**	840

Note. Bold values in each row mark the preferred species based on a BIC comparison. The far-right column lists the maximum change in the transit spectrum for use as a measure of the signal size.

spectra than we get from using empirical models alone. Other physically motivated parameterizations could and should be considered as we move toward fitting real JWST transit spectra.

Figure 14 shows the approximate ratio of cloud particle number density to gas number density versus pressure for the possible condensates in each of our four fiducial atmospheres

(assuming a 0.5 μm modal particle size with a log-normal dispersion of 2.5 and a fall-off of $\alpha = 1.0$). Different species will condense at different levels in the atmosphere for a given temperature, and some species form more particles than others. For example, Na_2S condenses much higher up in the 700 K atmosphere than in the 1000 K atmosphere, and Fe condenses higher up in the 1400 K atmosphere than in the 1800 K atmosphere. Recall that the number of aerosol particles is limited by the solar mixing ratio of the aerosol species' least abundant constituent atomic species. The solar mixing ratios of Cl, K, and Ti to H are all of order 10^{-7}, so the number densities of aerosol particles of KCl, NaCl, and TiO_2 are much smaller than those of the other possible condensate species, even assuming the same particle-size distribution.

First, we will look at transit contribution functions for a Mg_2SiO_4 cloud in the 1400 K fiducial atmosphere to get a sense for what is going on as we change α (Figure 15). In the left column, the metallicity is $Z = 1 \times Z_\odot$ and in the right column the metallicity is $Z = 3 \times Z_\odot$. The first row has $\alpha = 0$, then the second has $\alpha = 2$, and the third has $\alpha = 4$. The bottom-left panel shows the contribution function for the clear 1400 K atmosphere, and the bottom-right panel shows the transit spectra for all the other panels. Spectra shown by solid lines correspond to atmospheres with $Z = 3 \times Z_\odot$ and spectra shown by dashed lines correspond to $Z = 1 \times Z_\odot$. The particle-size distribution has a modal particle size of 1.0 μm and a dispersion of $\sigma_a = 2.5$. The cloud base always forms a little deeper than 10^{-4} bar. For lower values of α, there are cloud particles contributing opacity higher up in the atmosphere, while for higher values of α the cloud only contributes within a small range of pressures. As metallicity increases the cloud opacity makes up a larger portion of the contribution function than the gaseous opacity, but it never totally dominates, even for $\alpha = 0$ and $Z = 3 \times Z_\odot$. We can see the cloud base in the contribution functions around 10^{-4} bar, then a gap in contribution, and then the patterns of the gaseous absorption at higher pressures picks up. This is why, in the corresponding transit spectra, we can always see the gaseous absorption peaks.

Transit spectra for all the candidate cloud species with a range of Z and α are shown in Figure 16 and in Figures 30–32 in the Appendix, grouped by temperature. Z, cloud species, and the particle-size distribution work together to modulate how optically thin or thick the cloud is. In the examples shown in Figure 15, the cloud is always optically thin enough that the gaseous absorption is still affecting the transit spectrum. However, for many species, clouds can overpower gaseous extinction at many wavelengths (e.g., Na_2S in the 1000 K atmosphere, $MgSiO_3$ in the 1400 K atmosphere if metallicity is high, Fe in the 1800 K atmosphere, and Al_2O_3 in the 1800 K atmosphere if metallicity is high). Once one chooses a cloud species and a temperature, the cloud's base pressure is set. If the cloud base is at a middling pressure or deep in the atmosphere (say deeper than 10^{-2} bar), then α shapes whether the cloud is extended or resides only at depth. If the cloud base forms very high up in the atmosphere, then varying α will have less effect.

A key point we wish to emphasize with Figure 16 and Figures 30–32 in the Appendix, is that changing Z and α can only alter the transit spectra within a small range of behaviors in some cases (e.g., KCl, NaCl, and TiO_2), while in others it can move the atmosphere from appearing nearly clear to appearing very clouded (e.g., Fe and Mg_2SiO_4). When a large number of particles form, then the atmosphere looks very cloudy regardless of α (e.g., Na_2S in the 1000 K atmosphere, $MgSiO_3$ in the 1400 K atmosphere, or Fe in the 1800 K atmosphere). In these cases, changing Z can make a large difference to the balance between gaseous opacity and cloud opacity. When a very small number of particles form (e.g., KCl at 700 K, NaCl at 1000 K, TiO_2 at 1800 K), then the transit spectra can never appear much different from a clear atmosphere, and changing the metallicity is mostly changing the gaseous absorption features.

Clearly, assuming the cloud base must form where the Clausius–Clapeyron line intersects with the T–P profile and using only the material in excess of saturation vapor pressure places severe constraints on the patterns a cloud species can impart onto the transit spectrum of a given atmosphere. If these assumptions are a good approximation for actual cloud formation on exoplanets, then this is good news. One should be able to break degeneracies and obtain much tighter constraints on atmosphere and aerosol properties. If these assumptions are wrong, then one will struggle to fit the data at all or will end up with erroneous results. We will see the consequences of this in the MCMC experiments in the next section. Compared to the results for the slab aerosols, it is much easier to differentiate between the candidate species. This is partly because of the model and partly because the sample data tend to exhibit more non-gray behavior than the sample data for the hazy experiments. When the correct species is used in the fit, we also get tighter constraints on Z than for the slab aerosol.

6.1. Equilibrium Cloud MCMC Experiment Results

Is one likely to be able to unambiguously identify condensing species with JWST transit spectra? To address this question, we now consider the results of MCMC retrieval experiments for transit spectra with phase equilibrium clouds. In the experiment we simulated data for each possible cloud species with a tapering shape parameter of $\alpha = 2$, and an overall atmospheric metallicity of $Z = 3 \times Z_\odot$. Like the slab-MCMC experiments, we compare one spectrum with a smaller (0.05 μm) modal particle size and one with a larger (1.0 μm) modal particle size, and we always used a log-normal size distribution with dispersion 2.5. The top two sections of Tables 5–8 display the BIC values for all the fits.

The best-fit spectra for the 1400 K atmospheres are shown in Figure 17. Fe and the two types of silicates look very different for the small modal particle size. Distinguishing between $MgSiO_3$ and Mg_2SiO_4 is not as easy, but it does look feasible provided sufficient SNR and spectral resolution to locate the peak and shape of the 10 μm resonance feature, especially given the high SNR of these simulated transit spectra. When the particle-size distribution has a mode of 1 μm, all three species are able to mimic each other quite well. If α were lower or the metallicity were higher, then the 10 μm feature might rise above the gas absorption, again making iron and the two types of silicates more distinguishable. However, given the high SNR for the 1400 K object, the BIC values still favor the correct species in every case.

The posteriors for each MCMC fit done with the correct species are shown in Figure 18. The modal particle size and the dispersion of the size distribution are accurately retrieved in all cases. The tapering parameter α is constrained for the 1 μm Fe and forsterite, but otherwise just places an upper bound. For the smaller Fe particles in particular, α is poorly constrained. The reference pressure and temperature are more tightly constrained for the large particle sizes. The temperature for small iron

particles and large enstatite particles skews a bit higher than the true value, accompanied by a slight shift toward lower reference pressures. Within our prior of 0.1–3.16×solar, the metallicity is only able to place a lower bound. Note that this lower bound is much tighter than those placed on spectra which had slab aerosols.

We also show results for all the other fiducial atmospheres in the Appendix, Figures 33–38.

For the 700 K atmospheres, when the size distribution has 0.05 μm modal particles, the fit with the true species is stronger than the fit with the wrong species. For the size distributions with 1.0 μm modal particles, the wrong species provides a suitable fit to the data. With this modal particle size, the amount of material available to make KCl or Na_2S particles given our equilibrium assumptions is simply not sufficient to create a significant cloud opacity compared to the gaseous opacity. For the 1000 K atmospheres, in all cases where the underlying data have strong effects due to the aerosols, Na_2S and NaCl are very distinguishable. It is only for the 1.0 μm NaCl cloud that the two species fit the data equally well. In the 1000 K atmosphere, the Na_2S cloud base forms deeper in the atmosphere, around 1 bar, where there is enough material to make a reasonable number of particles. In contrast, in the 700 K atmosphere the Na_2S cloud base formed up around 10^{-5} bar. For the 1800 K grouping we tested Fe, TiO_2, and Al_2O_3. Similar to the other temperatures, when particle sizes are smaller, then the three species have trouble mimicking each other. When particles sizes are 1.0 μm, they are almost indistinguishable. However, with very high SNR, Fe may be unable to mimic the Al_2O_3 cloud.

The posteriors for the 1000 and 1800 K atmospheres mostly show similar results to the 1400 K atmosphere. The metallicity is only a lower bound and α is only an upper bound. The lower bounds on metallicity are again much tighter than those for the slab aerosols. The posteriors for the 1.0 μm NaCl clouds in the 1000 K atmosphere show that the particle-size distribution and α are totally unconstrained. This reflects the fact that the NaCl cloud has only a small effect on the transit spectrum. In the 700 K atmosphere, the metallicity was actually retrieved for all combinations of species and particle sizes, not just a lower bound. The correct value of α is also retrieved. The constraints for the 700 K are tightest, then the 1800 K planet and finally the 1400 and 1000 K planets have looser constraints. This reflects the varying scale heights of the planets compared to the precision of the depth measurements.

Overall, it is very clear from the parameter sensitivity studies and MCMC experiment results that incorporating some assumptions based on thermodynamics into your model can lead to fewer degeneracies between model parameters and makes aerosol species appear more distinct. This is no surprise. However, the benefits of the equilibrium cloud model depend heavily on whether you have made good assumptions. If condensed aerosols in exoplanet atmospheres form roughly where the *T–P* profile crosses the Clausius–Clapeyron line, then fall off in density in a manner proportional to the gaseous pressure scale height, and if they have a small modal particle size (less than 1.0 μm), then they tend to embed a lot of information about the species and size distribution of the aerosol in the transit spectra. The clouds with larger particle sizes were also statistically distinguishable based on the BIC, even in cases without obvious discrepancies between their best-fit transit spectra and the true transit spectra.

7. Summary and Conclusions

First, we demonstrated the sensitivity of JWST-like transit spectra to atmospheric properties, such as temperature and metallicity, and to aerosol properties, such as particle-size distribution, aerosol species, and spatial extent of aerosols. In our explorations, we considered spectra with 15 different aerosol species. We did our calculations using METIS and two forms of aerosol parameterization. One type of aerosol was a "slab" specified by a number fraction of available material incorporated into the aerosol, F, and an arbitrary top-pressure cut-off, $P_{\rm top}$. The second type was a "phase equilibrium" cloud which assigns the base of a condensing species to form where the *T–P* profile intersects with the Clausius–Clapeyron line, and then uses a free parameter, α, to describe how quickly the density of the aerosol falls off relative to the density of the gas. We paired these two types of aerosol spatial parameterization with log-normal size distributions. With this context of parameter sensitivity laid out, we then presented results from a wide array of retrieval experiments to look in depth at the prospects for inferring aerosol and planetary properties from a variety of hazy and cloudy simulated JWST transit spectra. We focused on fiducial atmospheres with relatively warm temperatures of 700, 1000, 1400, and 1800 K in order to include all the candidate condensing aerosol species in our set of 15 outside of NH_3 and H_2O clouds.

Before we review the results of our retrieval experiments and their implications for the JWST, we pause to remind the reader of a few caveats. As mentioned throughout the methods and results sections, our forward model for retrievals and simulated data assumes isothermal atmospheres, uniform aerosol coverage, and equilibrium chemistry with varying Z, but always a solar C/O ratio. This forward model would need modifications to also allow the variation of C/O ratio, patchy clouds, and a parameterized *T–P* profile rather than an isothermal profile in order to be applied to real data. Several works have already presented the problem with assuming uniform aerosol coverage and found successful remedies (Line & Parmentier 2016; MacDonald & Madhusudhan 2017). Rocchetto et al. (2016) point out biases that will arise from assuming an isothermal atmosphere in fitting real observations of transit spectra, and Miller-Ricci Kempton et al. (2012) compare results from assuming equilibrium chemistry versus allowing non-equilibrium mixing ratios when fitting the transit spectrum of GJ1214b. We have considered only metallicities of 0.1–3.16 $\times$ $Z_\odot$. This is a reasonable range for Jupiter-sized planets, but needs to be extended up to higher metallicities to explore smaller mass planets. With this in mind, our findings should be interpreted as indicative of the information content about aerosols and other atmospheric properties that can feasibly be encoded in JWST-like transit spectra of giant warm cloudy and hazy exoplanets. The retrieval approach used here is not intended to be applied to real data, rather it is meant to provide an upper limit on the precision of constraints that can be placed on model parameters and demonstrate two options for incorporating aerosol parameterizations with greater physical significance in future retrieval efforts.

We now summarize the questions we investigated in this paper and the answers we found.

1. Which JWST wavelengths contain the most information about aerosol properties and which provide information about gaseous absorption? Looking at Jacobians and transit spectra for a representative array of particle-size distributions and aerosols species, we found that it is the

combination of JWST's longest (8+ μm) and shortest (less than 2 μm) wavelength coverage which provide the most information about 0.1–1.0 μm aerosols, while the midIR wavelengths usually provide information about gaseous absorption (unless aerosols are present at very high altitudes). In other words, transit spectra which appear very flat at shorter wavelengths, could still exhibit recognizable spectral features from gaseous absorption, or from the aerosols themselves in the longer wavelength range accessible by the JWST. This trend arises both because there are strong gaseous absorption features in the near–midIR and because of the optical properties of many of the leading candidate aerosol species.

2. How well can we recover atmospheric metallicities and temperatures, even when aerosols are present as we extend the wavelength coverage of transit spectra? The metallicity was often difficult to retrieve when aerosols are present at high altitudes. The peaks of the broad groupings of absorption features at 2.5–3 μm and 4.5–8.5 μm are usually recognizable in transit spectra, even with aerosols present. However, the shapes of the edges and troughs of these gaseous absorption features relative to the peaks are needed to show a change due to metallicity that is not degenerate with simply changing the reference pressure or the amount of available material that is incorporated into aerosols. On the other hand, if the amount and/or species of aerosol present could be accurately tied to the bulk metallicity of the atmosphere, then spectra with aerosols are actually very sensitive to the metallicity of the atmosphere (often much more sensitive than the gas alone). This result emphasizes the importance of developing relevant microphysical models and using them to place reasonable priors on how much available material is likely to be incorporated into aerosols. That will only be possible if we know what species are present. The metallicities explored here occupy a narrow range when compared to the error bar of many existing measurements of exoplanet atmospheric metallicities (Welbanks et al. 2019). We cannot rule out the possibility that one could still distinguish between the low metallicity range explored here and metallicities that range up to several orders of magnitude higher.
3. Can we uniquely identify which dominant aerosol species are present in atmospheres using JWST transit spectroscopy? Can we constrain the size distribution of aerosols? How do these tasks differ for condensed clouds and photochemical hazes? We found that log-normal size distributions of different aerosol species could often be distinguished, as long as modal particle sizes and spatial positions are such that the aerosols do not just behave as a gray opacity source relative to the gaseous contributions to the transit spectra. Aerosols can present themselves as a gray opacity source when particles are large, when the aerosol opacity is negligible compared to gas opacity so it only raises the bottoms of absorption windows slightly, or when there is a steep top-pressure cut-off to the physical location of aerosols at a height such that the aerosol is optically thick for all wavelengths of light. The good news is that this type of aerosol can often be marginalized over to retrieve unbiased temperatures. The bad news is that it does not allow us to identify what species the aerosol is. In particular, different types of hydrocarbon haze (various soots, tholins, poly-HCN) tend to look very similar. They can mimic each other and other aerosols quite well if the other aerosol either behaves as a gray opacity source or is just slightly different from a gray opacity source (e.g., with a slight downward slope from 8 to 10 μm). However, in many cases the aerosol type, modal particle size, and spread in particle-size distribution can be recovered. The slab and phase equilibrium aerosol formulations of NaCl and KCl with small particles look quite distinctive. The Na_2S cloud with equilibrium base in the 1000 K atmosphere for both 0.05 and 1.0 μm particles, and in the 700 K atmosphere for just 0.05 μm particles. For 0.05 μm particles, silicates and iron formed as equilibrium base in 1400 K look very distinct. At 1800 K equilibrium base, Al_2O_3, TiO_2, and Fe look different when the modal particle size is 0.05 μm. Different types of silicates (enstatite versus forsterite and different iron percentages) may even be distinguishable if the 10 μm feature is observable, and the observations have sufficient SNR and spectral resolution. This requires the presence of 0.1–1 μm size particles lofted up in the air above 10^{-4}–10^{-5} bar for a strong 10 μm feature to be visible above water absorption. The question thus becomes, will aerosols form with size and spatial distributions such that they appear gray, or will they form in such a way as to leave distinctive features indicating their nature in transit spectroscopy? Answering this is beyond the scope of our paper, as it relies on detailed microphysical models and GCMs. This is the purview of coupled dynamical cores and microphysical models and is still an open question.

Overall, our results support the community's widespread optimism for JWST and ARIEL transit spectroscopy. Through a coincidence of stronger gaseous absorption and weaker aerosol extinction, the 4–9 μm range is consistently most likely to be dominated by gaseous absorption, even when the shorter and longer wavelengths tend to be shaped by aerosols across a wide variety of temperatures and aerosol species. This means that, despite the fact that some transit spectra lack gaseous absorption features in current observations, it is still feasible that the JWST could detect signatures of gaseous absorption in the near through midIR. For both a slab-type aerosol and a phase equilibrium cloud, our ability to distinguish between some of the leading candidate aerosol species and recover particle-size distributions will depend on what the ground truth is in the exoplanet atmospheres, even with the full wavelength coverage of the JWST. If nature is kind, and aerosols form such that we can unambiguously determine what the dominant aerosol species are and make empirical measurements of particle-size distributions and spatial extent, then this information would provide a valuable test of whether theories developed with GCMs and detailed microphysical modeling are correctly capturing the behavior of cloudy hazy exoplanet atmospheres. Our results point to the importance of continuing efforts to accurately link enrichment and depletion by aerosols to gas-phase chemistry within retrievals. This will ultimately be the key to inferring metallicities of cloudy hazy atmospheres.

The authors would like to acknowledge support for this research under NASA WFIRST-SIT award # NNG16PJ24C and NASA Grant NNX15AE19G. This research has made use of the NASA Exoplanet Archive, which is operated by the California Institute of Technology, under contract with the

National Aeronautics and Space Administration under the Exoplanet Exploration Program.

Software: astropy (Astropy Collaboration et al. 2013), numpy (Oliphant 2006; van der Walt et al. 2006), scipy (Millman & Aivazis 2011; Oliphant 2007), matplotlib (Hunter 2007), emcee (Foreman-Mackey et al. 2013; Goodman & Weare 2010), corner (Foreman-Mackey 2016), mpi4py (Dalcin et al. 2011).

Appendix

Figures 19 and 20 illustrate optical properties of candidate aerosol species for the reader's convenience. The rest of this appendix includes figures similar to those described in the text but now rounding out all four aerosol temperature groupings. Figures 21–23 show Jacobians for different aerosol species and modal particle size, similar to Figure 9.

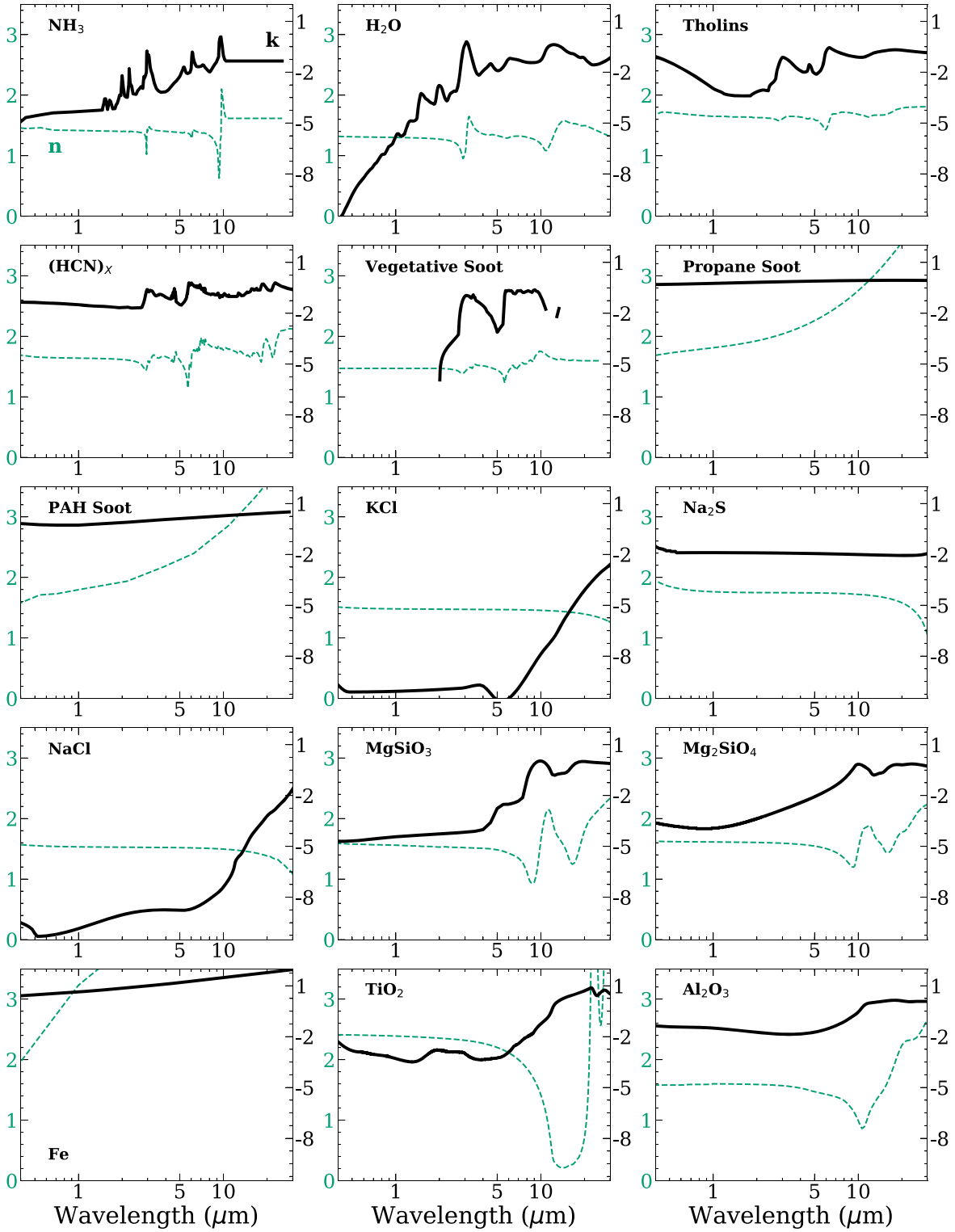

Figure 19. Complex indices of refraction used to incorporate aerosols into our models. Black lines are the base 10 log of the imaginary part and dashed green lines are base 10 log of the real part. References are in Table 2. Note that wavelength coverage is incomplete for vegetative soot.

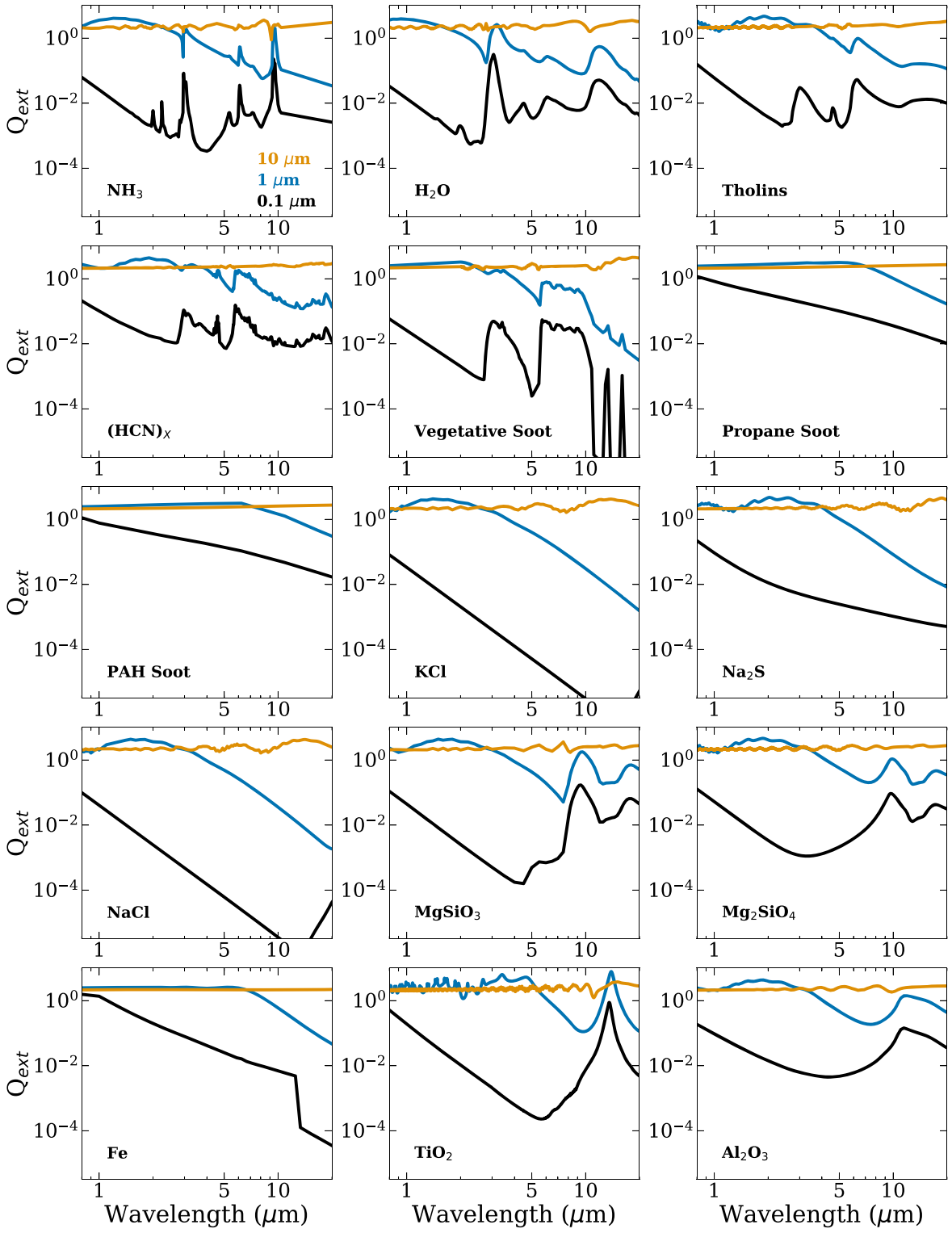

Figure 20. Extinction efficiency factors for several particle sizes. Recall, $\sigma_{\rm ext} = Q_{\rm ext} \times \pi a^2$, where a is the radius of the particle.

Figures 24–26 show the posterior probability distribution for fits to transit spectra with slab aerosols, similar to Figure 13. Figures 27–29 show the simulated data with slab aerosols and transit spectra fit with different aerosol species, similar to Figure 12.

Figures 30–32 show transit spectra with a phase equilibrium cloud as scale height and metallicity vary for various species, similar to Figure 16. Figures 33–35 show the posterior probability distributions for fits to transit spectra with phase equilibrium clouds, similar to Figure 18. Figures 36–38 show the simulated transit spectra with phase equilibrium clouds compared to transit spectra fit with various species, similar to Figure 17.

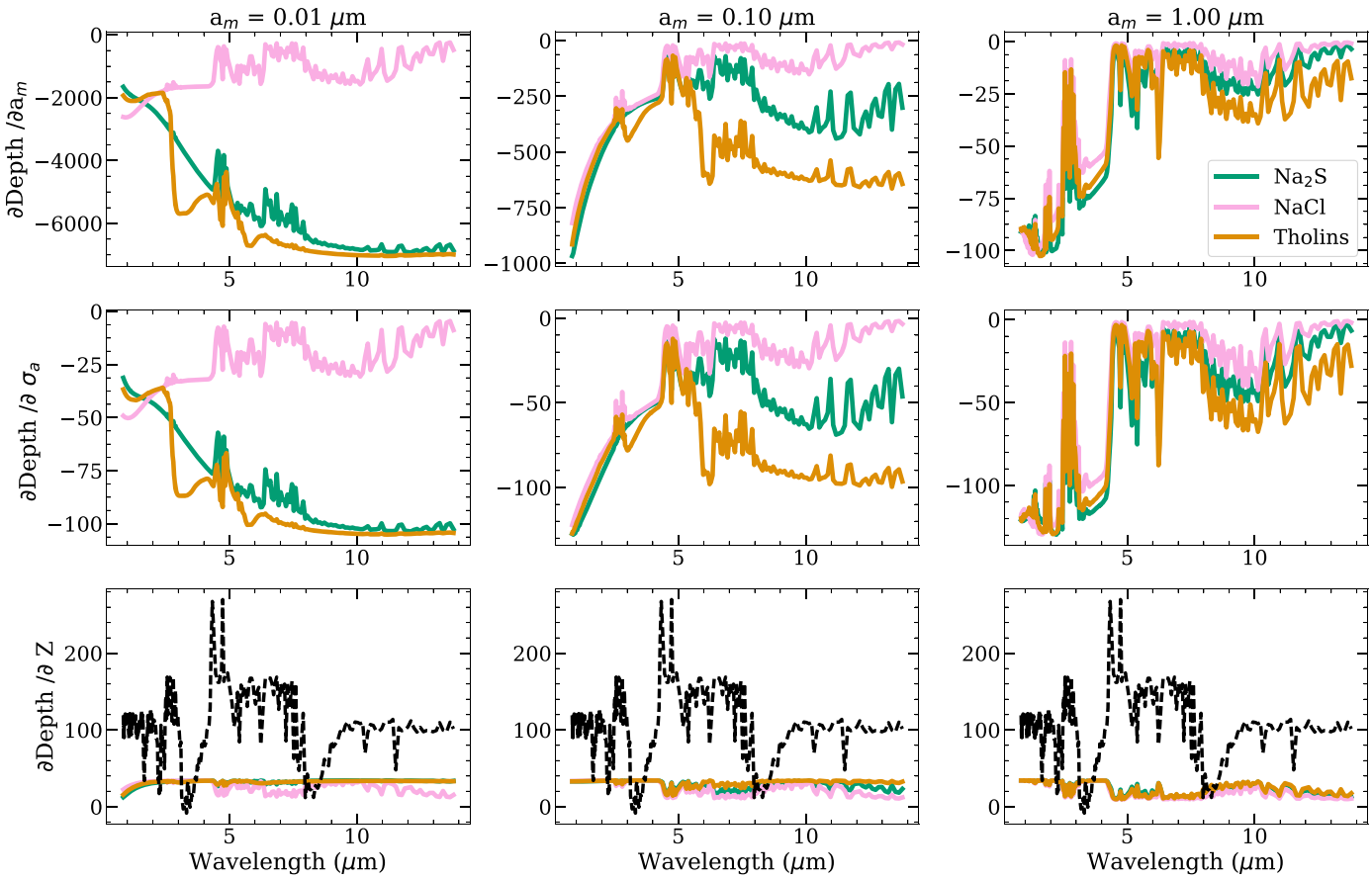

Figure 21. Jacobians for our 1000 K fiducial atmosphere when Na_2S (green), NaCl (pink), and Titan tholins (orange) are included as slab aerosols. We have made the same assumptions about the slab aerosol as in Figure 9: varying F such that $F\times$ the solar abundance of the limiting atomic species equal to 3×10^{-6}, setting the top-pressure cut-off too high up to make a difference, and using a size dispersion of 2.5 on the log-normal size distribution. Each column shows results for a different modal particle size, as labeled. The top row shows the partial derivative of transit depth with respect to modal particle size, the middle row shows the partial derivative with respect to size dispersion, and the bottom row shows the partial derivative with respect to metallicity. Again, the black dashed lines indicate the partial derivative with metallicity for the clear atmosphere.

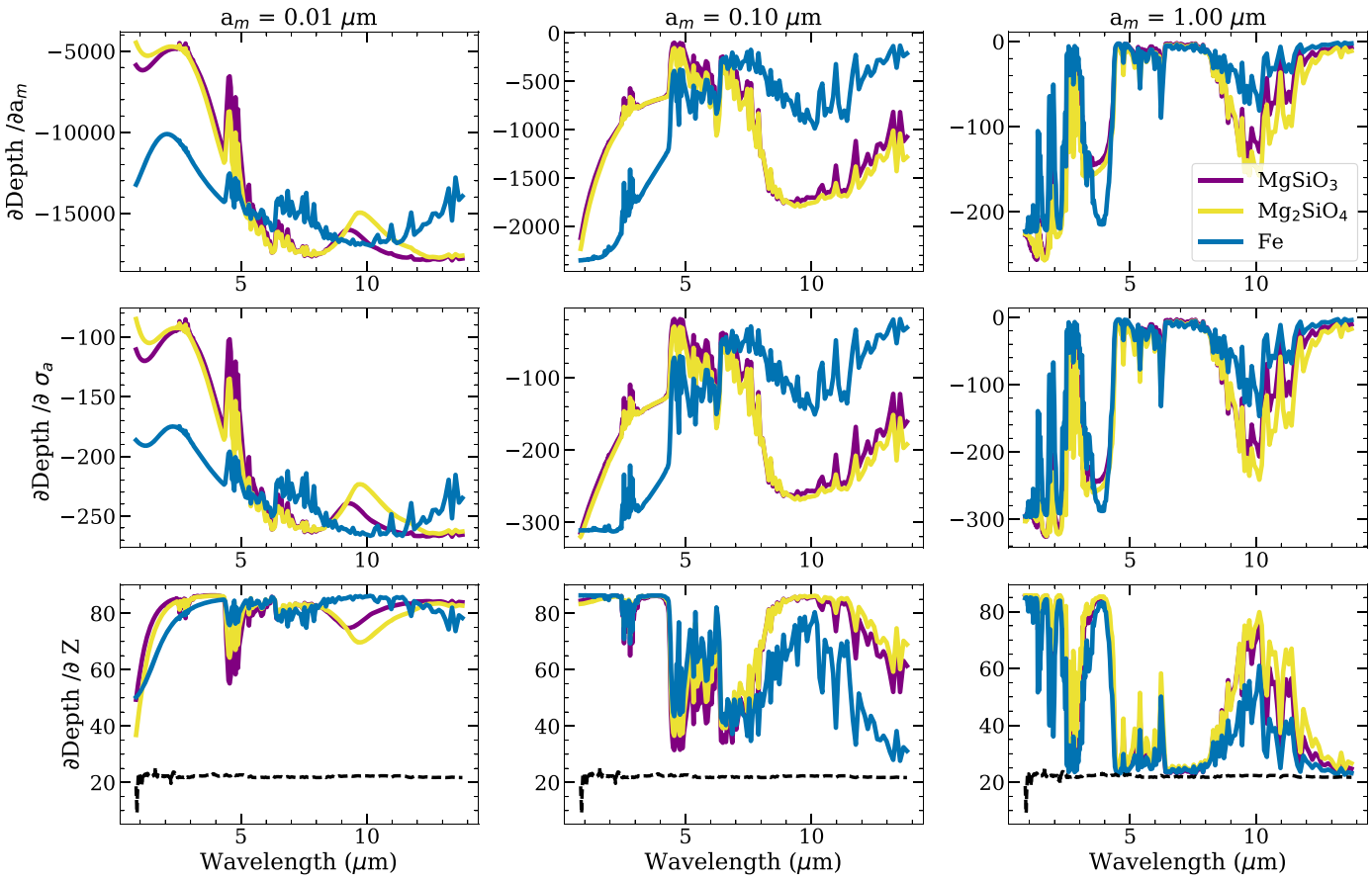

Figure 22. Jacobians for our 1400 K fiducial atmosphere when $MgSiO_3$ (purple), Mg_2SiO_4 (yellow), and Fe (blue) are included as slab aerosols. Each column sets a different modal particle size and each row is the partial derivative of transit depth with respect to a different parameter. In the panels showing the Jacobians with respect to Z (bottom row) we include a black dashed line showing the result for a clear atmosphere. We set F for each aerosol species such that $F\times$ the solar abundance of the limiting atomic species equal to 3×10^{-6}. σ_a is always set to 2.5. $P_{\rm top}$ is set to 10^{-8} bar so as to be well above the altitude where there is no longer enough material to form significant numbers of particles.

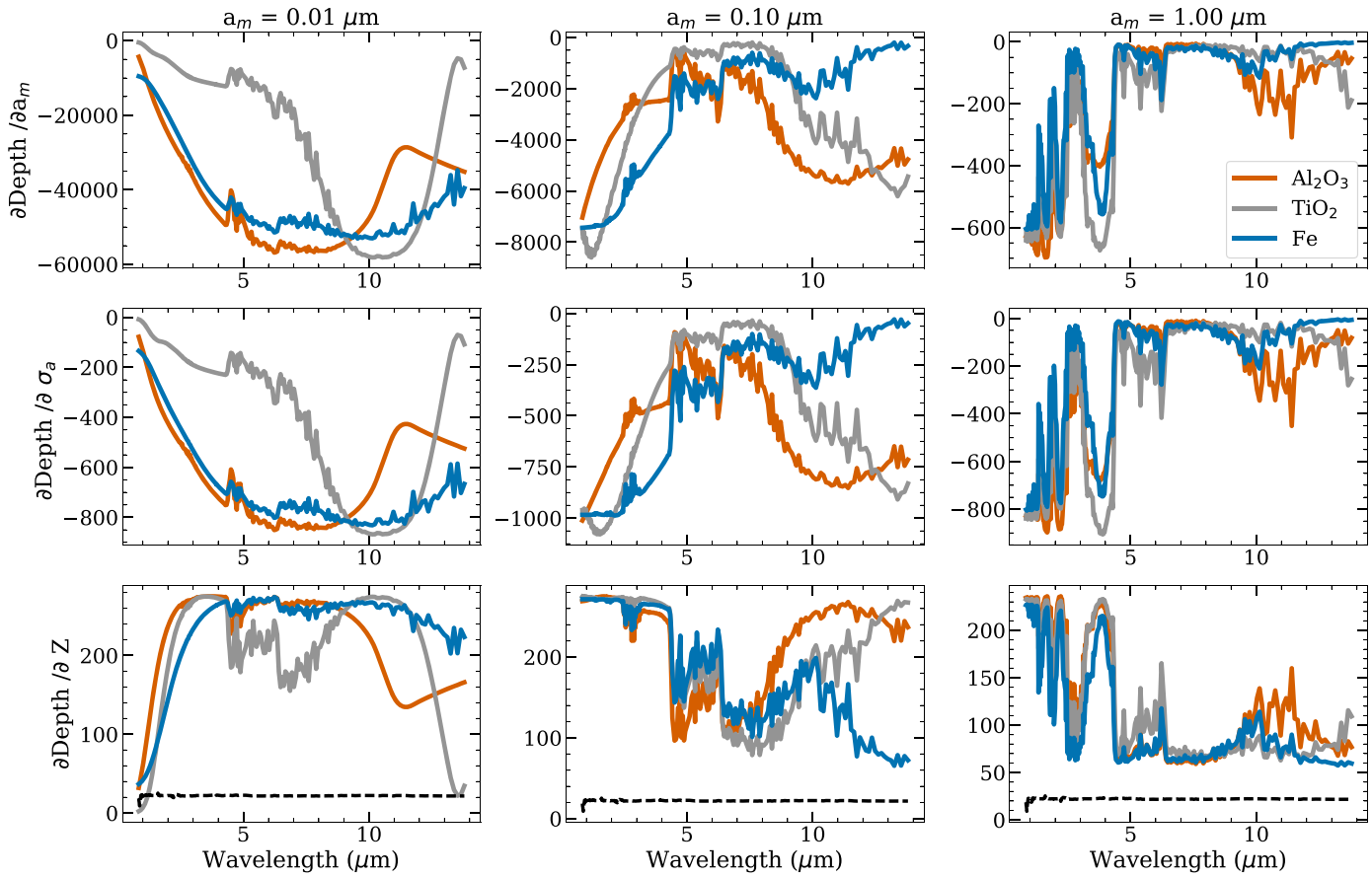

Figure 23. Jacobians for the 1800 K fiducial atmosphere when Al_2O_3 (rust), TiO_2 (gray), and Fe (blue) are included as slab aerosols. The top row shows the partial derivative of transit depth with respect to modal particle size, the center row shows the partial derivative with respect to the dispersion of the log-normal particle-size distribution, and the bottom shows the partial derivative with respect to metallicity. The panels in the bottom row include a black dashed line with the metallicity Jacobian for a clear atmosphere. Each column has a different modal particle size. The same values of $P_{\rm top} = 10^{-8}$ bar and $\sigma_a = 2.5$ are used throughout all the panels for all species. F is chosen for each species such that $F\times$ the solar abundance of the limiting atomic species equals 3×10^{-6}.

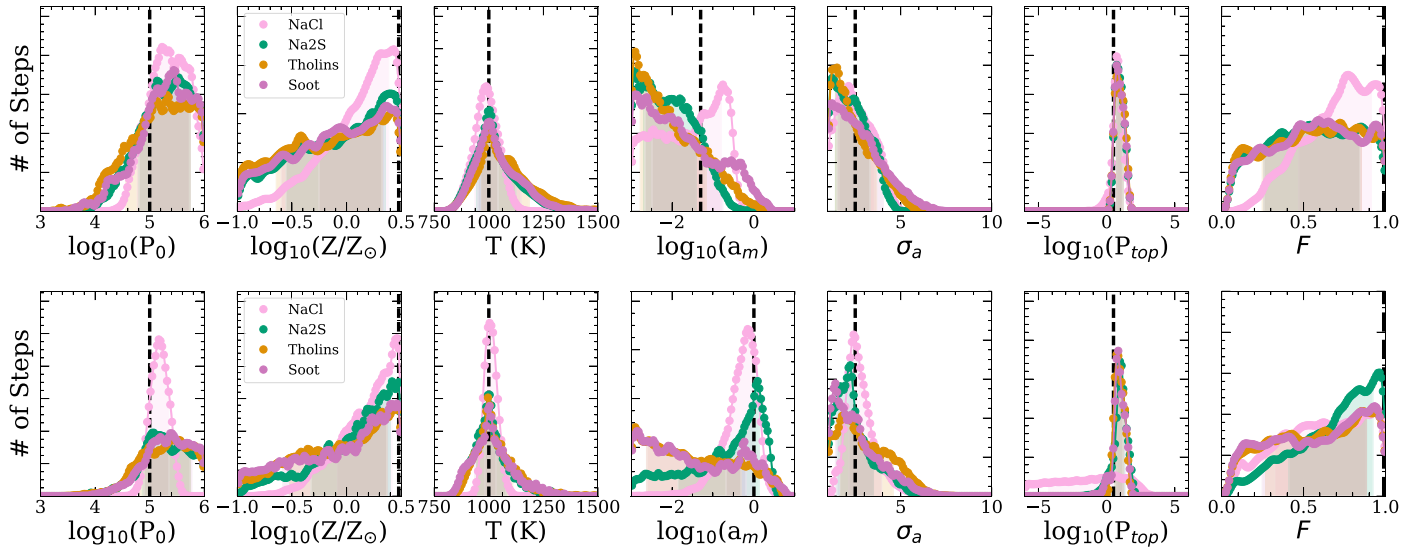

Figure 24. Histograms of parameter posteriors for the 1000 K fiducial atmosphere with slab aerosols. These are for MCMC fits with the correct species. Colors show different species of aerosols and vertical lines show true values of each parameter. In the top row, data was simulated with a modal particle size of 0.05 μm. In the bottom row, data was simulated with a modal particle size of 1 μm. Shaded regions mark the part of the posterior that falls between the 16th and 84th percentiles.

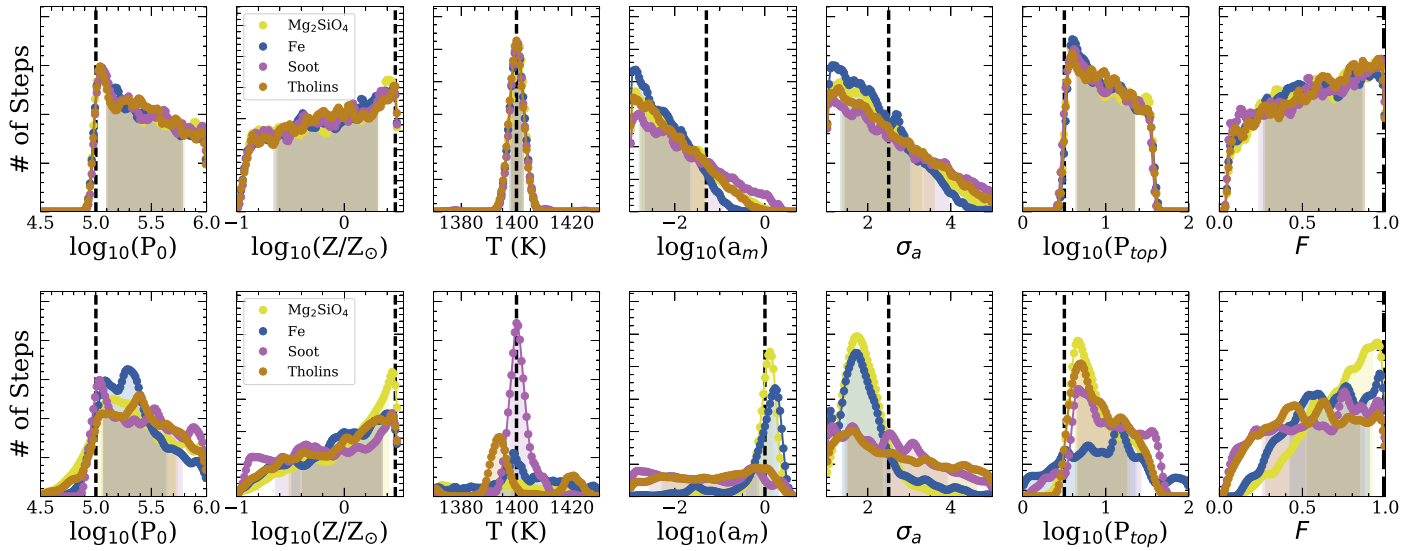

Figure 25. Histograms of posteriors from the MCMC fits for the 1400 K fiducial atmosphere with different slab aerosols. Each color is a retrieval for simulated data with a different species of aerosol. The same species of aerosol is used for simulated data and MCMC fits. In the top row the modal particle size was 0.05 μm, while in the bottom row the modal particle size was 1 μm. Vertical lines indicate the true parameter values. Shaded regions mark the part of the posterior that falls between the 16th and 84th percentiles.

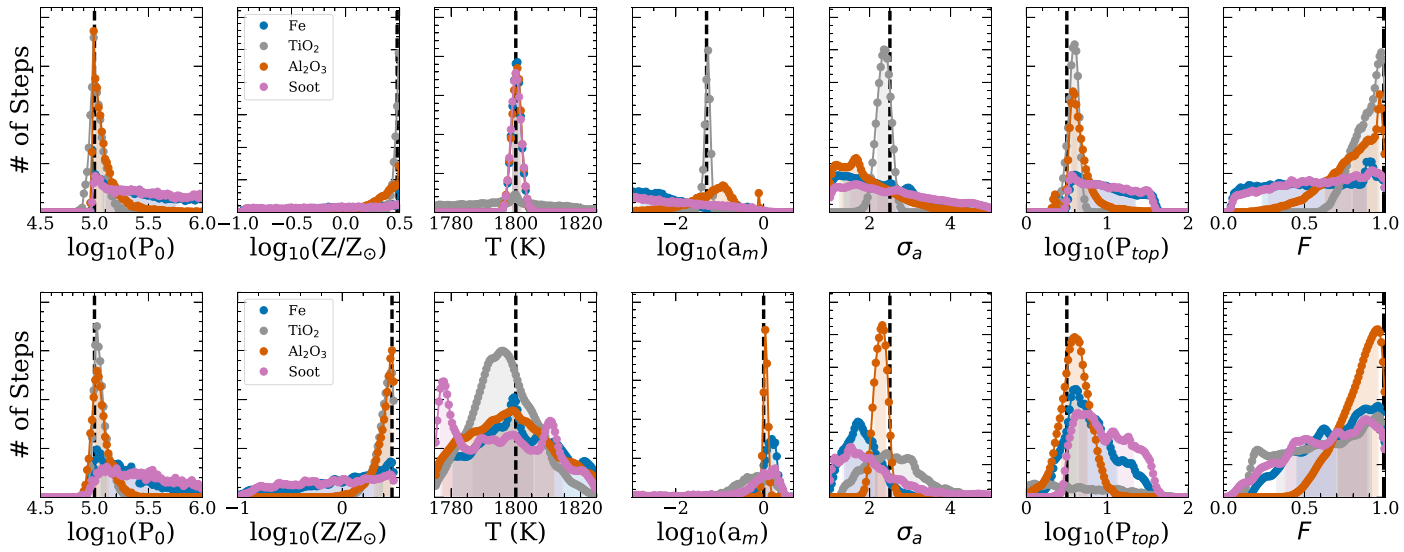

Figure 26. Histograms of parameter posteriors for the 1800 K fiducial atmosphere with slab aerosols. Colors show results for data simulated with different species of aerosols. The vertical lines mark the true values of parameters used when simulating data. In the top row the modal particle size was 0.05 μm, and in the bottom row the modal particle size was 1 μm. Again, shaded regions mark the part of the posterior that falls between the 16th and 84th percentiles.

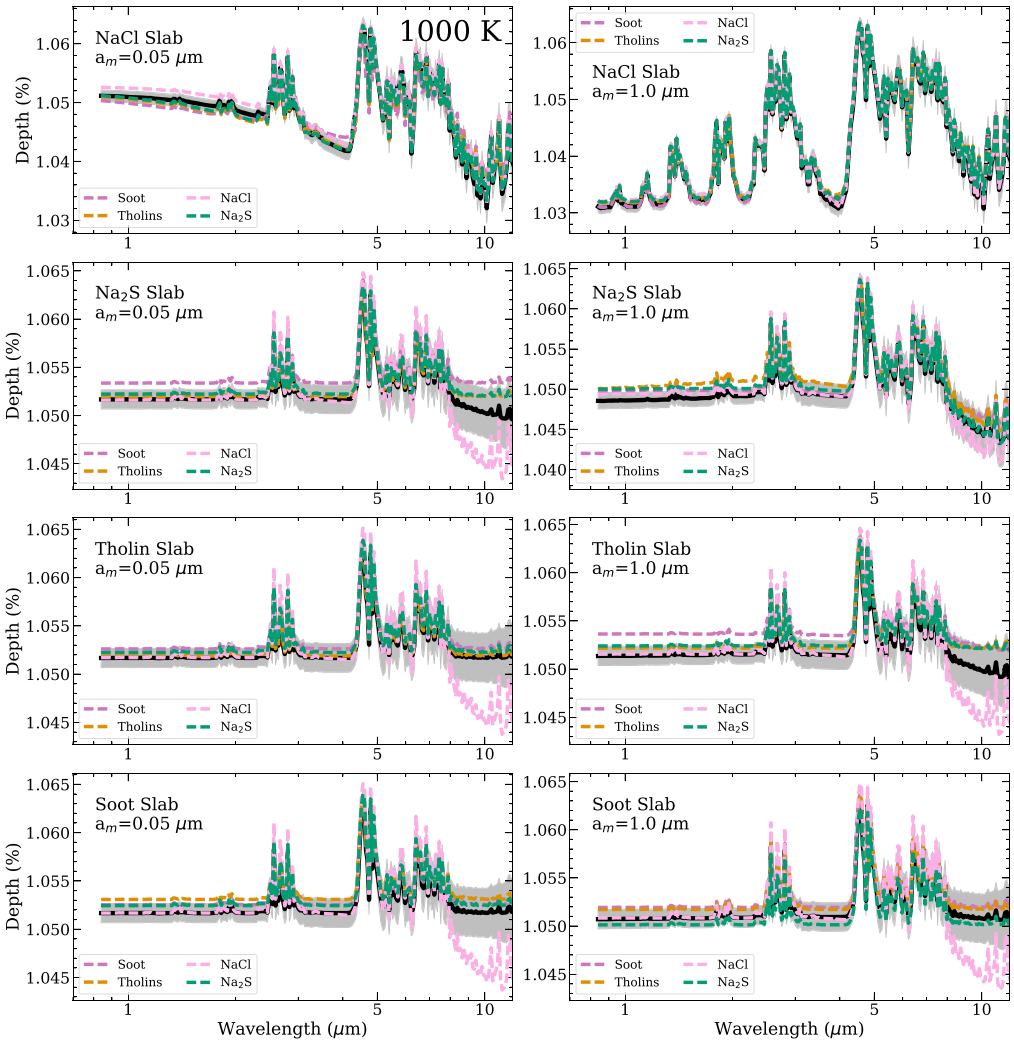

Figure 27. Results for the MCMC experiments with aerosols in the 1000 K fiducial atmosphere. The solid black line in each panel shows the simulated data and the surrounding light shading indicates the error envelope. In the top row the true species is NaCl, second row Na_2S, third row Titan tholins, and finally soot in the bottom row. Dashed lines show the spectra corresponding to the median parameter values retrieved with all the different aerosol species. In the left column, the data was simulated with a log-normal size distribution with modal particle size of 0.05 μm. The right side had a modal particle size of 1.0 μm. The true values of the other parameters are: $F = 1$, $\sigma_a = 2.5$, $P_{\rm top} = 10^{-4.5}$ bar, and $Z = 3 \times Z_\odot$.

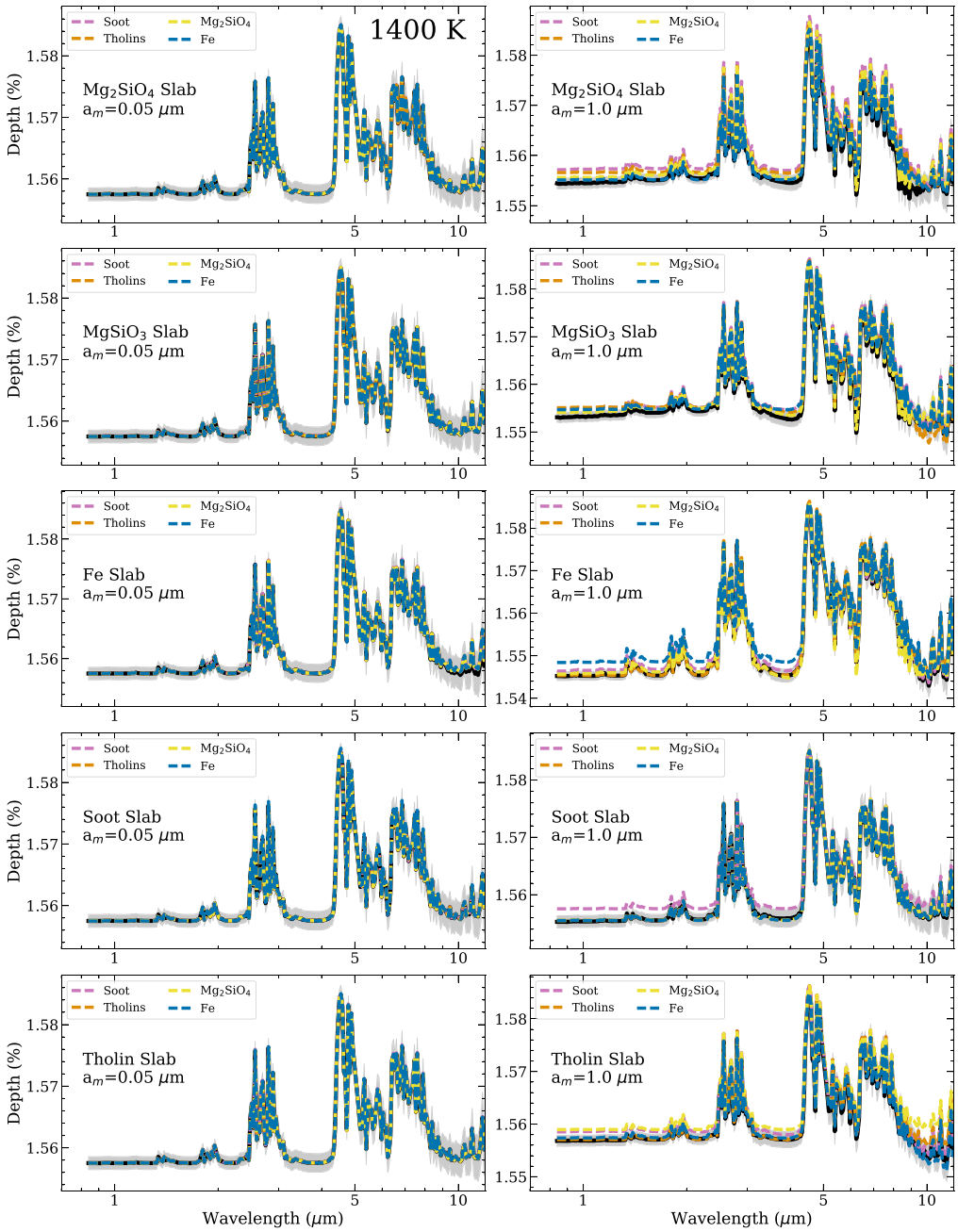

Figure 28. The results of MCMC fits for the 1400 K fiducial atmosphere. We simulated data with a slab of Mg_2SiO_4 (top row), $MgSiO_3$ (second row), Fe (third row), soot (fourth row), and tholins (bottom row). Simulated data are shown with a solid black line and the errors are shown with a shaded gray envelope. The modal particle size was 0.05 μm in the left column and 1.0 μm on the right column. The other parameters for the slab aerosol are: $F = 1.0$, $P_{\rm top}$=$10^{-4.5}$ bar, and a log-normal size distribution with $\sigma_a = 2.5$. The overall atmospheric metallicity is $Z = 3 \times Z_\odot$. Colored dashed lines show transit spectra resulting from fits with different aerosol species. These fits are computed with the median values from each parameter's MCMC chain. In the fits for data with 0.05 μm modal particle sizes (on the left), most of the fits are completely overlapping in the figure. This is reflected in the BIC values which are all within 0.02 of each other (reported in Table 7). For the larger modal particle size the silicate species are distinguishable from Fe or hydrocarbon hazes based on the BIC values.

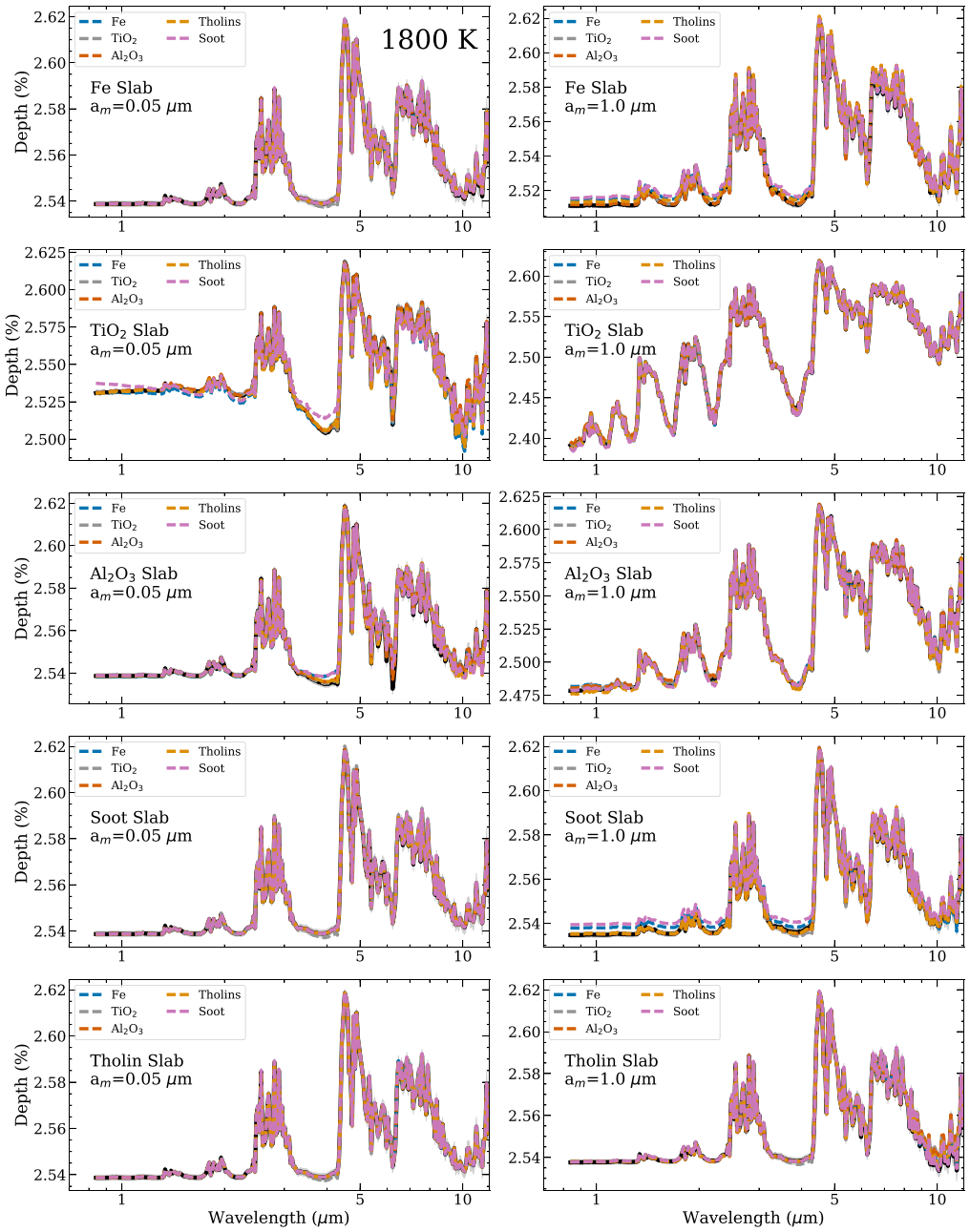

Figure 29. The results of our mixed aerosol species MCMC fits for the 1800 K atmosphere. We simulated data with a slab aerosol of Fe (top row), TiO_2 (second row), Al_2O_3 (third row), soot (fourth row), and tholins (bottom row). The slab aerosol used to simulate data always had $F = 1.0$, P_{top}=$10^{-4.5}$ bar, and a log-normal size distribution with $\sigma_a = 2.5$. The modal particle size was 0.05 μm in the left column and 1.0 μm on the right column. The overall atmospheric metallicity is $Z = 3 \times Z_\odot$. In each panel, the solid black line represents the simulated data and a lightly shaded region represents the error envelope. The size of the errors relative to the variations in the transit spectra are small, so the error envelope is just barely discernible around the data and fits. They start to show at wavelengths longer than 3 μm. The colored dashed lines show the transit spectra corresponding to the median parameter values of the posteriors mapped by the MCMC chains. The BIC for each of these fits is summarized in Table 8. Fe, tholins, and soot are indistinguishable when the modal particle size is 0.05 μm, and Al_2O_3 is also able to mimic their spectra. For the 1 μm modal particle size slab TiO_2, Fe, Al_2O_3, and soot all have the lowest BIC value in fits for their data, indicating that they would be distinguishable.

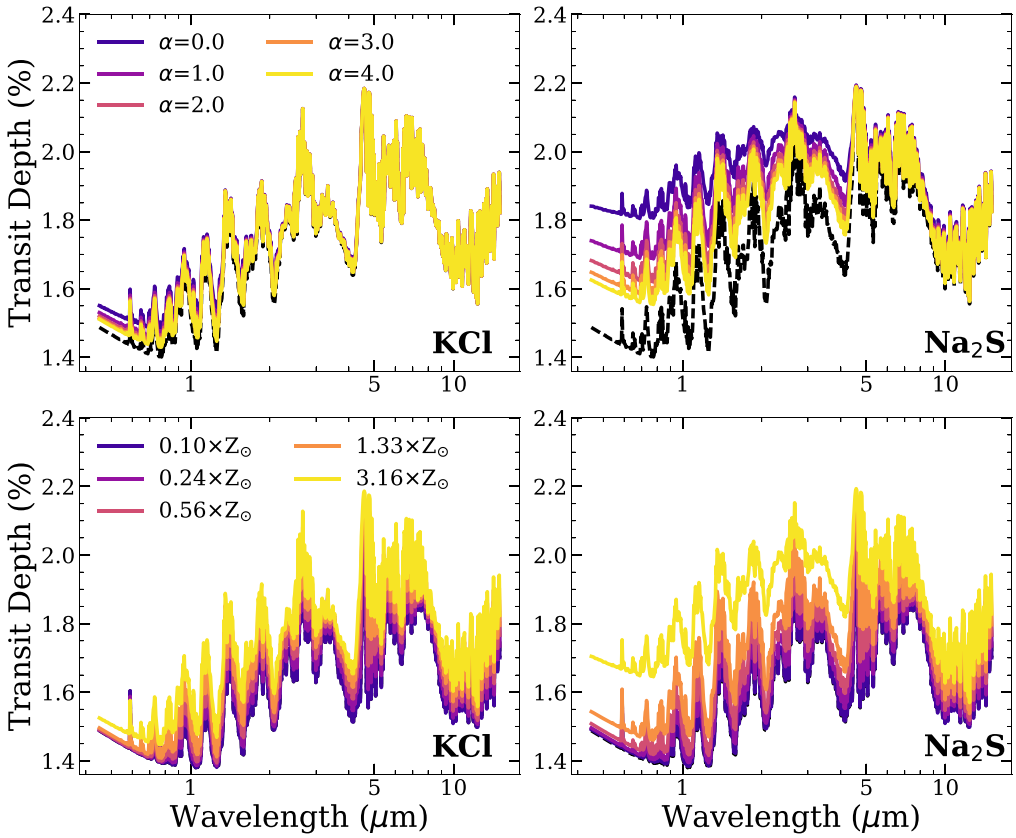

Figure 30. A demonstration of the 700 K planet's sensitivity to metallicity and α when an equilibrium cloud of KCl (left column) or Na_2S (right column) is present. The top row shows transit spectra with varying α and the bottom row shows transit spectra with varying Z. In all cases we assume $a_m = 0.5$ μm and $\sigma_a = 2.5$. When we are varying α, Z is fixed at $3 \times Z_\odot$, and when we are varying Z, we fix α at 2. In each panel a black dashed line shows the transit spectrum for the 700 K atmosphere when clear.

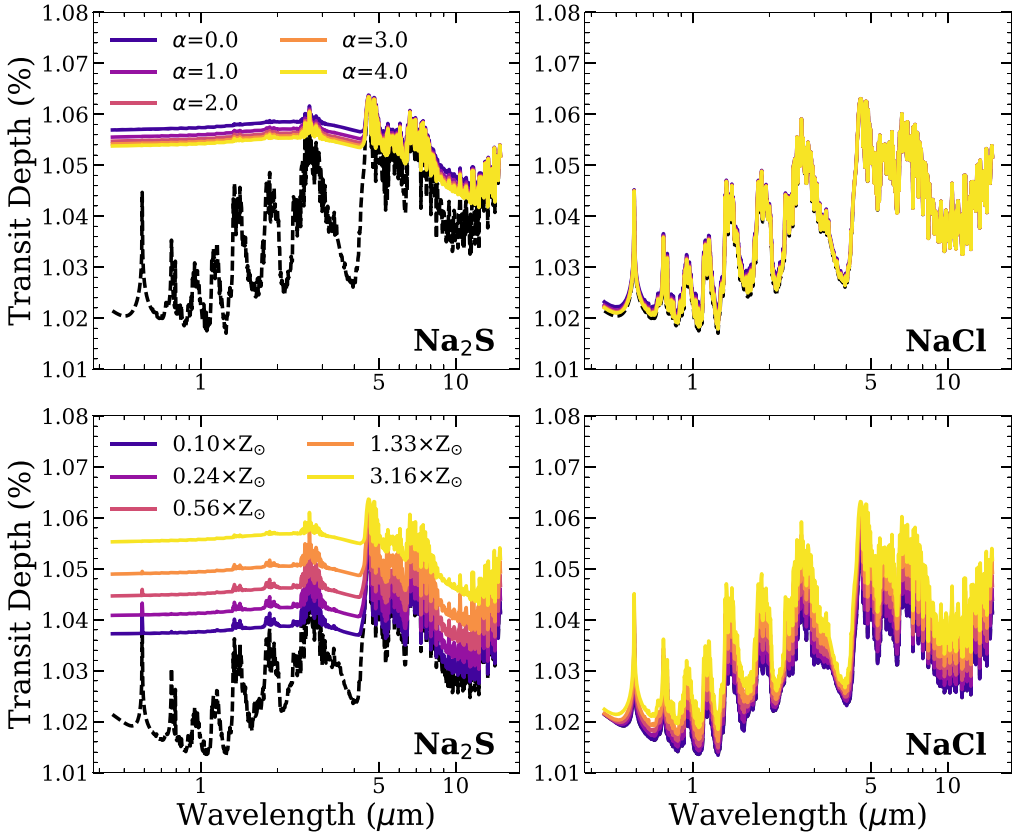

Figure 31. A demonstration of the 1000 K planet's sensitivity to metallicity and α when an equilibrium cloud of Na_2S (left column) or NaCl (right column) is present. The top row shows transit spectra with varying α and the bottom row shows transit spectra with varying Z. In all cases we assume $a_m = 0.5$ μm and $\sigma_a = 2.5$. When we are varying α, Z is fixed at $3 \times Z_\odot$, and when we are varying Z, we fix α at 2. In each panel a black dashed line shows the transit spectrum for the 1000 K atmosphere when clear.

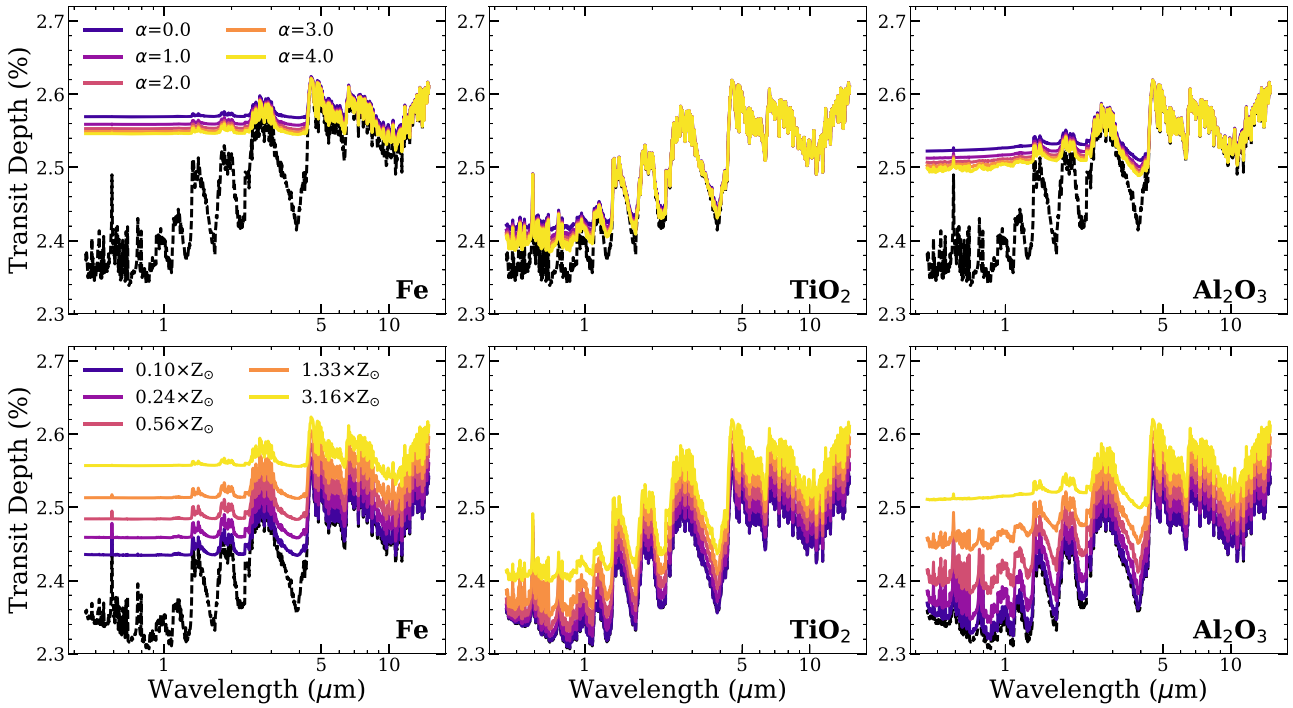

Figure 32. A demonstration of the 1800 K planet's sensitivity to metallicity and α when an equilibrium cloud of Fe (left column), TiO_2 (center column), or Al_2O_3 (right column) is present. The top row shows transit spectra with varying α and the bottom row shows transit spectra with varying Z. In all cases we assume $a_m = 0.5$ μm and $\sigma_a = 2.5$. When we are varying α, Z is fixed at $3 \times Z_\odot$, and when we are varying Z, we fix α at 2. In each panel a black dashed line shows the transit spectrum for the 1800 K atmosphere when clear.

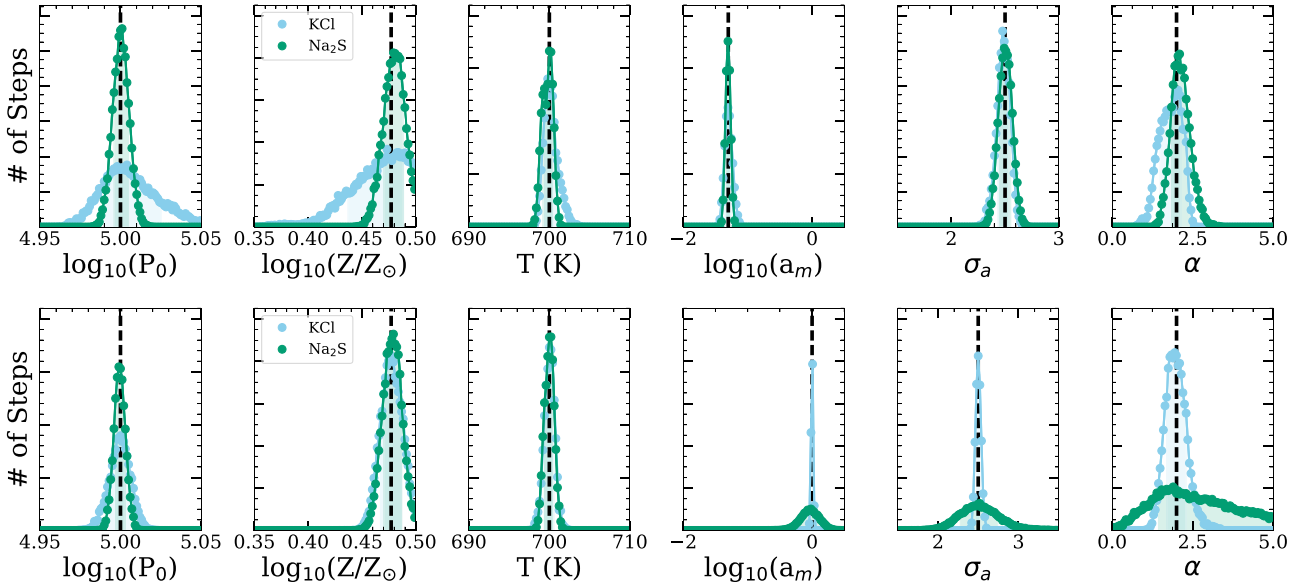

Figure 33. Histograms of posteriors for parameters from retrievals on simulated data for the 700 K fiducial atmosphere with two types of phase equilibrium clouds. The top row shows results for a cloud with a log-normal particle-size distribution with modal particle size $a_m = 0.05$ μm, and the bottom row shows results for log-normal particle-size distribution with modal particle size $a_m = 1$ μm. Vertical lines mark the true underlying values of parameters. Shaded regions indicate the portions of the posteriors that fall between the 16th and 84th percentiles.

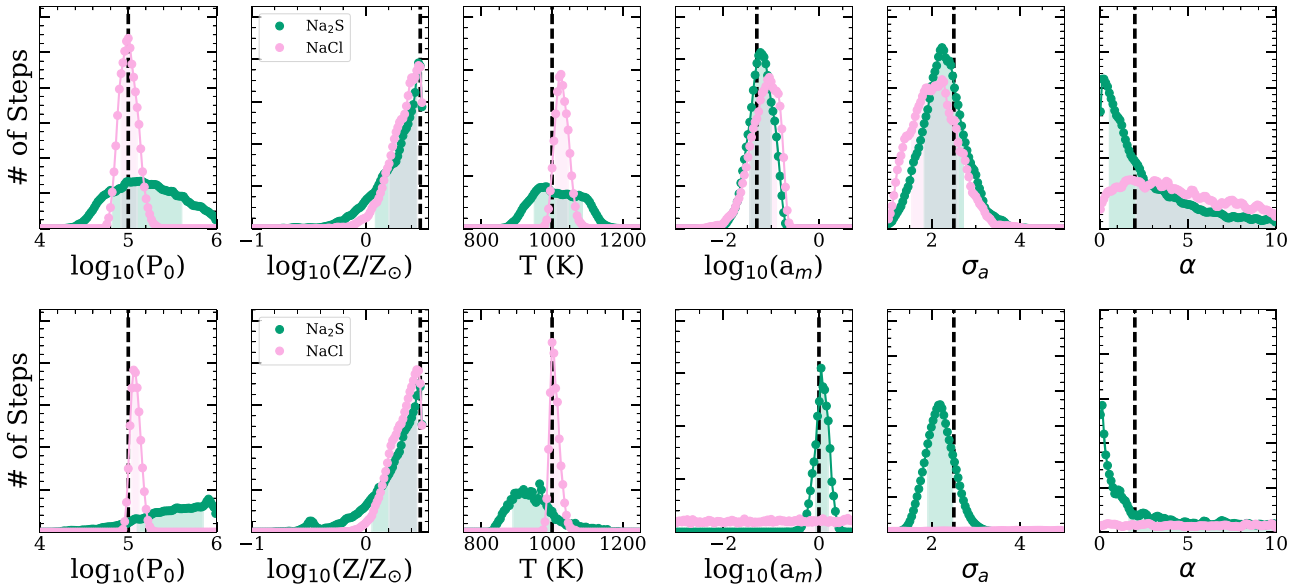

Figure 34. Histograms of posteriors for parameters from retrievals using the 1000 K fiducial atmosphere with Na_2S and NaCl phase equilibrium clouds. The top row has a log-normal particle-size distribution with modal particle size $a_m = 0.05$ μm, while the bottom row has a log-normal particle-size distribution with $a_m = 1$ μm. Vertical dashed lines indicates the true values of parameters. Shaded regions indicate the portion of the posterior that falls between the 16th and 84th percentile.

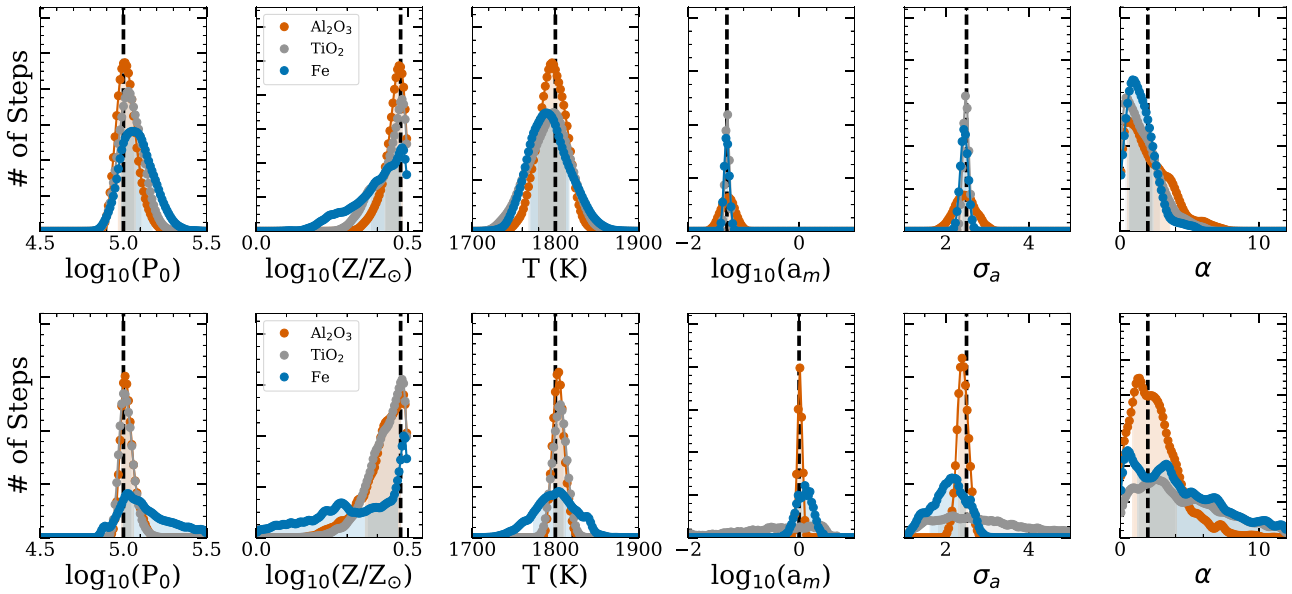

Figure 35. Histograms of posteriors for parameters from retrievals on data simulated for the 1800 K fiducial atmosphere with different species of phase equilibrium clouds. The top row has a log-normal particle-size distribution with modal particle size $a_m = 0.05$ μm, and the bottom row has a log-normal particle-size distribution with a modal particle size $a_m = 1$ μm. Colors show posteriors for different cloud species, and vertical lines denote the true values of parameters used to simulate data. Shaded regions indicate the portion of the posterior between the 16th and 84th percentile.

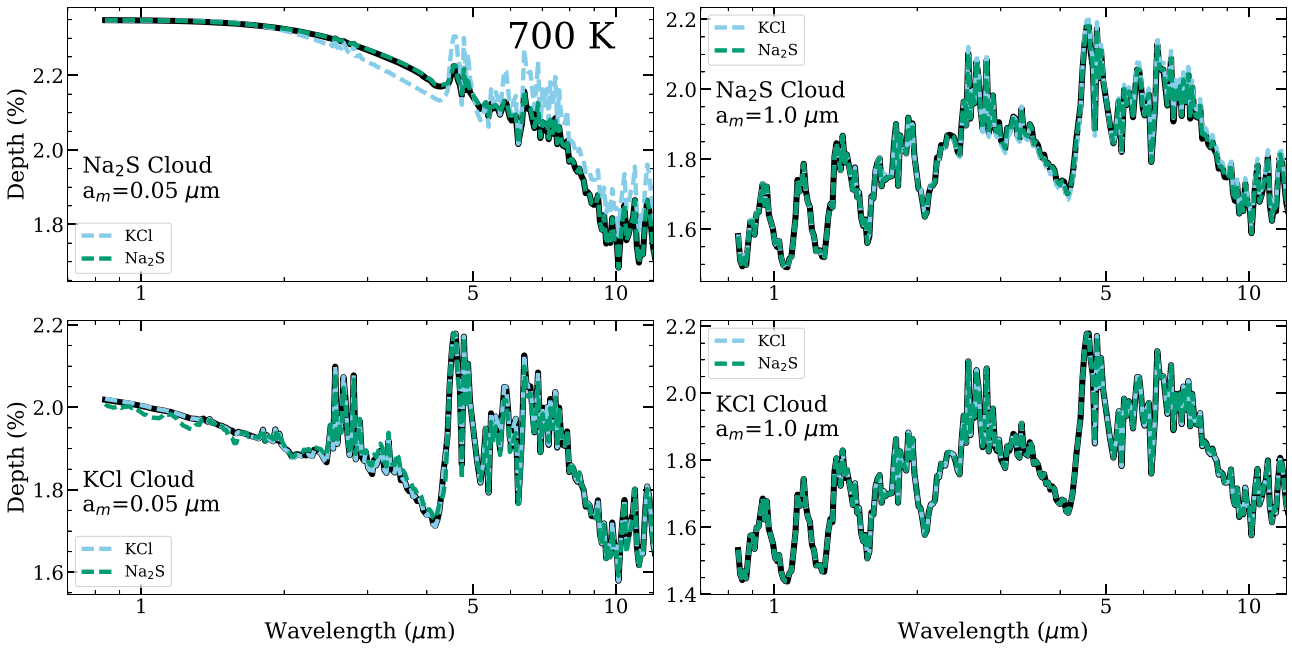

Figure 36. MCMC fits to simulated spectra for 700 K fiducial atmosphere with phase equilibrium clouds. The top row has simulated spectra with Na_2S and the bottom row has simulated spectra with KCl. The left column has a modal particle size of 0.05 μm and the right column has a modal particle size of 1.0 μm. The metallicity is always $Z = 3 \times Z_\odot$, α is 2, and the dispersion for the log-normal size distribution is always $\sigma_a = 2.5$. In each panel, the solid black line indicates the simulated data. There is also a shaded region shows the corresponding error envelope, but it is smaller than the width of the data line. The dashed lines show the transit spectra for retrieved parameters with different species of aerosols. Table 5 shows BIC values for all of these fits. Despite the curves in the right column lying nearly on top of each other, the correct species has the lowest BIC value.

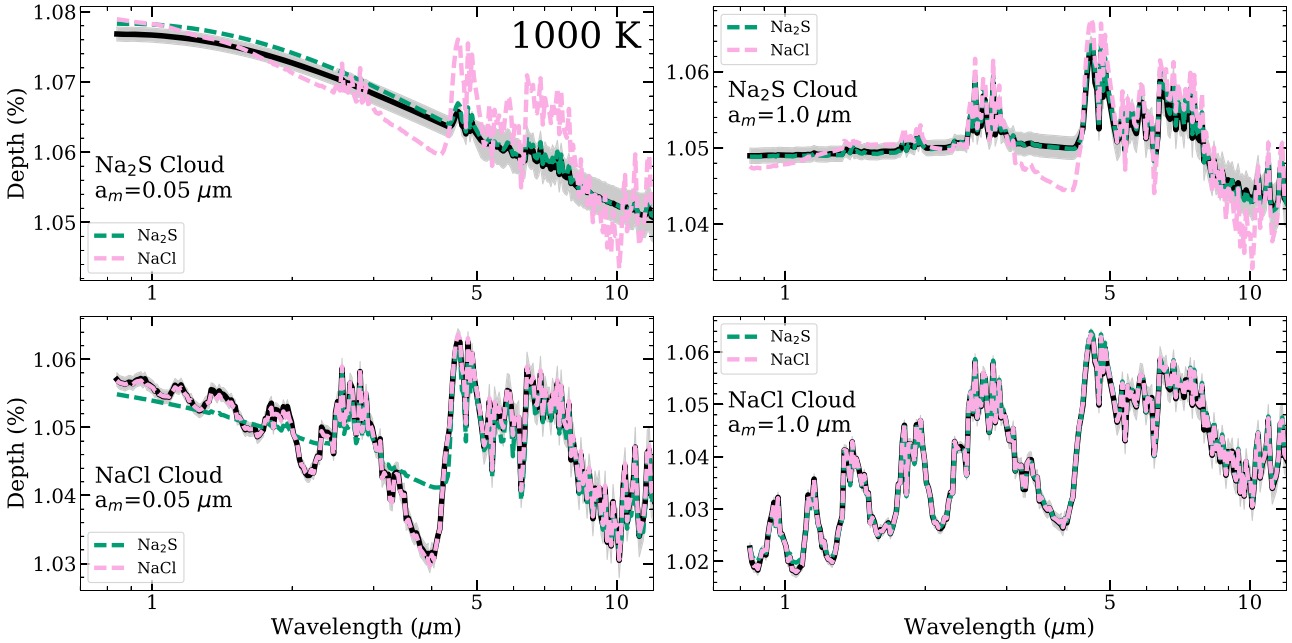

Figure 37. Results for MCMC fits to simulated data for the 1000 K atmosphere with phase equilibrium clouds. The solid black lines with shaded error envelopes indicate the simulated data. Dashed lines show the spectra for median parameter values from MCMC chains with Na_2S clouds, and NaCl clouds. In the top row the true cloud species is Na_2S and in the bottom row it is NaCl. On the left-hand side the modal particle size is 0.05 μm and on the right side the modal particle size is 1 μm. Values of BIC for all of these fits are included in Table 6. Note that in the bottom-right panel the curves are all lying nearly on top of each other.

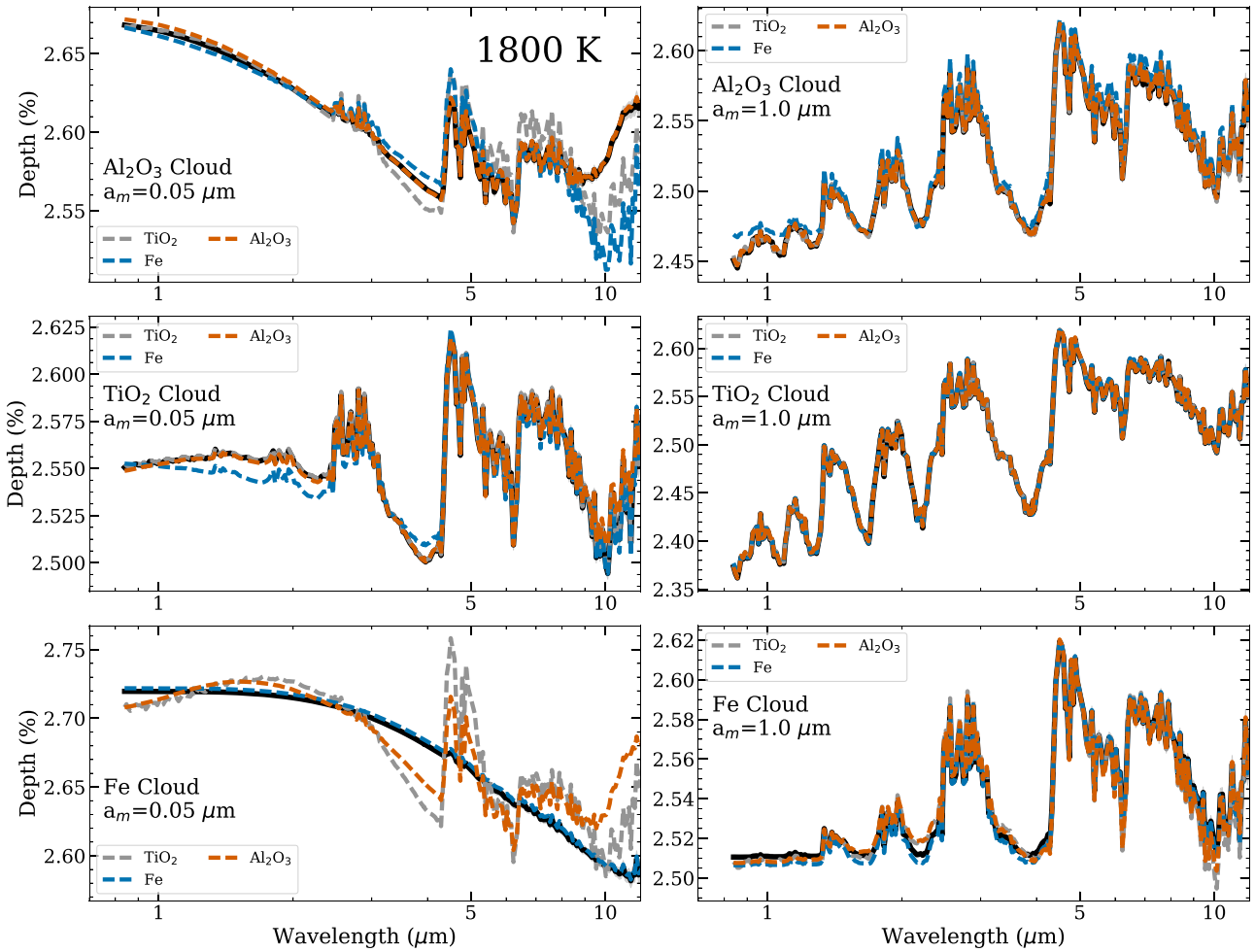

Figure 38. Results for MCMC fits to simulated data for the 1800 K atmosphere with phase equilibrium clouds. The solid black lines with shaded error envelopes indicate the simulated data. In this case the shaded error envelopes are very narrow compared to the *y*-axis scale. They only become visible at the longest wavelengths. Dashed lines show the best-fit spectra with different condensing species. In the top row the true cloud species is Al_2O_3, in the middle row the true cloud species is TiO_2, and in the bottom row it is Fe. On the left-hand side the modal particle size is 0.05 μm and on the right side the modal particle size is 1 μm. BIC values for all of these fits are summarized in Table 8.

ORCID iDs

Brianna I. Lacy https://orcid.org/0000-0002-9420-4455
Adam Burrows https://orcid.org/0000-0002-3099-5024

References

Ackerman, A. S., & Marley, M. S. 2001, ApJ, 556, 872
Adams, D., Gao, P., de Pater, I., et al. 2019, ApJ, 874, 61
Anders, E., & Grevesse, N. 1989, GeCoA, 53, 197
Astropy Collaboration, Robitaille, T. P., Tollerud, E. J., et al. 2013, A&A, 558, A33
Barstow, J. K. 2020, MNRAS, 497, 4183
Barstow, J. K., Aigrain, S., Irwin, P. G. J., et al. 2017, ApJ, 834, 50
Barstow, J. K., Changeat, Q., Garland, R., et al. 2020, MNRAS, 493, 4884
Barstow, J. K., & Heng, K. 2020, SSRv, 216, 82
Blecic, J., Dobbs-Dixon, I., & Greene, T. 2017, ApJ, 848, 127
Brown, T. M. 2001, ApJ, 553, 1006
Budaj, J., Kocifaj, M., Salmeron, R., et al. 2015, MNRAS, 454, 2
Burrows, A., & Sharp, C. M. 1999, ApJ, 512, 843
Burrows, A. S. 2014, PNAS, 111, 12601
Chang, H., & Charalampopoulis, T. T. 1990, RSPSA, 430, 577
Charbonneau, D., Brown, T. M., Noyes, R. W., et al. 2002, ApJ, 568, 377
Cubillos, P. E., Fossati, L., Erkaev, N. V., et al. 2017, ApJ, 849, 145
Dalcin, L. D., Paz, R. R., Kler, P. A., et al. 2011, AdWR, 34, 1124
Dittmann, J., Gao, P., Faherty, J., et al. 2020, AAS Meeting, 235, 248.07
Ehrenreich, D., Lovis, C., Allart, R., et al. 2020, Natur, 580, 597
Fisher, C., & Heng, K. 2018, MNRAS, 481, 4698
Foreman-Mackey, D. 2016, JOSS, 1, 24
Foreman-Mackey, D., Hogg, D. W., Lang, D., et al. 2013, PASP, 125, 306
Fortney, J. J. 2005, MNRAS, 364, 649
Fraine, J., Deming, D., Benneke, B., et al. 2014, Natur, 513, 526
Fu, G., Deming, D., Knutson, H., et al. 2017, ApJL, 847, L22
Gao, P., & Benneke, B. 2018, ApJ, 863, 165
Gao, P., Marley, M. S., & Ackerman, A. S. 2018, ApJ, 855, 86
Gao, P., Thorngren, D. P., Lee, G. K. H., et al. 2020, NatAs, 4, 951
Goodman, J., & Weare, J. 2010, Commun. Appl. Math. Comput. Sci., 5, 65
Greene, T. P., Line, M. R., Montero, C., et al. 2016, ApJ, 817, 17
He, C., Hörst, S. M., Lewis, N. K., et al. 2018a, AJ, 156, 38
He, C., Hörst, S. M., Lewis, N. K., et al. 2018b, ApJL, 856, L3
Helling, C. 2019, AREPS, 47, 583
Helling, C., Iro, N., Corrales, L., et al. 2019, A&A, 631, A79
Hörst, S. M., He, C., Lewis, N. K., et al. 2018, NatAs, 2, 303
Hubbard, W. B., Fortney, J. J., Lunine, J. I., et al. 2001, ApJ, 560, 413
Hunter, J. D. 2007, CSE, 9, 90
Irwin, P. G. J., Teanby, N. A., de Kok, R., et al. 2008, JQSRT, 109, 1136
Iyer, A. R., Swain, M. R., Zellem, R. T., et al. 2016, ApJ, 823, 109
Kawashima, Y., Hu, R., & Ikoma, M. 2019, ApJL, 876, L5
Kawashima, Y., & Ikoma, M. 2018, ApJ, 853, 7
Kawashima, Y., & Ikoma, M. 2019, ApJ, 877, 109
Khare, B. N., Sagan, C., Arakawa, E. T., et al. 1984, Icar, 60, 127
Khare, B. N., Sagan, C., Thompson, W. R., et al. 1994, CaJCh, 72, 678
Kitzmann, D., & Heng, K. 2018, MNRAS, 475, 94
Kreidberg, L., Bean, J. L., Désert, J.-M., et al. 2014, Natur, 505, 69
Lacy, B., & Burrows, A. 2020, arXiv:2006.06899
Lavvas, P., & Koskinen, T. 2017, ApJ, 847, 32
Lecavelier Des Etangs, A., Pont, F., Vidal-Madjar, A., et al. 2008, A&A, 481, L83
Lee, G., Dobbs-Dixon, I., Helling, C., et al. 2016, A&A, 594, A48

Leggett, S. K., Allard, F., & Hauschildt, P. H. 1998, ApJ, 509, 836
Line, M. R., & Parmentier, V. 2016, ApJ, 820, 78
Line, M. R., Wolf, A. S., Zhang, X., et al. 2013, ApJ, 775, 137
Louden, T., Wheatley, P. J., Irwin, P. G. J., et al. 2017, MNRAS, 470, 742
MacDonald, R. J., & Madhusudhan, N. 2017, MNRAS, 469, 1979
Madhusudhan, N. 2018, in Handbook of Exoplanets, ed. H. Deeg & J. Belmonte (Cham: Springer), 104
Mai, C., & Line, M. R. 2019, ApJ, 883, 144
Marley, M. S., & Robinson, T. D. 2015, ARA&A, 53, 279
Miller-Ricci Kempton, E., Zahnle, K., & Fortney, J. J. 2012, ApJ, 745, 3
Millman, K. J., & Aivazis, M. 2011, CSE, 13, 9
Morley, C. V., Fortney, J. J., Marley, M. S., et al. 2012, ApJ, 756, 172
Öberg, K. I., Murray-Clay, R., & Bergin, E. A. 2011, ApJL, 743, L16
Ohno, K., & Okuzumi, S. 2018, ApJ, 859, 34
Oliphant, T. E. 2006, A Guide to NumPy (USA: Trelgol Publishing), https://web.mit.edu/dvp/Public/numpybook.pdf
Oliphant, T. E. 2007, CSE, 9, 10
Ormel, C. W., & Min, M. 2019, A&A, 622, A121
Parmentier, V., Fortney, J. J., Showman, A. P., et al. 2016, ApJ, 828, 22
Pinhas, A., & Madhusudhan, N. 2017, MNRAS, 471, 4355
Pinhas, A., Madhusudhan, N., Gandhi, S., et al. 2019, MNRAS, 482, 1485
Piso, A.-M. A., Pegues, J., & Öberg, K. I. 2016, ApJ, 833, 203
Powell, D., Louden, T., Kreidberg, L., et al. 2019, ApJ, 887, 170
Powell, D., Zhang, X., Gao, P., et al. 2018, ApJ, 860, 18
Puig, L., Pilbratt, G. L., Heske, A., et al. 2016, Proc. SPIE, 9904, 99041W
Robertson, C. W., Downing, H. D., Curnutte, B., et al. 1975, JOSA, 65, 432
Rocchetto, M., Waldmann, I. P., Venot, O., et al. 2016, ApJ, 833, 120
Sánchez-Lavega, A., Pérez-Hoyos, S., & Hueso, R. 2004, AmJPh, 72, 767
Seager, S., & Sasselov, D. D. 2000, ApJ, 537, 916
Sharp, C. M., & Burrows, A. 2007, ApJS, 168, 140
Sing, D. K., Fortney, J. J., Nikolov, N., et al. 2016, Natur, 529, 59
Stevenson, K. B., Lewis, N. K., Bean, J. L., et al. 2016, PASP, 128, 094401
Sudarsky, D., Burrows, A., & Hubeny, I. 2003, ApJ, 588, 1121
Sutherland, R. A., & Khanna, R. K. 1991, AerST, 14, 331
Thorngren, D. P., Fortney, J. J., Murray-Clay, R. A., et al. 2016, ApJ, 831, 64
Tinetti, G., Drossart, P., Eccleston, P., et al. 2018, ExA, 46, 135
Tsiaras, A., Waldmann, I. P., Zingales, T., et al. 2018, AJ, 155, 156
Tsuji, T. 2002, ApJ, 575, 264
Vahidinia, S., Cuzzi, J. N., Marley, M., et al. 2014, ApJL, 789, L11
van der Walt, S., Colbert, S. C., & Varoquaux, G. 2006, CSE, 13, 22
Wakeford, H. R., & Sing, D. K. 2015, A&A, 573, A122
Wakeford, H. R., Sing, D. K., Deming, D., et al. 2018, AJ, 155, 29
Wakeford, H. R., Wilson, T. J., Stevenson, K. B., et al. 2019, RNAAS, 3, 7
Waldmann, I. P., Tinetti, G., Rocchetto, M., et al. 2015, ApJ, 802, 107
Welbanks, L., Madhusudhan, N., Allard, N. F., et al. 2019, ApJL, 887, L20
Woitke, P., Helling, C., Hunter, G. H., et al. 2018, A&A, 614, A1
Wu, Y., & Cheng, T. 2016, JQSRT, 168, 158
Yung, Y. L., Allen, M., & Pinto, J. P. 1984, ApJS, 55, 465
Yurchenko, S. N., & Tennyson, J. 2014, MNRAS, 440, 1649
Zahnle, K., Marley, M. S., Morley, C. V., et al. 2016, ApJ, 824, 137
Zellem, R. T., Swain, M. R., Cowan, N. B., et al. 2019, PASP, 131, 094401